Fabrication of Vertical Well-aligned Zinc Oxide Nanostructures for Photovoltaic Application

李昕

Xin Li

A dissertation submitted to
Kochi University of Technology
in partial fulfillment of the requirements
for the degree of
Doctor of Philosophy

Special Course for International Students
Department of Electronic and Photonic System Engineering
Graduate School of Engineering
Kochi University of Technology
Kochi, Japan

August 2014

Fabrication of Vertical Well-aligned Zinc Oxide Nanostructures for Photovoltaic Application

Xin Li

Abstract

Dye sensitized solar cells (DSSCs) have emerged as an important alternative to the conventional silicon based solar cells due to their fascinating features such as low fabrication cost and relatively high efficiency. Since the invention by Prof. O'Regan and Prof. Grätzel in 1991, DSSCs have been intensively studied and are currently undergoing rapid development for commercial applications. Now, the commercial DSSC product has already obtained 10% while the highest efficiency of DSSC in lab was about 15%.

However, the development of DSSC has reached bottleneck in the improvement of efficiency. One reason is difficult to obtain textured TiO_2 to absorb more dye molecules. TiO_2 was used as photoanode in the traditional DSSC. The common TiO_2 was nanocrystalline porous films. But the results exhibited that porous TiO_2 film was not so high efficiency in the absorption of dye molecules. Most of the TiO_2 film surface was ineffective. So to increase the effective surface area is the key to increase the absorption of dye molecules resulting in the efficiency increase. Based on our previous work on ZnO nanostructure, we designed a novel DSSC structure to try to achieve vertical

well-aligned ZnO nanostructures to replace TiO_2 to increase the efficiency of DSSC.

In this dissertation, my main work focused on the fabrication of vertical well-aligned large surface ZnO nanostructures for dye-sensitized solar cell applications. There were three main requirements for ZnO nanostructures to be used in dye-sensitized solar cell applications:

(a) Vertical well-aligned ZnO nanostructures to obtain high transmittance and fast electron transportation.

(b) Large surface area to help absorbing more dye molecules.

(c) Conductive and transparent TCO substrates to help reducing the series resistance of the solar cell and increasing the transmittance.

Through solving these problems, I can get the ZnO-based DSSC with the high conversion efficiency of 3.75%. The world best pure ZnO-based DSSC has a efficiency about 4.7% with a special designed dye, our ZnO-based DSSC not only has similar efficiency with the commercial dye, but also has much better reproducibility.

In my research, there are several novel ideas solving these requirements:

1) Developing novel multi-annealing technique to fabricate vertical well-aligned ZnO nanostructures. (1 paper published)

2) Introducing the novel mist chemical vapor deposition (Mist CVD) technique to fabricate ZnO nanostructures with controllable size and morphology (1 paper published, 1 submitted paper)

3) High transmittance and conductivity ITO substrates for the DSSCs. (1 submitted paper)

The main work and results of thesis will be exhibited by chapters one by one as follows.

Chapter 1 Introduction

The research background of ZnO was introduced in detail. ZnO is one of potential material applied for the optoelectronic applications due to its unique characteristics. But, some urgent issues were still remained for the further industrial applications. In order to solve these remained issues, the objectives of thesis were proposed and the outline of the thesis was built.

Chapter 2 Fabrication and characterization

The working principles and operation manual of fabrication and analysis equipment were introduced in this chapter.

Fabrication equipment:

ZnO thin films were prepared by radio frequency magnetron sputtering system. The post-treatment processes were applied in the conventional quartz annealing furnace. The morphology modification of ZnO nanostructures were carried out in the Mist CVD system.

Analysis equipment:

Following the fabrication procedure, a number of characterizations were applied to evaluate the structural, electric and optical properties. The structural properties were inspected using X-ray diffraction. A field emission scanning electron microscope (FE-SEM) and a transmission electron microscope (TEM) system were used to

characterize the morphology and microstructure. The surface morphology and the root-mean-square (rms) surface roughness of the films were characterized using an atomic force microscope (AFM). The luminescent characteristics were measured by photoluminescence (PL) measurement. Optical transmission spectra measurements were performed using an UV-visible spectrophotometer. The electrical property was measured using a Hall measurement system.

Chapter 3 Fabrication of vertical well-aligned ZnO nanostructures by single annealing process

In this chapter, the influence of the substrates and annealing temperatures were investigated.

The substrates had significant influence of ZnO films, further influence on fabrication of well-aligned ZnO nanostructures. ZnO film deposited on the silicon had the best crystallinity and the formed ZnO nanostructures with the best alignment and the highest density. The lower mismatch of the lattice imperfections and matching thermal expansion coefficient between ZnO film and substrates contributed to fabricating ZnO film with good crystallinity and vertical well-aligned ZnO nanostructures. The density and height of ZnO nanostructures were increased with the increase of the annealing temperature. The diameter of ZnO nanostructures were increased when the temperature increased in the suitable range. The blue-green emission centered at 491nm was obtained from all of annealed samples, with the suppressed UV emission at about 378nm. The intensity of visible peak (around 491nm) was increased with the increase of temperature.

Chapter 4 Fabrication of large size ZnO nanostuctures by multiple annealing processes

In this chapter, the effects of different post-treatment processes on the ZnO nanostructures were investigated. The conclusions of each part in this chapter will be generally expressed one by one.

The oxygen treatment time can help adjusting the size of obtained ZnO nanostructures. Because oxygen annealing between the two reducing gas annealing processes contributed to efficiently introduce the oxygen into the ZnO thin films, leading to ZnO nanostructures regrown quickly. The low temperature treatment can help controlling the density of the obtained ZnO nanostructures. ZnO nanostructures with controllable size were obtained via the novel multi-annealing processes.

Chapter 5 Morphology modification of ZnO nanostructures by Mist CVD treatment

In this chapter, the effects of Mist CVD carrier gases and post annealing time on the crystal growth, structural properties were investigated.

The obtained ZnO nanostructures exhibited different morphology and crystallinity with different carrier gases: the growth of ZnO nanostructures was epitaxial growth in the carrier gas Argon, indicating the obtained ZnO nanostructures were good single crystal with well-aligned ZnO nanosheets on the surface; the growth of ZnO nanostructures were random in the carrier gas Air, resulting in the obtained ZnO nanostructures were polycrystalline with intertwined nanosheets on the surface. Choosing the suitable carrier gases can help us obtaining the ZnO nanostructures with the designed crystallinity and surface morphology.

With the increase of Mist CVD treatment time, the surface morphology of ZnO nanostructures were modified with intertwined (carrier gas: air) and aligned (carrier gas: argon) nanosheets and the size of ZnO nanostructures was enlarged. The size and morphology of ZnO nanostructure can be well controlled by modulating the Mist CVD treatment time.

Chapter 6 DSSC fabrication and applications

In this chapter, the feasibility of ZnO nanostructures used as photoanode in DSSC was investigated.

If the ITO film thickness increased, the roughness and Hall mobility of ITO films was increased while the resistivity of ITO films was decreased. The as-deposited ZnO films deposited exhibited better crystallinity, and the following formed ZnO nanostructures showed the higher density, transmittance as well as better vertical alignment when the ITO film thickness decreased. The highest overall conversion efficiency of demonstrated dye-sensitized solar cell was 3.65% with a fill factor 0.528. The Jsc and Voc were 12.67mA/cm^2 and 0.551V, respectively.

Chapter 7 Conclusions

The main results obtained from this research work are summarized.

Acknowledgements

First of all, I would like to express my sincere appreciate to my supervisor Prof. Hatta Akimitsu for his guidance and supports during my Ph.D. study and research. Thank you for offering me the opportunity to study in KUT and great encouragement in my whole research work. It is my honor to be your student and I am proud of it.

Specially, I want to give my thanks to my vice-supervisor Prof. Chaoyang Li who directed me into the scientific research area and take care of me both on research and daily life. To me, she is more like a mother more than a supervisor. I will never forget what I learned from her, which will benefit my entire life.

I would like to thanks to my co-supervisor Prof. Mamoru Furuta for supporting me in the use of cleanroom and equipment as well as giving me much more effective suggestions and helps on my research.

I also want to thanks my co-supervisor Associate Prof. Hiroshi Furuta for his kind-hearted encouragement and instructive advices on my research.

I also want to give my sincere thanks to the members in Institute for Nanotechnology, to Associate Prof. Toshiyuki Kawaharamura for his kind help in my daily research and discuss with me; To Associate Prof. Hisao Makino, and Dr. Noriko Nitta for teaching me the equipment principle and operation.

For my dear SSP fellows, I cherish the great periods and the friendship with all of you.

Last but not least, I so appreciate my parents for their endless supporting and love and everything you have done for me. Thank you so much.

Caption of Figures

Fig. 1.1 The crystal structure of ZnO

Fig. 1.2 The schematic diagram of VLS method.

Fig. 1.3 The ZnO nanowires obtained by VLS method.

Fig. 1.4 The ZnO nanotubes fabricated by the MOCVD method.

Fig. 1.5 The obtained ZnO nanobelts

Fig. 1.6 The obtained different kinds of ZnO nanostructures.

Fig. 1.7 The structure of traditional TiO_2-based dye-sensitized solar cell

Fig. 1.8 The working principle of dye-sensitized solar cell

Fig. 1.9 The efficiency development of DSSC

Fig. 1.10 The novel DSSC structure using ZnO/PEI as photoanode.

Fig. 1.11 The novel DSSC structure with ZnO photoanode and special designed SK1-dye.

Fig. 1.12 The structural of my thesis.

Fig. 2.1 The schematic diagram of RF sputtering

Fig. 2.2 The annealing furnace

Fig. 2.3 The Mist CVD system

Fig. 2.4 The schematic diagram of XRD

Fig. 2.5 The SEM system

Fig. 2.6 The schematic diagram of SEM

Fig. 2.7 The schematic diagram of PL system

Fig. 2.8 The TEM system

Fig. 2.9 The schematic diagram of TEM system

Fig. 2.10 The AFM system

Fig. 2.11 The schematic diagram of AFM system

Fig. 2.12 The Hall system

Fig. 2.13 The schematic diagram of Hall system

Fig. 3.1 (a) XRD patterns and (b) dependence of c-axis crystallite sizes and FWHM of as-deposited ZnO films on different substrates

Fig. 3.2 Dependence of lattice constant c and stress of as-deposited ZnO films on different substrates.

Fig. 3.3 SEM images of as-deposited ZnO film on (1) Qz glass, (2) FTO glass, (3) sapphire, and (4) silicon

Fig. 3.4 Comparison of ca ratio of as-deposited ZnO films on different substrates

Fig. 3.5 AFM images of ZnO films (500 nm in thickness) deposited on (a) Qz glass, (b) FTO glass, and (c) silicon

Fig. 3.6 XRD patterns of ZnO nanostructures on different substrates (after reducing annealing, two peaks of Al2O3 appeared in XRD pattern of ZnO sapphire)

Fig. 3.7 SEM images of fabricated ZnO nanostructures on (a) Qz glass, (b) FTO glass, (c) sapphire, and (d) silicon.

Fig. 3.8 The energy level diagram of ZnO Eigen defect

Fig. 3.9 The growth mechanism of ZnO nanostructures

Fig. 3.10 The TEM images of a ZnO nanorod

Fig. 3.11 XRD patterns of ZnO nanostructures obtained from different annealing temperatures

Fig. 3.12 SEM images of fabricated ZnO nanostructures in (1) 460 ℃ (2) 450 ℃, (3) 440 ℃, and (4) 420 ℃.

Fig. 3.13 PL spectra of ZnO nanostructures obtained from different annealing

temperatures

Fig. 4.1 The annealing parameters.

Fig. 4.2 SEM images of (a) as-deposited ZnO films and fabricated ZnO nanostructures with (b) 0min (c) 15min, (d) 30min, and (e,f) 60min.

Fig. 4.3 The XRD spectra of ZnO nanostructures with different oxygen annealing treatment time.

Fig. 4.4 The PL spectra of ZnO nanostructures with different oxygen annealing treatment time

Fig. 4.5 The SEM images of ZnO nanostructures with different oxygen annealing treatment.

Fig. 4.6 The annealing processes of different steps.

Fig. 4.7 The XRD patterns of ZnO nanostructures with different multiple annealing processes

Fig. 4.8 Dependence of intensity and FWHM of obtained ZnO nanostructures on different annealing processes.

Fig. 4.9 The SEM images of ZnO nanostructures with different multiple annealing processes.

Fig. 4.10 The HRTEM images of a ZnO nanorod obtained from the multiple annealing processes.

Fig. 4.11 The transmittance of ZnO nanostructures with different multiple annealing processes.

Fig. 4.12 The PL spectra of ZnO nanostructures with different multiple annealing processes.

Fig. 5.1 The figure of Mist CVD system.

Fig. 5.2 The SEM images of (a) as-deposited ZnO film and (b) ZnO nanostructures obtained from reducing annealing process.

Fig. 5.3 Influence of Mist CVD treatment time (1) after reducing annealing; (2) 5min in air; (3)30min in air; (4) 5min in argon; (5)30min in argon.

Fig. 5.4 The HRTEM images of ZnO nanorods obtained from different processes.

Fig. 5.5 SEM images of ZnO nanostructures regrowth after treated in Mist CVD in air for (1) 0 min (2)5min, (3)30min, (4)45min, (5)60min, (6)75min. (a: top view and b: cross section view)

Fig. 5.6 Relationship between regrowth of ZnO nanostructures and Mist CVD post-treatment time in air

Fig. 5.7 (a) XRD patterns and (b) Dependence of intensity and FWHM of ZnO nanostructures on Mist CVD treatment time in air

Fig. 5.8 PL spectra of ZnO nanostructures on Mist CVD treatment time in air

Fig. 5.9 SEM images of ZnO nanostructures regrowth after treated in Mist CVD in argon for (1) 0 min (2)5min, (3)30min, (4)45min, (5)60min, (6)75min. (a: top view and b: cross section view)

Fig. 5.10 Relationship between regrowth of ZnO nanostructures and Mist CVD post-treatment time in argon

Fig. 5.11 XRD patterns of ZnO nanostructures on Mist CVD treatment time in argon

Fig. 5.12 PL spectra of ZnO nanostructures on Mist CVD treatment time in argon.

Fig. 6.1 The schematic diagram of dye-sensitized solar cell

Fig. 6.2 The comparison of TiO_2 and ZnO based photoanode (with the N719 dye, I^-/I_3^- electrolyte, TCO substrate)

Fig. 6.3 AFM images of ITO thin films with thickness of (a) 200nm, (b) 300nm, (c) 400nm, and (d) 500nm.

Fig. 6.4 The dependence of resistivity and Hall mobility on the thickness of ITO films.

Fig. 6.5 The dependence of optical transmittance on the ITO film thickness.

Fig. 6.6 The XRD patterns of as-deposited ZnO films on ITO film with different thickness.

Fig. 6.7 SEM images of as-deposited ZnO film and nanostructures on ITO films with different thickness (1) 200nm (2) 300nm (3) 400nm and (4) 500nm. (a: as-deposited ZnO films; b: obtained ZnO nanostructures).

Fig. 6.8 The optical transmittance of ZnO nanostructures on ITO films with different thickness.

Fig. 6.9 (a) SEM images of ZnO nanorods (a) as-deposited ZnO film, (b) after reducing annealing, and (c) after long time reducing annealing.

Fig. 6.10 J-V curve of the demonstrated dye-sensitized solar cell (a: short ZnO nanostructures; b: long ZnO nanostructures; tested under simulated sunlight AM 1.5 with the radiant power of 100mW/cm^2)

Caption of Tables

Table 1.1 The physical properties of ZnO.

Table 1.2 The current solar cells classification

Table 3.1 The parameters of obtained ZnO nanostructures.

Table 5.1 Mist CVD conditions with different carrier gases

Table 6.1 The comparison of ZnO and TiO_2

Chapter 1: Introduction

1.1 The literature of ZnO material……………………………………………18
1.1.1 Properties of zinc oxide
1.1.2 Fabrication of ZnO nanostructure
1.2 The literature of DSSC……………………………………………23
1.2.1 Background of study on DSSC
1.2.2 ZnO-based DSSC
1.3 Objectives and structure of this thesis……………………………………………27
1.4 References……………………………………………35

Chapter 2: Fabrication and characterization

2.1 Fabrication equipment……………………………………………39
2.1.1 Radio frequency magnetron sputtering
2.1.2 Conventional annealing furnace
2.1.3 Mist CVD system
2.2 Characterization techniques……………………………………………41
2.2.1 X-ray diffraction
2.2.2 Field emission scanning electron microscope
2.2.3 Photoluminescence spectroscopy
2.2.4 Transmission spectroscopy
2.2.5 Atom force microscope
2.2.6 Hall measurement device
2.3 References……………………………………………55

Chapter 3: Fabrication of vertical well-aligned ZnO nanostructures by single annealing process

3.1 Introduction……………………………………………56
3.2 Substrate dependence……………………………………………58
3.2.1 Experiments
3.2.2 Results and discussion
3.2.3 Summary
3.3 Annealing temperature dependence……………………………………………67
3.3.1 Experiments
3.3.2 Results and discussion
3.3.3 Summary

3.4 Conclusions……………………………………………………………………70
3.5 References…………………………………………………………………...82

Chapter 4: Fabrication of large size ZnO nanostructures by multiple annealing processes

4.1 Introduction……………………………………………………………………85
4.2 Influence of oxygen annealing time…………………………………………...87
4.2.1 Experiments
4.2.2 Results and discussion
4.2.3 Summary
4.3 Influence of low temperature treatment………………………………………...89
4.3.1 Experiments
4.3.2 Results and discussion
4.3.3 Summary
4.4 Fabrication of large size ZnO nanostructures………………………………....91
4.4.1 Experiments
4.4.2 Results and discussion
4.4.3 Summary
4.5 Conclusions..93
4.6 References……………………………………………………………….103

Chapter 5: Morphology modification of ZnO nanostructures by Mist CVD treatment

5.1Introduction……………………………………………………………………104
5.2 Carrier gas dependence……………………………………………………105
5.2.1 Experiments
5.2.2 Results and discussion
5.2.3 Summary
5.3 Mist treatment time dependence……………………………………………109
5.3.1 Experiments
5.3.2 Results and discussion
5.3.3 Summary
5.4 Conclusions……………………………………………………………………113
5.5 References……………………………………………………………………123

Chapter 6: DSSC fabrication and applications

6.1 Introduction……………………………………………………………124
6.2 ZnO-based DSSC fabrication……………………………………………126
6.2.1 Experiments
6.2.2 Characterization of ZnO based DSSC
6.2.3 Summary
6.3 Conclusions……………………………………………………………134
6.4 References……………………………………………………………145
Chapter 7: Conclusions……………………………………………………146
List of publications…………………………………………………………150

Chapter 1

Introduction

1.1 The literature of Zinc oxide material

1.1.1 Properties of zinc oxide

1.1.1.1 General properties

Zinc oxide (ZnO) is an important novel wide bandgap oxide semiconductor material. Crystalline ZnO is thermochromic. The melting point of ZnO is 1975 ℃. The physical properties were shown in Table 1.1 [1-2]. Zinc oxide is an amphoteric oxide. It is nearly insoluble in water, but it is soluble in most of acids, such as hydrochloric acid. ZnO reacts slowly with fatty acids in oils to produce the corresponding carboxylates, such as stearate [3-4].

ZnO has three different crystal structures: the hexagonal wurtzite, the cubic zinc blende and the cubic rock salt. The wurtzite structure is most commonly used due to the highest stability under normal working conditions with a=0.325 nm and c=0.521 nm.

The wurtzite ZnO exhibited the structure of ABAB hexagonal close packing (HCP), with the alternating planes composed of O^{2-} and Zn^{2+} ions tetrahedral coordinated and stacked along the c-axis on an alternate basis (Fig. 1.1) [5]. The diversification of ZnO surface energy owes to the normal dipole moment and instant polarization fabricated by the Zn^{2+} and O^{2-} ions [6-8].

Table 1.1 The physical properties of Zinc Oxide [1]

Properties of wurtzite ZnO

Property	Value
Lattice parameters at 300 K	
a_0	0.324 95 nm
c_0	0.520 69 nm
a_0/c_0	1.602 (ideal hexagonal structure shows 1.633)
u	0.345
Density	5.606 g cm^{-3}
Stable phase at 300 K	Wurtzite
Melting point	1975 °C
Thermal conductivity	0.6, 1–1.2
Linear expansion coefficient (/C)	a_0: 6.5×10^{-6}
	c_0: 3.0×10^{-6}
Static dielectric constant	8.656
Refractive index	2.008, 2.029
Energy gap	3.4 eV, direct
Intrinsic carrier concentration	$<10^6$ cm^{-3}
Exciton binding energy	60 meV
Electron effective mass	0.24
Electron Hall mobility at 300 K for low n-type conductivity	200 cm^2 V^{-1} s^{-1}
Hole effective mass	0.59
Hole Hall mobility at 300 K for low p-type conductivity	5–50 cm^2 V^{-1} s^{-1}

Another important characteristic of ZnO is its polar surfaces. For ZnO, (0001) has the lowest Gibbs free energy, resulting in a smooth surface in the equilibrium state, so ZnO structures have a strong (0001) preferred orientation to form hexagonal structure. At the same time, to maintain a stable structure, the polar surfaces generally have facets or exhibit massive surface reconstructions, but ZnO ±(0001) surfaces are exceptions: they are atomically flat, stable and exhibit no reconstruction,. The other two most commonly observed facets for ZnO are {2-1-10} and {01-10}, which are non-polar and have lower energy than the {0001} facets. The oppositely charged ions in ZnO ±(0001) produce positively charged Zn^-(0001) and negatively charged O^-(000-1) surfaces, resulting in a normal dipole moment and spontaneous polarization along the (0001) direction (c-axis) [9-13].

1.1.1.2 Optoelectronic properties

For the optoelectronic materials, the direct bandgap semiconductor is needed to produce an effective amount of photons, the current optoelectronic materials in industry are mainly Group III-V semiconductors, because most of the Group III-V materials are direct bandgap semiconductors. ZnO is one of the few of II-VI direct bandgap material [14-15]. The energy gap of ZnO is 3.3eV, which is quite wide, suitable to be used as the emitting material of the blue and ultraviolet light, such as the laser diode or the short-wavelength light-emitting devices [16]. Additionally, ZnO has a large exciton binding energy (60meV), much higher than other wide bandgap semiconductor materials (such as GaN 25mev, ZnSe 22meV), which makes the ZnO more stable than other materials in room temperature.

1.1.1.3 Electronic properties

For the ZnO materials, the essential (intrinsic) defects such as oxygen vacancies or interstitial zinc atoms make it easy to form n-type semiconductor. With doping the Group III elements such as Al, Ga, n-type ZnO semiconductor with much higher electron carrier concentration can be obtained. However, the fabrication of p-type ZnO was quite difficult. The common method was doping with nitrogen.

Since the n-type ZnO has a high transmittance and conductivity, the more attention was paid to apply it in the transparent conductive glass applications. Hoffman et al. [17] fabricated the ZnO-based thin film transistor, with the transmittance of 75% in the visible wavelength range, known as the transparent transistors. The ZnO material has the high potential to be applied in the active component or transparent optoelectronic components of the flat panel display applications.

1.1.1.4 Other properties

ZnO has piezoelectric properties due to the non-central symmetric structure obtained from tetrahedral coordination in ZnO, making it to be used in the micro sensors and micro actuator. Furthermore, the grain boundary barrier energy of the polycrystalline zinc oxide thin film is quick high, so it is widely used in the rheostat [18-19].

1.1.2 Fabrication of ZnO nanostructures

Due to the strong (0001) polar surface existed in the ZnO crystals, ZnO can be easily fabricated into different kinds of nanostructures, such as the nanorod, nanosheet, nanoneedle, etc. [20-22]. Till now, several fabrication methods have been applied to synthesis the ZnO nanostructures, including vapor-liquid-solid (VLS) method, thermal evaporation method, chemical vapor deposition (CVD), metal-organic vapor-phase epitaxy, metal-organic chemical vapor deposition (MO-CVD), chemical vapor deposition (CBD), etc. [23-28].

VLS growth method was the most common method to grow one dimensional ZnO nanomaterials. The schematic diagram of VLS method was shown in Fig. 1.2. With the appropriate catalyst precipitation nanowires as media, ZnO nanostructures can be grown up. Furthermore, the VLS method can fabricate the nanostructures in the selective area with the proper design of the catalyst area. Yang et al. [29] using VLS mechanism, succeeded in the fabrication of high density ZnO nanowires with the Au as a catalyst, as shown in Fig. 1.3.

The MOCVD method was different from the traditional VLS mechanism, because the growth process of MOCVD method does not use the metal catalyst particles. Therefore, it was also called MOVPE (metalorganic vapor-phase epitaxy). Also, compared with thermal evaporation, the MOCVD method has a relatively low growth temperature,

around 400 ℃. Zhang et al. [30] fabricated the vertical well-aligned ZnO nanotube by the MOCVD technique, as shown in Fig. 1.4. Its growth mechanism was presumed to spiral columnar growth.

In 2001, Wang et al. [31] heated the zinc oxide powder in a high temperature furnace in 1400 ℃ for 2 hours under the pressure 300torr. The working gas was pure argon. Then the world first ZnO nanobelt was fabricated, as shown in Figure 1.5.

In addition, Wang's group also used this simple synthetic method to fabricate a lot of different ZnO nanostructures, such as the nanocombs, nanorings, nanosprings, etc., as shown in Fig.1.6.

Until now, a number of methods can be used to fabricate a variety of ZnO nanostructures. However, there still many issues were remained for further industrial applications, such as the poor reproducibility, difficult alignment, the complicated processes, high cost, difficult to scale up and pollution to the environment, etc. Therefore, a novel technique to fabricate controlled vertical well-aligned ZnO nanostructures was still needed.

In our previous work [23, 26], we have many experiences on the fabrication of high quality ZnO thin film using RF magnetron sputtering. The relationship between the deposition parameter, the substrates and the properties of obtained films were investigated. The sputtering mechanism of the ZnO film was discussed. The fabrication techniques of zinc-rich and oxygen-rich ZnO films were well optimized.

In recent years, we had succeeded in obtaining the hexagonal-cone ZnO nanostructures on ZnO film using low temperature treatment in a reducing gas ambient [32-33], which was completely different from other current fabrication techniques of ZnO nanostructures. In our technique, ZnO films were fabricated by RF magnetron

sputtering in pure argon, resulting in the ZnO films having zinc atoms inside. Then the as-deposited ZnO films were annealed in the reducing ambient to transform the ZnO films to be ZnO nanostructures following the VLS mechanism. During the annealing process, zinc atoms inside the ZnO films can help to format the ZnO nuclei, using as catalyst. Therefore , the common additional metal catalyst was not needed, so our method was called “self-catalyst” method.

1.2 The literature of dye-sensitized solar cell

1.2.1 Background of study on dye-sensitized solar cell

The exhaustion of fossil resources in the near future force the humans reevaluate the importance of developing the renewable energy sources, such as solar energy. Thus far, silicon-based solar cells have been widely used, but they still can’t compete with fossil fuels due to the high cost. It is an urgent issue to develop much cheaper photovoltaic devices with reasonable efficiency. Now, there are three kinds of solar cells available to get, as shown in Table 1.2.

Table 1.2 The current solar cells classification

Type of cell		Efficiency (%)	Characteristics		
			Cost	Stability	Industrial production
Silicon based solar cell	Crystalline	25	×	○	○
	Multicrystalline	18	×	○	○
	Amorphous	13	△	×	×
$CuInSe_2$ based solar cell (CIGS)		24	×	○	○
III-V semiconductors (GaAs, InP) based solar cell		45	×	○	×
Dye-sensitized solar cells (DSSC)		15	○	○	○
Organic solar cell (OSC)		10	○	○	×

Till now, the most popular solar cells were silicon-based solar cells, including the crystalline, polycrystalline, and the amorphous three kinds. The crystalline and

polycrystalline silicon based solar cells have the relatively higher efficiency, good stability and easy to scale up. But the cost was still too high. Specially, the amorphous silicon based solar cells have low stability and difficult to scale up.

The other popular solar cells were thin film based solar cells, including the CIGS, and the III-V semiconductor based solar cells. The CIGS has high efficiency and good stability, but the fabrication processes were too complex, resulting in the high cost, and the failure in the industrial production. The III-V semiconductor based solar cells has the highest efficiency, about 45%, but the cost was too high, resulting in the few applications, such as satellites, spacecraft, etc.

Recent years, some new concept solar cells, including the dye-sensitized solar cells, the organic solar cells attracted more and more attention. The organic solar cells have low cost and good stability, but the efficiency was too low.

Compared with other kinds of solar cells, the dye sensitized solar cells have emerged as an important alternative to conventional silicon solar cells owing to their fascinating features such as low fabrication cost, good stability and relatively high efficiency [34-35]. Since the invention by O'Regan and Grätzel in 1991, DSSCs have been intensively studied and are currently undergoing rapid development for practical use [36].

A typical DSSC consists of four elements: a photoelectrode fabricated with the porous TiO_2 film deposited on conducting substrates (transparent conductive oxide, TCO glass), a dye molecule monolayer anchored on the surface of the TiO_2 film, a volatile liquid electrolyte containing I^-/I^{3-} redox couple and a platinized TCO glass as counter electrode, as shown in Fig.1.7.

The working principle of DSSC was shown in Fig 1.8. Photo-excitation of the dye

resulted in the injection of electrons into the conduction band of the semiconductor. The dye was regenerated by I^- in electrolyte. The I^- ions were regenerated in turn at the counter electrode by the reduction of I^{3-} with electrons which have passed through the external circuit. The voltage generated under illumination corresponds to the difference between the quasi-Fermi level of the electron in the semiconductor and the redox potential of the electrolyte. The net outcome was the conversion from light to electricity without any permanent chemical transformation.

In 1991, Swiss scientists firstly improved the conversion efficiency of the dye-sensitized solar cell to be 7.11% by using novel nanotechnology to fabricate nanocrystalline TiO_2 films on TCO glass as photoanode [37]. Since then, the dye-sensitized nanocrystalline solar cells was invented and quickly developed.

In 1993, Grätzel's group improved the conversion efficiency of the dye-sensitized solar cell to be 10.00% by using liquid electrolyte I^-/I_3^- and novel red dye, combined with nanocrystalline TiO_2 films [38].

In 1998, Tenakone's group obtained the DSSC conversion efficiency to be 4.5% by using CuI solid electrolyte and novel N3 dye, combined with nanocrystalline TiO_2 films [39].

In 2001, Hagfeldt et al used the low temperature process to fabricate the nanocrystalline TiO_2 films on the flexible substrates, obtaining the conversion efficiency of 5.2% [40].

In 2002, Hara's group firstly used the nature dye "coumarin" combined with the nanocrystalline TiO_2 films, liquid dye to fabricate the DSSC, getting the conversion efficiency of 5.6% [41]. The nature dye can help reducing the cost of dye and is environmental friendly.

Currently, the highest energy conversion efficiency of dye-sensitized solar cell was still made by the group of Prof. Grazel's group, above 15%, using the TiO_2/SnO_2 composites as the anode material, combined with the black dye N719 [42].

Figure 1.9 was shown the efficiency development of DSSC. The results indicated that the efficiency improvement of DSSC was encountered a bottleneck. The critical issues of dye-sensitized solar cells were to find the method to increase the efficiency significantly.

In recent years, the world continued to invest in the research of DSSC developments, mainly in two parts, the invention of new dye and the new material of the photoanode. In this thesis, I focused on the investigation of new photoanode material for DSSC.

1.2.2 ZnO-based dye-sensitized solar cell

In my research, we replaced the traditional TiO_2 films by the novel ZnO nanostructures. Compared with TiO_2, the ZnO has similar bandgap, much quicker electron transportation, and a variety of different nanostructures (indicating large internal surface area).

Currently, Germany Pasquier et al [43] obtained the conversion efficiency of the dye-sensitized solar cell to be 4.0% by using ZnO nanorods coated with TiO_2 as photoanode, and N719 dye, combined with liquid electrolyte I^-/I_3^-.

Mahmood et al [44] used the ZnO combined with the polyethylenimine (PEI) as photoanode, and obtained the DSSC conversion efficiency to be 5.0%. Fig. 1.10 showed the structure of this novel ZnO-based DSSC.

Barpuzary et al [45] combined the ZnO photoanode with the special designed SK1 dye. The conversion efficiency was up to 5.7%. The novel DSSC structure was shown in Fig. 1.11.

1.3 Objectives and structure of this thesis

In this dissertation, my main work focused on the fabrication of vertical well-aligned large surface ZnO nanostructures for dye-sensitized solar cell applications. There were three main requirements for ZnO nanostructures to be used in dye-sensitized solar cell applications:

(a) Vertical well-aligned ZnO nanostructures to obtain high transmittance and fast electron transportation.

(b) Large surface area to help absorbing more dye molecules.

(c) Conductive and transparent TCO substrates to help reducing the series resistance of the solar cell and increasing the transmittance.

In my research, there are several novel ideas solving these requirements:

1) Developing novel multi-annealing technique to fabricate vertical well-aligned ZnO nanostructures. (1 paper published)

2) Introducing the novel mist chemical vapor deposition (Mist CVD) technique to fabricate ZnO nanostructures with controllable morphology (1 paper published, 1 submitted paper)

3) High transmittance and conductivity ITO substrates for the photoanode of DSSCs. (1 submitted paper)

The structural of my thesis was shown in Fig. 1.12.

The main work and results of thesis will be exhibited by chapters one by one as

follows.

Chapter 1: The research background of ZnO including the history and current development was introduced in detail. The objectives of thesis were proposed as well as the outline of the thesis was built.

Chapter 2: The working principles and operation manual of fabrication and analysis equipment were introduced in this chapter.

Chapter 3-5: A variety of experimental methods were carried out for fabricating vertical well-aligned ZnO nanostructures. The characterization analysis of the results was discussed in detail.

Chapter 6: Vertical well-aligned ZnO nanostructures were applied as the photoanode material in the ye-sensitized solar cells.

Chapter 7: The main results obtained from this research work are summarized. The possible future research direction was point out.

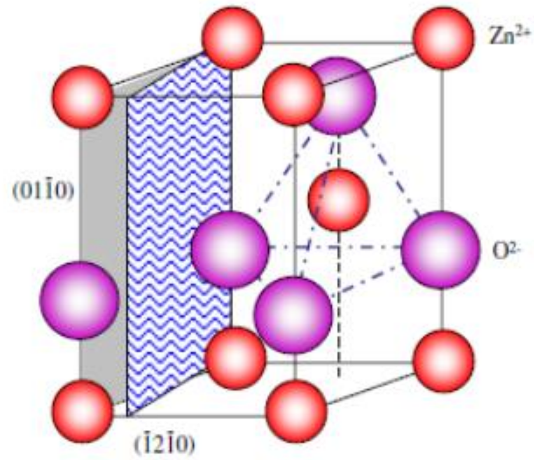

Fig. 1.1 The crystal structure of ZnO. [5]

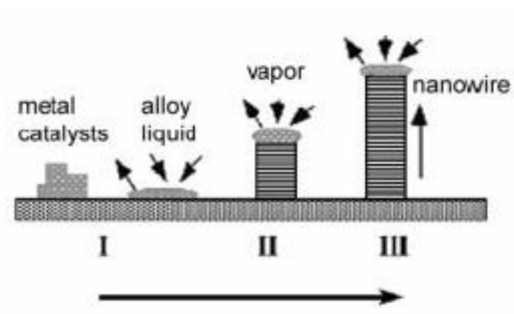

Fig. 1.2 The schematic diagram of VLS method.

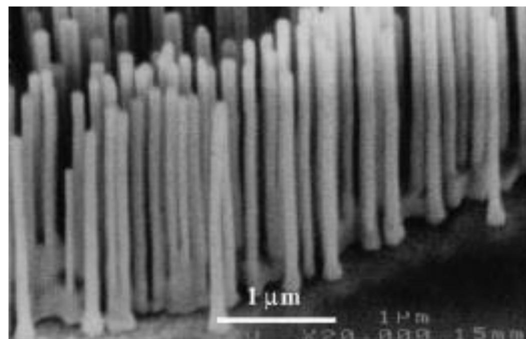

Fig. 1.3 The ZnO nanowires obtained by VLS method. [29]

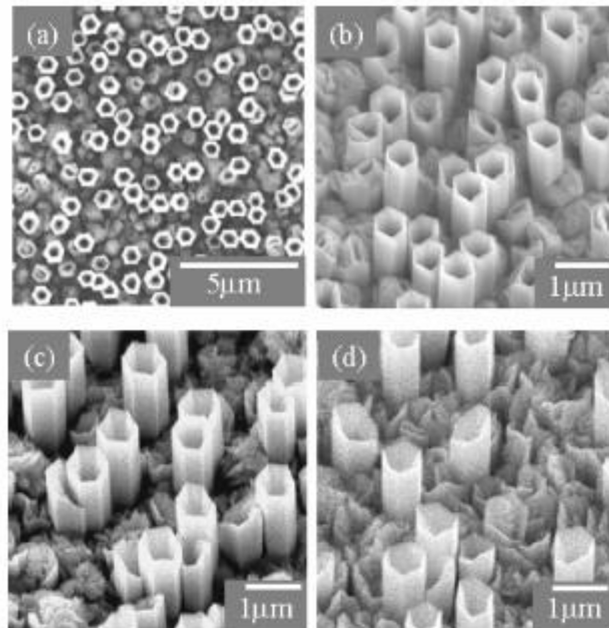

Fig. 1.4 The ZnO nanotubes fabricated by the MOCVD method. [30]

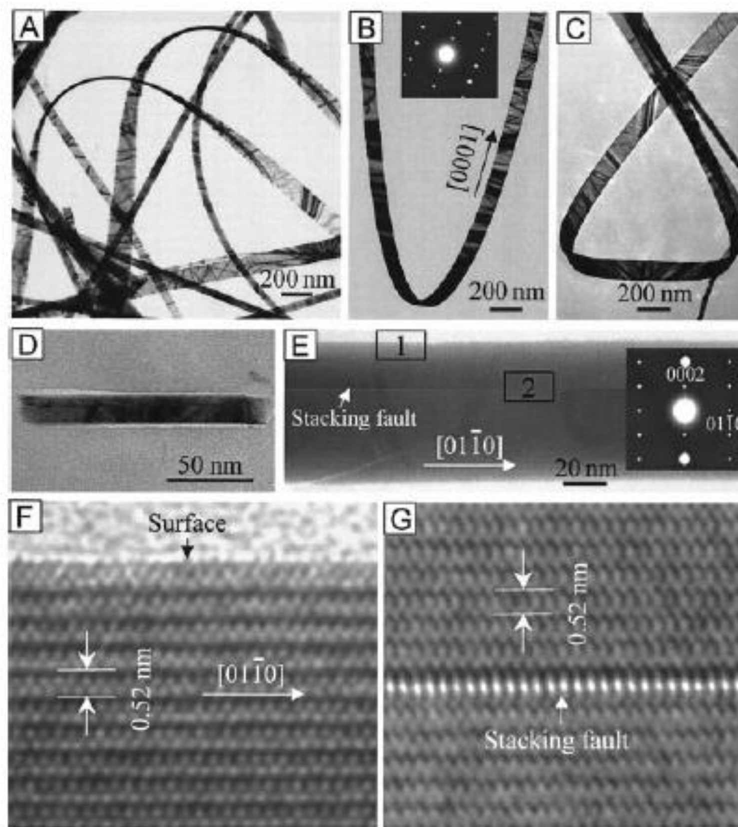

Fig. 1.5 The obtained ZnO nanobelts. [31]

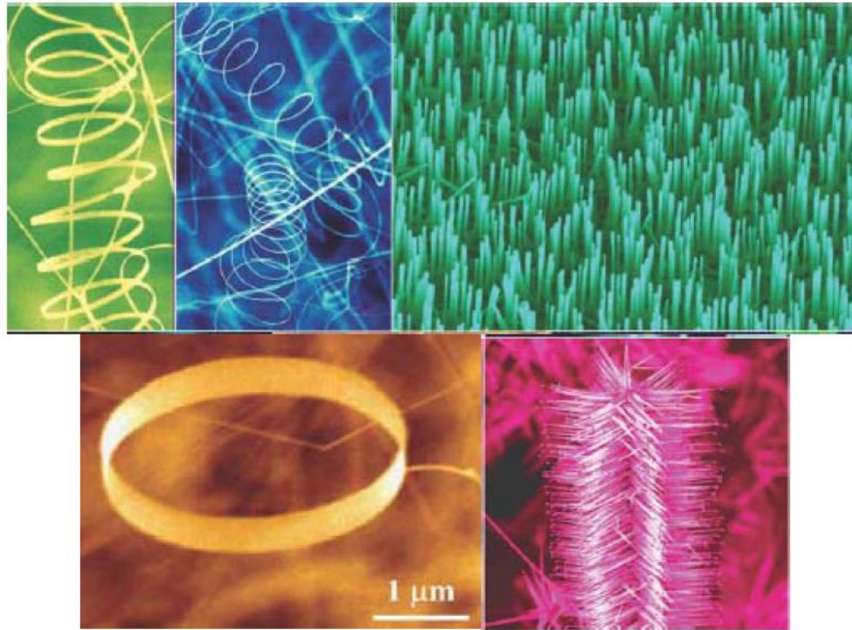

Fig. 1.6 The obtained different kinds of ZnO nanostructures. [31]

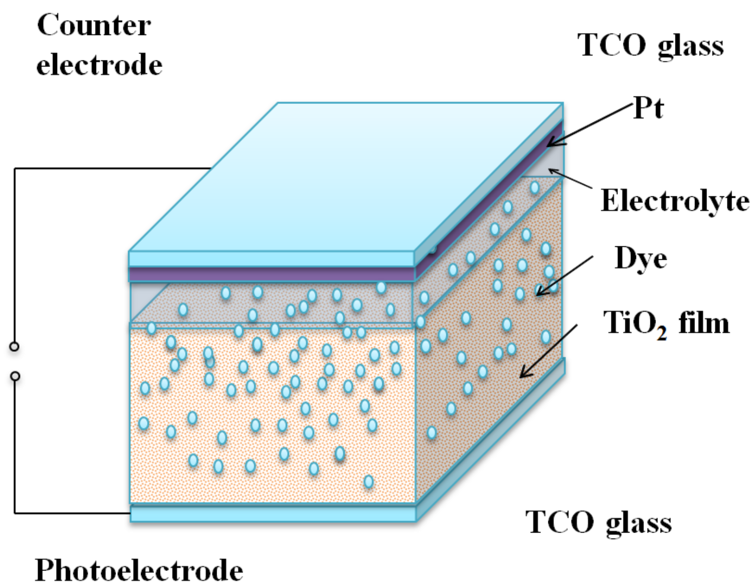

Fig. 1.7 The structure of traditional TiO_2-based dye-sensitized solar cell.

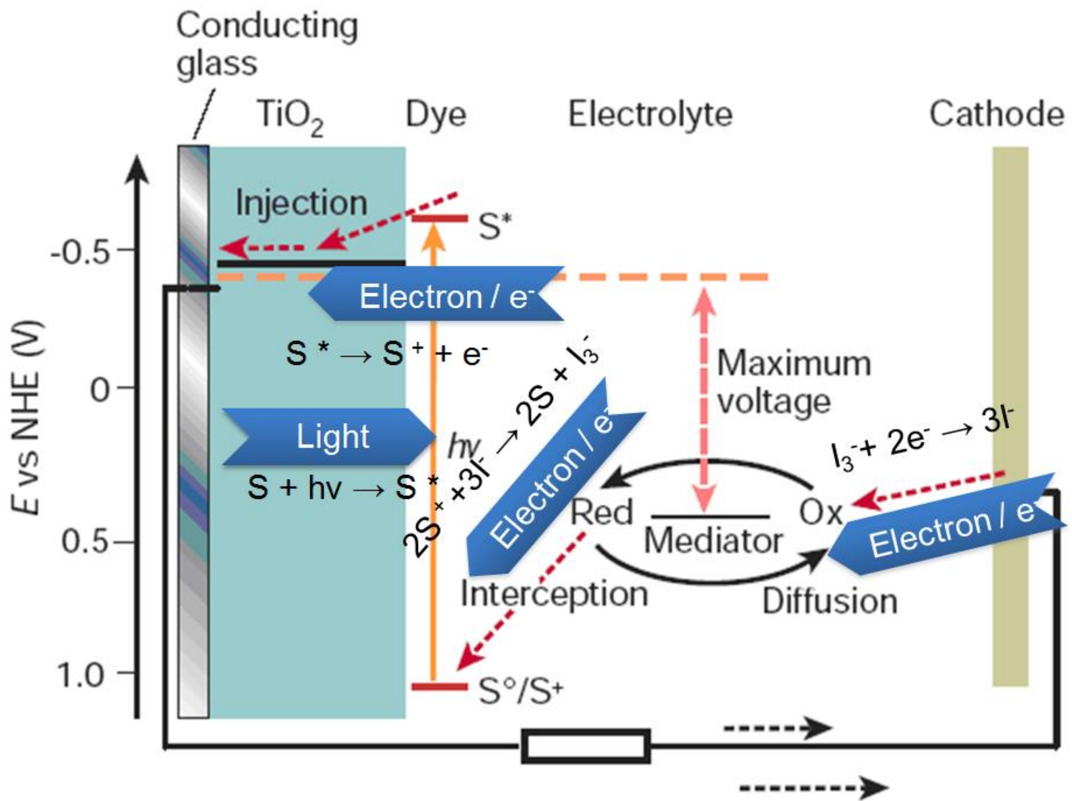

Fig. 1.8 The working principle of dye-sensitized solar cell.

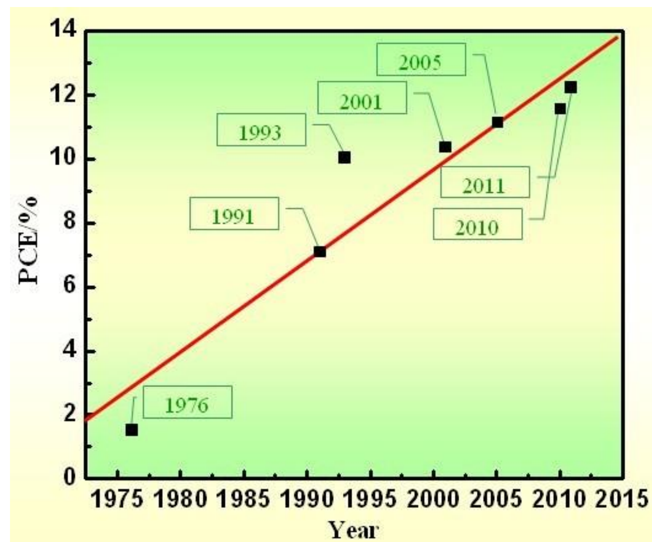

Fig. 1.9 The efficiency development of DSSC. [36]

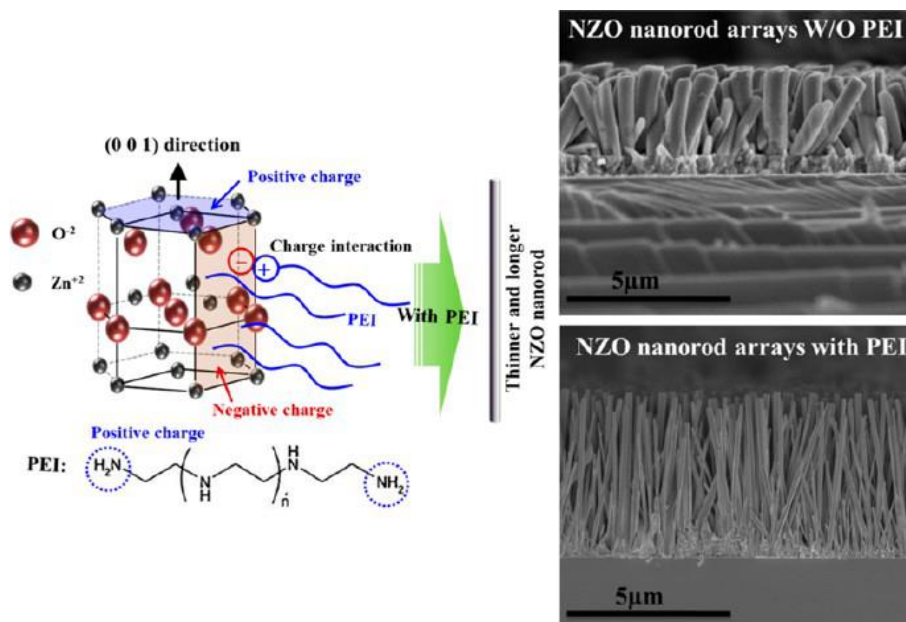

Fig. 1.10 The novel DSSC structure using ZnO/PEI as photoanode. [44]

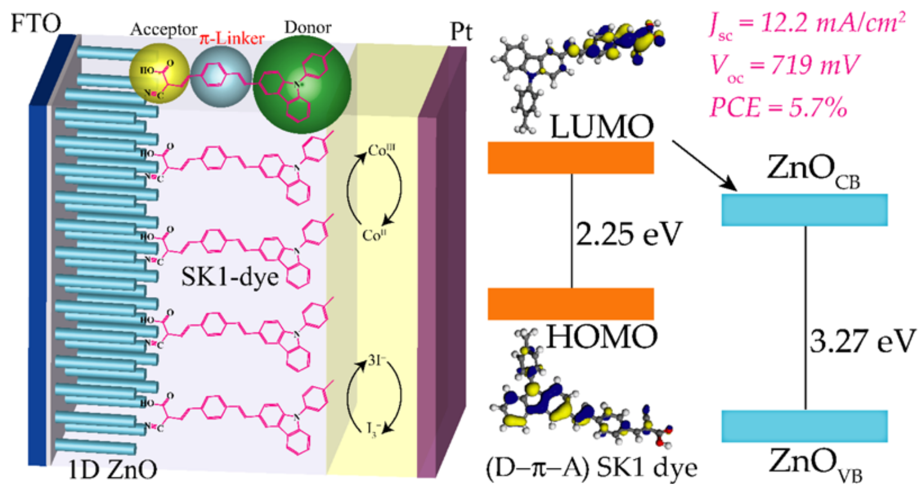

Fig. 1.11 The novel DSSC structure with ZnO photoanode and special designed SK1-dye. [45]

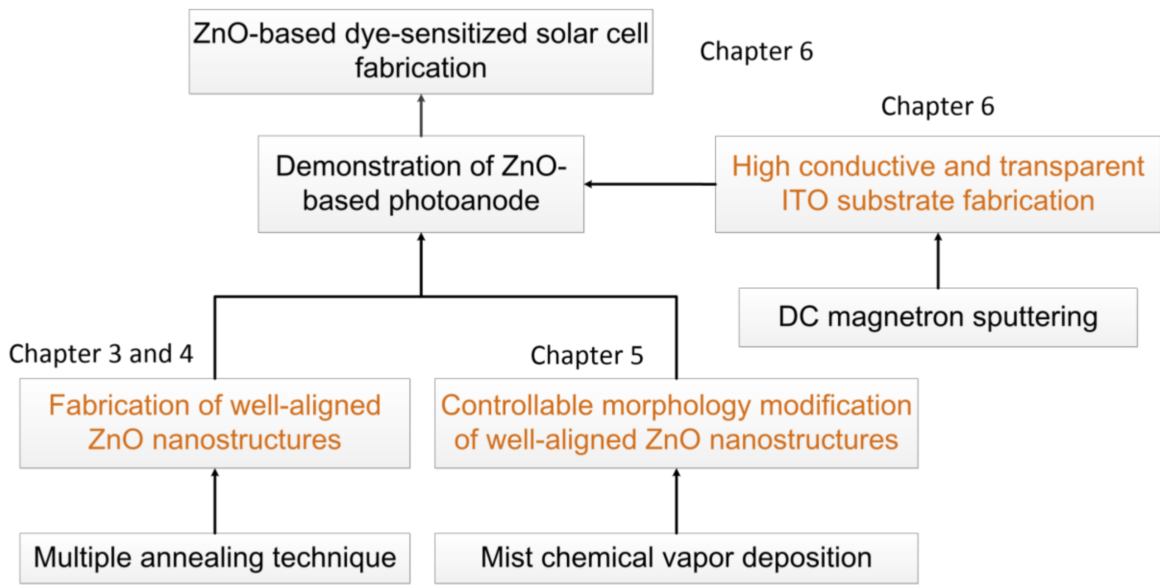

Fig. 1.12 The structure of my thesis.

Reference

1 Z. L. Wang, J. of Phys. C. Vol. 16 (2004) 829.

2 F. Laeri, F. Schuth, U. Simon, and M. Wark, "Host-Guest-Systems Based on Nanoporous Crystals", Wiley (2003).

3 Z. Fan and J. G. Lu, J. of Nanosci. and Nanotechnol. 5 (2005) 1561.

4 S. Baruah, and J. Dutta, Sci. Technol. Adv. Mater. 10 (2009) 1.

5 A. Cimino, G. Mazzone, and P. Porta, Z. Phys. Chem. (NF), 41 (1964) 154.

6 J.E. Jaffe, J.A. Snyder, Z. Lin, and A.C. Hess, Phys. Rev. B, 62 (2000) 1660.

7 S.K. Kim, S.Y. Jeong, and C.R. Cho, Appl. Phys. Lett. 82 (2003) 562.

8 Z. Shan, S. Li, C. B. Liang, and S.X. Mao, J. Cryst. Growth. 265 (2004) 482.

9 S. H. Kim, A. Umar, and Y. B. Hahn, J. Cryst. Growth. 277 (2005) 471.

10 Z. L. Wang, Materials Today. 7 (2004) 26.

11 S. Music, S. Popovic, M. Maljkovic, and D. Dragcevic, J. of Alloy. and Compd. 347 (2002) 324.

12 J. Zhang, Y. Yang, and J. Li, J. Cryst. Growth. 280 (2005) 509.

13 T. K. Subramanyam, B. S. Naidu, and S. Uthanna, Cryst. Res. Technol. 35 (2000) 1194.

14 C. Yang, X.M. Li, X.D. Gao, X. Cao, R. Yang, and Y.Z. Li, J. Cryst. Growth 312 (2010) 978.

15 H. Tanaka, S. Fujita, and S. Fujita, Appl. Phys. Lett. 86 (2005) 192911.

16 H. Li, Y.Z. Zhang, X.J. Pan, T. Wang, and E.Q. Xie, J. Alloys Compd. 472 (2009) 208.

17 R. L. Hoffman, B. J. Norris, and J. F. Wager, Appl.Phys.Lett. 82 (2003) 733.

18 X. Sun, and J. Wang, J. Nano lett. 8 (2008) 1884.

19 T. Kawaharamura, Dr. Thesis, “Study on mist CVD method and its application to the growth of ZnO thin films” Kyoto-Univ., 2008.

20 H. Ohta, M. Orita, M. Hirano, and H. Hosono, J. Appl. Phys. 89 (2001) 5720.

21 A. Tsukazaki, M. Kubota, A. Ohtomo, T. Onuma, K. Ohtani, H. Ohno, S.F. Chichibu, and M. Kawasaki, Jpn. J. Appl. Phys. 44 (2005) L643.

22 M. Furuta, Y. Kamada, M. Kimura, T. Hiramatsu, T. Matsuda, H. Furuta, C. Li, S. Fujita, and T. Hirao, IEEE Electr. Device Lett. 31 (2010) 1257.

23 Q. P. Wang, D.H. Zhang, H. L. Ma, X. H. Zhang, and X. J. Zhang, Appl. Surf. Sci. 220 (2003) 12.

24 K. Ito and T. Nakazawa, Jpn. J. Appl. Phys. 22 (1983) L245.

25 Y. J. Xing, Z.H. Xi, Z.Q. Xue, X.D. Zhang, J.H. Song, R.M. Wang, J. Xu, Y. Song, S.L. Zhang, and D.P. Yua, Appl. Phys. Lett. 83 (2003) 1689.

26 C. Y. Li, T. Matsuda, T. Kawaharamura, H. Furuta, M. Furuta, T. Hiramatsu, and T. Hirao, J. Vac. Sci. Technol. B. 28 (2010) C2B51.

27 L. Vayssieres. Adv. Mater. 15 (2003) 464.

28 M.H. Huang, S. Mao, H. Feick, H.G. Yan, Y.Y. Wu, H. Kind, E. Weber, R. Russo, and P.D. Yang, Science, 292 (2001) 1897.

29 Y. Yang, J. L. Wang, and W. C. Tsai, Thin Solid Films, 518 (2010) 7328.

30 Y. Y. Zhang, Phys. Rev. B. 80 (2009) 094528.

31 W. Pan, Z.R. Dai, Z.L. Wang, Science, 291 (2001) 1947.

32 C. Y. Li, T. Kawaharamura, T. Matsuda, H. Furuta, T. Hiramatsu, M. Furuta, and T. Hirao. J. Appl. Phys. Express. 2 (2009) 091601.

33 X. Li, C. Y. Li, T. Kawaharamura, D. P. Wang, N. Nitta, M. Furuta, H. Furuta and A. Hatta, Trans. Mat. Res. Soc. 28(2013).

34 M. Grätzel, Inorg. Chem. 44 (2005) 6841.

35 B. C. O’Regan, K. Bakker, J. Kroeze, H. Smit, P. Sommeling, and J. R. Durrant, J. Phys. Chem. B 110 (2006) 17155.

36 M. Grätzel, Prog. Photovolt: Res. Appl. 14 (2006) 429.

37 B. O’Regan, and M. Grätzel, Nature, 353 (1991) 737

38 M. K. Nazeeruddin, A. Kay, I. Rodicio, R. Baker, E. Mueller, P. Liska, N. Vlachopoulos, and M. Graetzel, J. A. C. S. 115 (1993) 6382.

39 K. Tennakone, J. Phys. D: Appl. Phys. 31 (1998) 1492.

40 A. Hageldt, and M. Gätzel, Chem. Rev. 95（2001）49.

41 K. Hara, T. Sato, R. Katoh, A. Furube, Y. Ohga, A. XShinpo, S. Suga, K. Sayama, H. Sugihara, and H. J. Phys. Chem. B. 107 (2003) 597-606.

42 J. Burschka, N Pellet, S. J. Moon, R. Baker, P. Gao, M. Nazeeruddin, and M. Gratzel, Nature. 499 (2013) 316.

43 S. Pasquier, D. P. Norton, K. Ip, Y. W. Heo, and T. Steiner, Prog. in Mater. Sci., 50 (2005) 293.

44 D. Barpuzary, A. S. Patra, J. V. Vaghasiya, B. G. Solanki, S. S. Soni, and M. Qureshi. ACS appli. Mater. & interf. 78(2014) 841.

45 K. Mahmood, B. S. Swain, G. S. Han, B. J. Kim, and H. S. Jung. ACS appli. Mater. & interf. 79 (2014) 954.

Chapter 2

Fabrication and characterization

In this chapter, the formation and evaluation equipment were briefly introduced. The thin films were prepared by radio frequency magnetron sputtering system. The post-treatment processes were applied in the conventional quartz annealing furnace. The morphology modification was carried out in the Mist CVD system.

Following the fabrication procedure, a number of characterizations were applied to evaluate the structural, electric and optical properties. The structural properties were inspected using X-ray diffraction. A field emission scanning electron microscope (FE-SEM) and a transmission electron microscope (TEM) system were used to characterize the surface morphology and the microstructure. The surface morphology and the root-mean-square (rms) surface roughness were characterized using an atomic force microscope (AFM). The luminescent characteristics were measured by photoluminescence (PL) measurement. Optical transmission spectra measurements were performed using UV-visible spectrophotometer. The electrical property was measured using a Hall measurement system.

All the measurement were carried out in the room temperature

2.1 Fabrication equipment

2.1.1 Radio frequency magnetron sputtering system

Sputtering is the physical deposition technique to deposite thin films. Due to the low

cost, easy to scale up, and low working temperature, the sputtering was widely applied in both research and industry [1]. Our sputtering system contained the high vacuum system, the sputtering system, the heating system, and the samples delivery system. Fig. 2.1 showed the schematic diagram of RF sputtering system [2].

If a solid is subjected to bombardment by the particles with suitable energy, the surface atoms can acquire enough energy from collision processes to escape, which is known as "*sputtering*". Sputtering sources often employ magnetrons that utilize strong electric and magnetic fields to confine charged plasma particles close to the surface of the sputter target [2-3]. The sputter gas is typically an inert gas such as argon. The extra argon ions created as a result of these collisions leads to a higher deposition rate. It also means that the plasma can be sustained at a lower pressure. The sputtered atoms are neutrally charged and so are unaffected by the magnetic trap. Charge build-up on insulating targets can be avoided with the use of RF sputtering where the sign of the anode-cathode bias is varied at a high rate.

In this thesis, ZnO and related films were deposited by the conventional RF magnetron sputtering system using argon and air as working gases as well as ZnO as target.

2.1.2 Commercial annealing furnace

The figure of the annealing furnace was shown in Fig. 2.2. This commercial annealing furnace, one of oven type equipment, is used for the post-treatment of different materials. The furnace contained a quartz tube, the heater, vacuum system, and cooling system.

The conventional annealing furnace has a heating temperature range RT (room temperature) ~ 800 ℃. The environmental gases were N_2, Ar, O_2 and forming gas. The

quartz boat was set in the center of the furnace, which was used to support the treated samples [4].

In this thesis, the annealing furnace was used to anneal sample with different ambient.

2.1.3 Mist CVD system

The Mist CVD was a novel chemical vapor deposition method. The schematic diagram of Mist CVD was shown in Fig. 2.3[5]. The Mist CVD system contained three parts: (1) the source supply unit: the material solution was sonicated to form micro mist droplets by ultrasonic transducer. (2) the transportation unit: the mist droplets were transferred from source supply unit to reaction unit by carrier gas and dilution gas. (3) the reaction unit: the thin film or nanostructures were forming in here.

This technique has several advantages. Firstly, the micro mist droplets in several micrometers will be not recombined during the transport process due to the special design of the internal shape of the reaction portion,; therefore, the "stable material" such as the oxide material can be treated as the gas (mist droplets in several micrometers) to be used in the chemical vapor deposition.

In this thesis, the Mist chemical vapor deposition was used to modify the surface area of the ZnO nanostructures.

2.2 Characterization techniques

2.2.1 X-ray diffraction

The XRD system (ATX-G) containes the X-ray source, the optical focus system, the sample holder, and the detector. The schematic diagram of X-ray diffractometer (XRD) optical system was in Fig. 2.4[6].

X-ray diffraction is one of the most popular devices in the materials research, which

usually employed a copper target to generate X-ray (Kα) with the wavelength 1.54056Å. Crystals are regular arrays of atoms, and X-rays can be considered waves of electromagnetic radiation. Atoms scatter X-ray waves, primarily through the atoms' electrons. The X-ray striking an electron produces secondary spherical waves emanating from the electron. This phenomenon is known as elastic scattering, and the electron is known as the scatterer [7]. A regular array of scatterers produces a regular array of spherical waves, determined by Bragg's law:

$$2d\sin\theta = n\lambda$$

Here d is the spacing between diffracting planes, θ is the incident angle, n is any integer, and λ is the wavelength of the beam.

These specific directions appear as spots on the diffraction pattern called reflections. Thus, X-ray diffraction results from an electromagnetic wave (the X-ray) impinging on a regular array of scatterers (the repeating arrangement of atoms within the crystal).

Till now, over 80,000 materials have been enrolled into the International Powder Diffraction File (PDF) database as the Joint Committee for Powder Diffraction Standards (JCPDS) [7]. If the XRD patterns were obtained, we can compare the experiments data with the standard data. Then, the information about the peak position, the composition and lattice distortion can be easily calculated.

In my thesis, the XRD was used to determine the crystalline phase of the material, calculate the distance between the lattice, the direction and lattice of the sample.

2.2.2 Field emission scanning electron microscope

The field emission scanning electron microscope (FE-SEM) system (JEOL-JSM7400F) contains the vacuum system, the electron gun, the focus coils, and the detectors as shown in Fig. 2.5.

The schematic diagram of SEM is exhibited in Fig. 2.6[8]. A typical field emission microscope consists of a metallic sample in the form of a sharp tip and a conducting fluorescent screen enclosed in ultrahigh vacuum. The tip radius used is typically of the order of 100 nm. It is composed of a metal with a high melting point, such as tungsten. The sample is held at a large negative potential (1-50 kV) relative to the fluorescent screen. This gives the electric field near the tip apex to be the order of 10^{10} V/m which is high enough for field emission of electrons to take place [9].

The elemental composition of the specimen can be identified by energy dispersive X-ray spectroscopy (EDS). The EDS analysis system works as an integrated feature of a scanning electron microscope (SEM), and cannot operate on its own without the latter.

In my thesis, the SEM was used to observe the morphology and microstructure of the samples. The EDS was used to analyze the element distribution in the samples [10].

2.2.3 Photoluminescence spectroscopy

The photoluminescence (PL) measurement is carried out by an iHR320 Micro-PL/Raman spectroscope (Horiba Ltd.), which containes a He-Cd laser as the light source, a set of gratings, and the detectors.

The schematic diagram of PL is exhibited in Fig. 2.7[11]. In a typical PL system, a semiconductor sample is excited by a light-source which provided photons with energy larger than the bandgap energy. Once the photons are absorbed, electrons and holes are formed with finite momenta in the conduction and valence bands, respectively. The excitations then undergo energy and momentum relaxation towards the band gap minimum. Typical mechanism is Coulomb scattering and the interaction with phonons. Finally, the electrons recombine with holes under emission of photons [12].

Ideally, defect-free semiconductors are quantum many-body systems where the

interactions of charge-carriers and lattice vibrations have to be considered in addition to the light-matter coupling. In general, the PL properties are also extremely sensitive to internal electric fields and to the dielectric environment which impose further degrees of complexity. A precise microscopic description is provided by the semiconductor luminescence equations [13].

In this thesis, the PL system was used to obtain the photoluminescence spectra of the samples to help analyzing the optical properties of the samples.

2.2.4 Transmission emission microscope

The transmission electron microscope (TEM) system (JEOL-2100F) contains the high vacuum system, the high voltage electron gun, the focus coils, the detectors, and EDX system, as shown in Fig. 2.8.

The schematic diagram of TEM is exhibited in Fig. 2.9[14]. The Transmission electron microscopy (TEM) is a microscopy technique in which a beam of electrons was transmitted through an ultra-thin specimen, interacting with the specimen as it passes through [15-16]. An image is formed from the interaction of the electrons transmitted through the specimen; the image is magnified and focused onto an imaging device, such as a fluorescent screen, on a layer of photographic film, or to be detected by a sensor such as a CCD camera.

TEMs are capable of imaging at a significantly higher resolution than light microscopes, owing to the small de Broglie wavelength of electrons.

In my thesis, the TEM was used to observe the morphology and microstructure of the samples. The EDX was used to analyze the element distribution in the samples [10].

2.2.5 Atomic force microscopy

The atomic force microscope (AFM) (Nanoscope II, Digital Instruments) contained

the sample holder, a laser and the needle detector, as shown in Fig. 2.10.

The schematic diagram of AFM is exhibited in Fig. 2.11[17]. The AFM consists of a cantilever with a sharp tip (probe) at its end that is used to scan the specimen surface. The cantilever is typically the silicon or the silicon nitride with a tip radius of curvature on the order of nanometers.

When the tip is brought into proximity of a sample surface, forces between the tip and the sample lead to a deflection of the cantilever according to Hooke's law [18]. Depending on the situation, forces that are measured in AFM include mechanical contact force, van der Waals' forces, capillary forces, chemical bonding, electrostatic forces, magnetic forces, Casimir forces, solvation forces, etc. Along with force, additional quantities may simultaneously be measured through the use of specialized types of probes [19].

Typically, the deflection is measured using a laser spot reflected from the top surface of the cantilever into an array of photodiodes. Other methods that are used include optical interferometry, capacitive sensing or piezoresistive AFM cantilevers.

In this thesis, the AFM was applied to measure the surface morphology of samples.

2.2.6 Hall measurement device

The electrical properties of materials are measured by using a Hall measurement system (Accent HL5500, M-1), as shown in Fig. 2.11. This Hall system contained a four-probe detector, a magnetron system and the heating system.

The schematic diagram of Hall Effect is showed in Fig. 2.13[20].The Hall Effect is the production of a voltage difference (the Hall voltage) across an electrical conductor, transverse to an electric current in the conductor and a magnetic field perpendicular to the current.

The Hall Effect is due to the nature of the current in a conductor. Current consists of the movement of many small charge carriers, typically electrons, holes, ions or all three. When a magnetic field is present that is not parallel to the direction of motion of moving charges, these charges experience a force, called the Lorentz force. When such a magnetic field is absent, the charges follow approximately straight, 'line of sight' paths between collisions with impurities, phonons, etc. [21].

In this thesis, the Hall measurement was applied to measure the electrical properties of the samples.

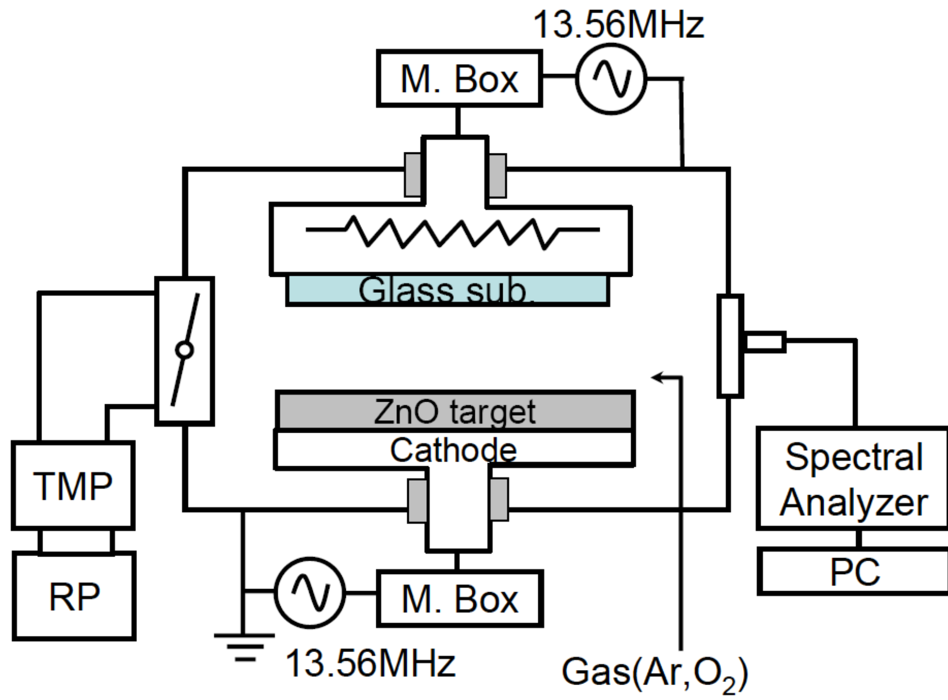

Fig. 2.1 The schematic diagram of RF sputtering.

Fig. 2.2 The annealing furnace.

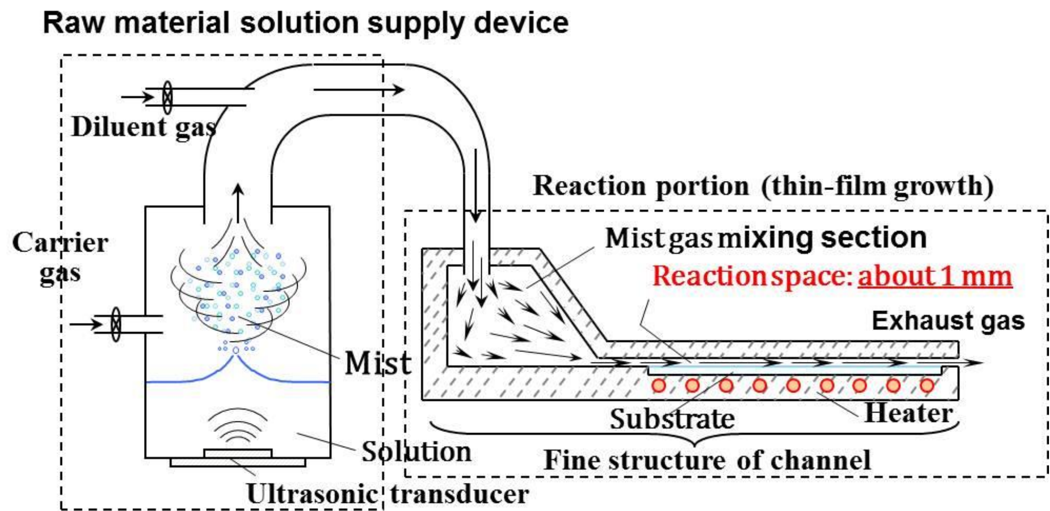

Fig. 2.3 The Mist CVD system. [5]

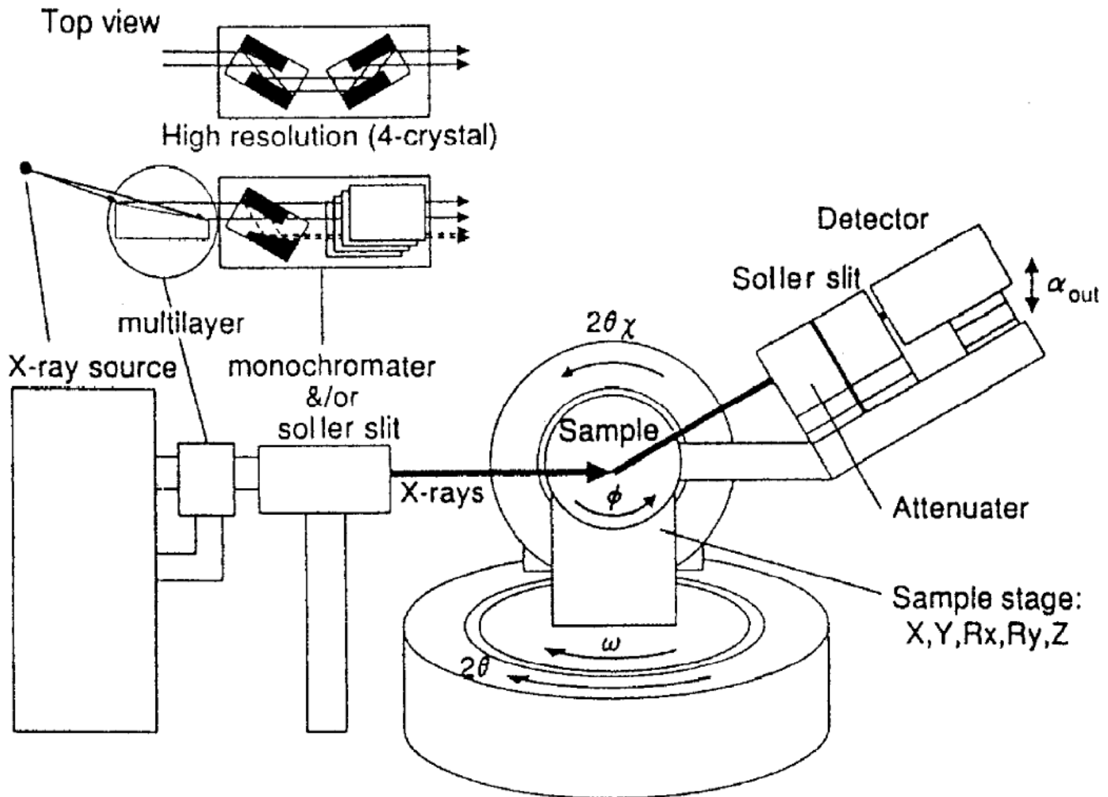

Fig. 2.4 The schematic diagram of XRD. [6]

Fig. 2.5 The JEOL-JSM7400F SEM system.

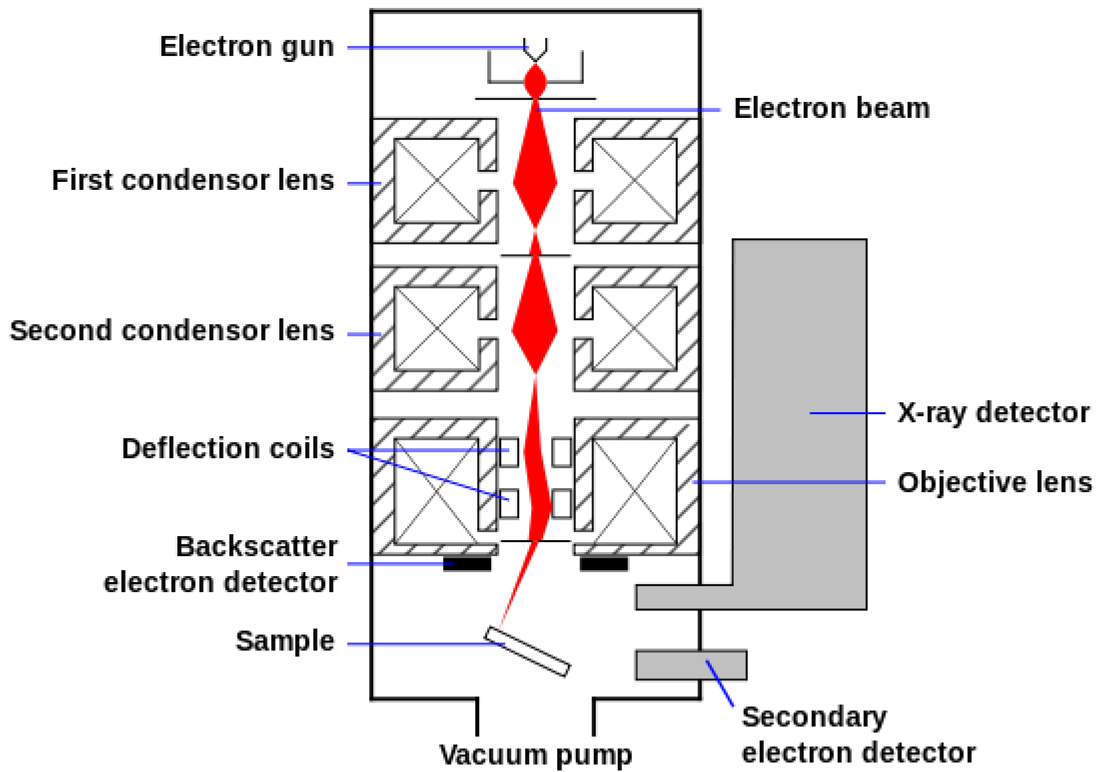

Fig. 2.6 The schematic diagram of JEOL-JSM7400F SEM. [8]

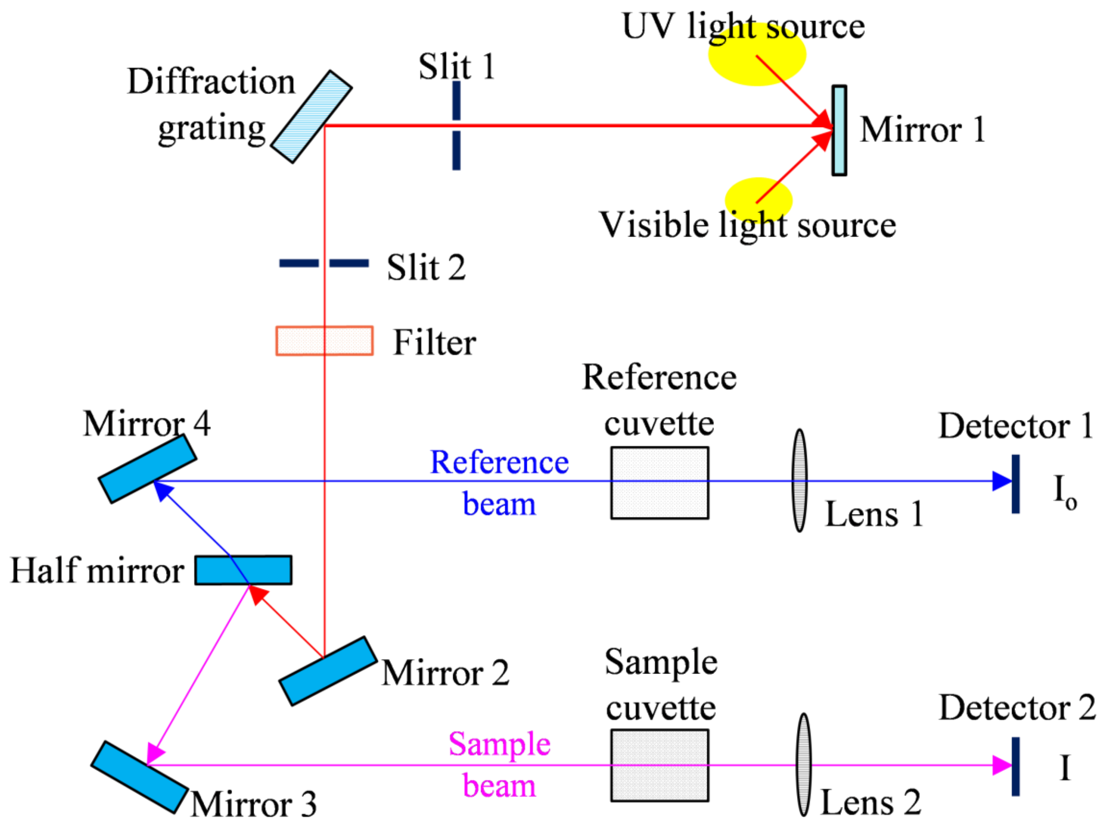

Fig. 2.7 The schematic diagram of PL system. [11]

Fig. 2.8 The JEOL-2100F TEM system.

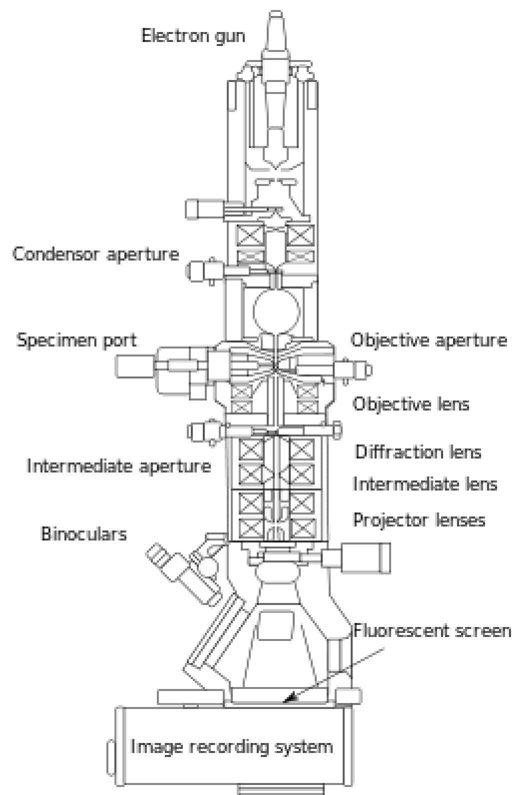

Fig. 2.9 The schematic diagram of TEM system. [14]

Fig. 2.10 The Nanoscope II AFM system

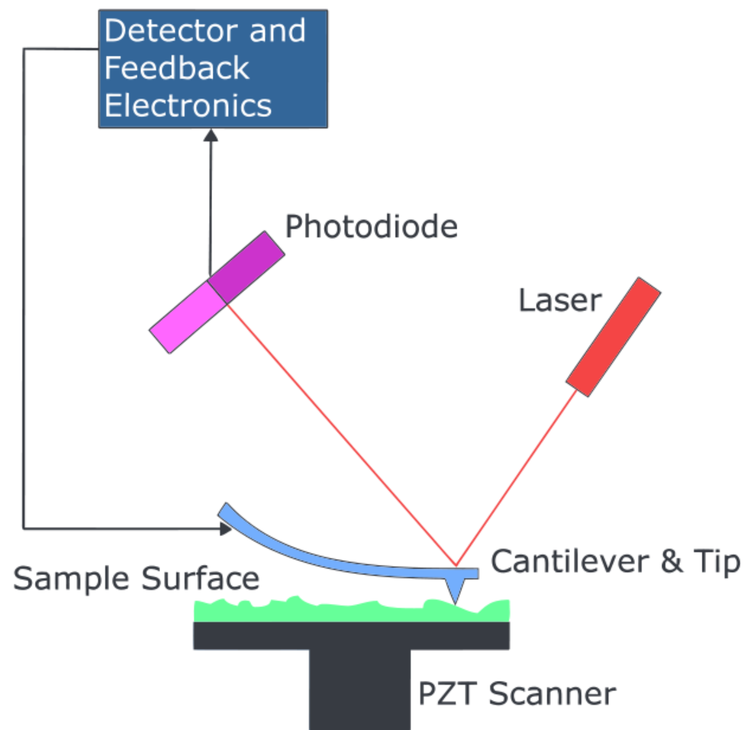

Fig. 2.11 The schematic diagram of AFM system. [17]

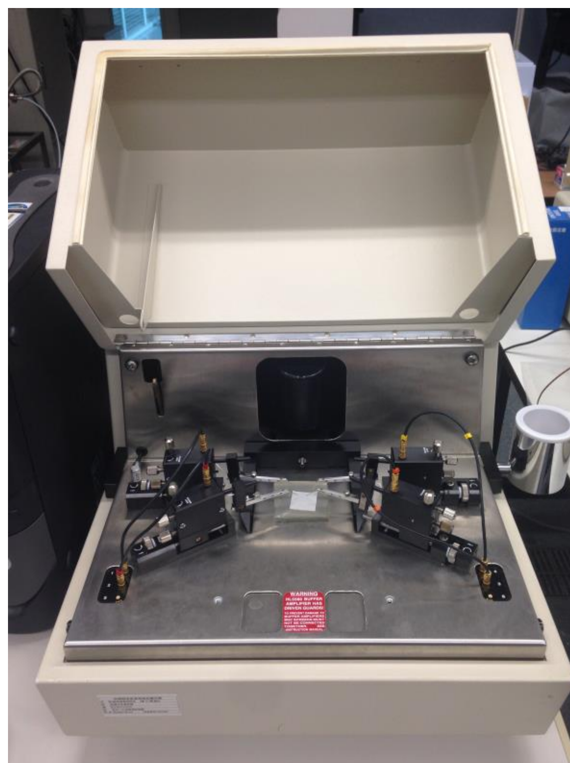

Fig. 2.12 The Accent HL5500 Hall system.

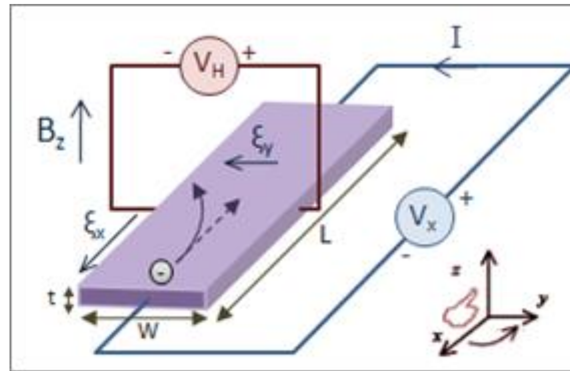

Fig. 2.13 The schematic diagram of Hall system. [20]

Reference

1 J. L. Vossen, Phys. Thin Films, 9 (1977) 1.

2 C. Y. Li, T. Matsuda, T. Kawaharamura, H. Furuta, M. Furuta, T. Hiramatsu, and T. Hirao, J. Vac. Sci. Technol. B. 28 (2010) C2B51.

3 C. Y. Li, M. Furuta, T. Matsuda, T. Hiramatsu, H. Furuta, and T. Hirao, Thin Solid Films, 517 (2009) 3265.

4 D. P. Wang, Z. M. Li, T. Kawaharamura, M. Furuta, T. Narusawa, and C. Y. Li, Phys. stat. Sol. (c). 9 (2012) 491.

5 T. Kawaharamura, Dr. Thesis, "Study on mist CVD method and its application to the growth of ZnO thin films" Kyoto-Univ., 2008.

6 J. M. Jensen, A. B. Oelkers, R. Toivola, D. C. Johnson, J. W. Elam, and SM. George, Chem. Mater. 14 (2002) 2276.

7 B. Cheng, and E.T. Samulski, Chem. Comm. 21 (2004) 986.

8 http://en.wikipedia.org/wiki/Scanning_electron_microscope.

9 L. L. Yang, Dr. Thesis, "Synthesis and characterization of ZnO nanostructures" Linkoping-Univ. Sweden, 2010.

10 http://serc.carleton.edu/research_education/geochemsheets/eds.html

11 http://www.itst.ucsb.edu/~vinhnguyen/Time-Frequency_Spectroscopy.htm

12 Q. Y. Wan, X. Gao, and J. Li, Appl. Phys. Lett. 7 (2004) 3014.

13 D. Kan, T. Terashima, R. Kanda, and Y. Shimakawa, Nature, 4 (2005) 816.

14 http://en.wikipedia.org/wiki/Transmission_electron_microscopy

15 R. F. Egerton, “Electron Energy-loss Spectroscopy in the Electron Microscope”. Springer. 1996.

16 J. Frank. “Electron tomography: methods for three-dimensional visualization of structures in the cell”. Springer. 2006

17 http://en.wikipedia.org/wiki/Atomic_force_microscopy

18 G. Binnig, C. F. Quate, and C. Gerber, Phys. Rev. Lett. 56 (1986) 930.

19 R. V. Lapshin, Nanotechnology, 15 (2004) 1135.

20 http://en.wikipedia.org/wiki/Hall_effect

21 A. Baumgartner, Phys. Rev. B, 74 (2006) 165426.

Chapter 3

Fabrication of vertical well-aligned ZnO nanostructures by single annealing process

3.1 Introduction

As one of the most promising II-VI compound semiconductors, ZnO with wide have attracted much more interest to be used as photoelectrode in photovoltaic applications, due to the wide bandgap energy of 3.37eV and high electron mobility (up to 1000 cm^2 /V s) [1-6].

For the photovoltaic devices, the transmittance of photoanode was a very important parameter for the improvement of conversion efficiency. The high transmittance of photoanode required the anode material having the uniform and smooth morphology and good crystallinity to reduce the scattering and loss of the light. For the case of ZnO nanostructures, the vertical well-aligned morphology with good crystallinity was needed to reduce the scattering and loss of the light.

In order to increase the conversion efficiency of photovoltaic devices, the alignment of ZnO nanostructures should be well controlled during the fabrication processes.

A number of methods have been used to fabricate ZnO nanostructures, such as chemical vapor deposition, vapor-phase transport, pursed-laser deposition, thermal evaporation [7-12].However, these methods always have some disadvantage including the complex process, low reproducibility, high cost, difficult to scale up and pollution to

the environment, leading to the failures in the industrial applications. Therefore, a novel technique to fabricate controlled vertical well-aligned ZnO nanostructures was still needed.

In our previous work, we have many experiences on the fabrication of high quality ZnO thin film using RF magnetron sputtering [13-15]. In recent years, we had succeeded in obtaining the hexagonal-cone ZnO nanostructures on ZnO film using low-temperature treatment in a reducing gas ambient which was very different technique from other techniques [16-17].

Until now, there are many reports on the evaluation of ZnO thin films [18-22], most attentions were paid to the influences of deposition conditions on the properties of ZnO films rather than the substrate selection. Most of the research on deposition of ZnO thin films on different substrates including glass, quartz glass, silicon, sapphire, aluminum and copper focused on the deposition parameter optimization [23-28].There are few reports on the selection of substrates and the effects of substrates on the ZnO thin films. As our experience, by our technique, ZnO nanostructures can be fabricated on ZnO films which were formed on different substrates. The vertical alignment, morphology and properties of ZnO nanostructures were affected by the substrates. The properties of as-deposited ZnO films are significantly influenced by the substrates, such as the crystal orientation, the conductivity, the stability, as well as the inherent property. Thus, the investigation of the role of substrates on the fabrication of ZnO films and ZnO nanostructures were urgently needed.

Therefore, several substrates were used for the fabrication of ZnO films and well-aligned nanostructures to investigate the role of the substrates on the fabrication of ZnO nanostructures and discuss the grow mechanism of the vertical well-aligned ZnO

nanostructures.

In the first part of this chapter, the reducing annealing technique was introduced. The influence of the substrate on the fabrication of well-aligned nanostructures was discussed.

As we know, the annealing temperature has great influence on the physical and sometimes chemical properties of a material. Therefore, it's very important to investigate the dependence of the growth of ZnO nanostructure on the temperature to discuss the growth mechanism of the ZnO nanostructures.

In the second part of this chapter, the effect of annealing temperature on the obtained ZnO nanostructure was discussed.

3.2 Substrates dependence

3.2.1 Experiments

ZnO thin films (500nm) were deposited by a conventional 13.56 MHz radio frequency (RF) magnetron sputtering system [17]. A 4-inch ZnO ceramic target (99.999% ZnO) was located on the cathode 60mm away from the substrate stage. The background pressure in the sputtering chamber was evacuated to about 6×10^{-5} Pa with a turbo molecular pump. The RF power was 180 W. The deposition processes were performed in an Ar ambient (30 sccm) controlled by a mass flow controller. The working pressure was maintained at 7 Pa. The substrate temperature on the anode was preheated to 150 ℃ for 20min prior to deposition and was fixed during the deposition procedure. In order to compare the effect of substrates, the four different substrates were selected as comparison: Qz glass, silicon (100) wafer, sapphire (0001), FTO glass.

Following the deposition procedure, ZnO thin film was put into a conventional furnace at low temperature annealing in a reducing gas ambient. The ZnO films were

treated at 450 ℃ for 5h in reducing gas (1.9% H_2 in N_2).

3.2.2 Results and discussion

3.2.2.1 The influence of substrates on the fabrication of ZnO films

Figure 3.1(a) showed the XRD patterns of the ZnO films (500 nm in thickness) deposited on four different substrates under the same deposition conditions.

The X-ray diffraction analysis revealed that only the (002) reflection peak could be observed for all films, meaning that all of the as-deposited ZnO films had highly (002) preferred orientation with a c-axis perpendicular to the substrates. However, the peak intensities of ZnO films were significantly different.

The crystallinity of ZnO film was improved gradually in the films deposited in order of Qz glass, FTO glass, sapphire and silicon. ZnO film deposited on the silicon showed the highest (002) peak intensity. The different peak intensities of the ZnO films indicated that the film crystallinity was significantly influenced by the substrate materials.

Figure 3.1(b) showed the relationship between the c-axis crystallite size, the FWHM and the different substrates.

It was found that the FWHM value was decreased in the opposite order of the peak intensity increase. The sharpest FWHM value 0.215°was obtained from the ZnO film deposited on silicon substrate. With Scherrer's equation [32-33], the c-axis crystallite size could be calculated by the FWHM value. The crystallite sizes of the ZnO films on the Qz glass, FTO glass, sapphire and silicon increased from 26.7nm to 27.7nm, 29.5nm and 38.3nm, respectively, exactly as same order as the increase of XRD peak intensity of the ZnO films. Therefore, the XRD result showed the crystallinity was improved with the ZnO film deposited on the substrates in the order of Qz glass, FTO glass, sapphire

and silicon.

The dependence of lattice constant c and compressive stress of as-deposited ZnO films on different substrates was shown in Fig. 3.2.

It was found that the lattice distortion of constant c on different substrates decreased in the order of the increase of crystallinity. The crystalline substrates, silicon and sapphire showed lower lattice distortion than the other two substrates.

ZnO film on silicon substrate showed the lowest lattice distortion, which was much close to the standard lattice constant c (0.52062nm). ZnO films deposited on different substrates showed compressive stress with an increase in order of silicon, sapphire, FTO glass and glass. The most relax film was obtained from the film deposited on silicon substrate. The results revealed that the improvement of crystallinity of the ZnO films led to a decrease in the lattice distortion and compressive stress of the ZnO films.

Figure 3.3 (1-a) to (4-a) showed the top view SEM images of as-deposited ZnO films obtained from RF magnetron sputtering.

It was observed that the average grain sizes of ZnO films were 120nm, 300nm, 100nm and 60nm on Qz glass, FTO glass, sapphire and silicon substrates, respectively.

The cross section SEM images of as-deposited ZnO films were shown in Fig. 3.3 (1-b) to (4-b).

The thickness of all the films was about 500nm. It was obviously that the crystallinity of the as-deposited ZnO films was gradually improved in the order of Qz glass, FTO glass, sapphire and silicon. On silicon substrate, the ZnO film showed very clear column-like structure which indicated good c-axis ZnO crystallinity.

As we know, the c-axis crystallite size and average grain size can roughly demonstrate the growth speed of ZnO films in the vertical and horizontal directions. For

the same thickness ZnO films, it must have a smaller average grain size if ZnO film had higher c-axis crystallite size resulting in a higher c/a ratio. The grain shape of as-deposited ZnO film could be characterized by the ratio of c-axis crystallite size and average grain size, as shown in Fig. 3.4. With the higher c/a ratio, the as-deposited film would show more clearly column-like structure. It was found that the c/a ratio of ZnO film on Qz glass, sapphire and silicon increased in the same sequence as that of crystallinity.

The results revealed that ZnO film on silicon substrate showed higher c/a ratio with much clear column-like c-axis structures. But ZnO film on FTO glass exhibited the lowest c/a ratio because the average grain size of ZnO film on FTO glass was much higher than those of other substrates. This was because the FTO glass was conductive and polycrystalline substrate. During the deposition on FTO glass substrate, the sputtered ZnO species can move a relatively further distance and the adhesion between the ZnO species and the ZnO films were weaker, resulting in higher growth speed in the horizontal direction than that on the vertical direction [14]. Therefore, the ZnO film on FTO glass exhibited large grain size.

Figure 3.5 showed the AFM images of as-deposited ZnO films on Qz glass, FTO glass and silicon obtained from RF magnetron sputtering (ZnO film on sapphire in our experiment is not suitable for the AFM measurement).

The average roughness (rms) of the ZnO surfaces was calculated for a $4\mu m^2$ scanning area. The results showed that the rms of ZnO films increased from 6.11nm to 6.40nm, 14.5nm in the order of Qz glass, FTO glass and silicon. It can be easily found that ZnO film on silicon substrate showed much clear vertical column-like structures comparing to the other two kinds of substrates, which was well-agreement with the previous results

of XRD and SEM analysis. Additionally, the column-like structures will enlarge the surface area of ZnO film which might be helpful on supplying ZnO nuclei during synthesis of ZnO nanostructures in the reducing annealing process.

There were several potential effects which would affect structural properties of ZnO films deposited on different substrates by RF sputtering.

Firstly, the mismatch of the lattice imperfections had significant influence on ZnO film deposition. ZnO film with good crystallinity could be fabricated on crystalline substrates instead of amorphous or polycrystalline substrates. In our research, four different kinds of substrates were used, two of them were crystalline substrates, silicon and sapphire; the other two were amorphous or polycrystalline, Qz glass and FTO glass. The less mismatching between ZnO and substrate, the better crystallinity ZnO film could be obtained. The theoretical calculation indicated that the mismatch of ZnO to Si(100) and sapphire(0001) is respectively 10.2% and 18.4% [34-35], which were lower theoretical mismatch, comparing to the Qz and FTO glass. This theoretical calculation was good support to the previous results in Fig. 3.2, i.e.: ZnO film on silicon substrate showed the lowest lattice distortion and best crystallinity.

Secondly, the thermal expansion coefficients of substrates are also very important parameters for the RF-sputtering process. The thermal expansion coefficient of ZnO is 3.0×10^{-6}/K as well as the thermal expansion coefficients of the Qz glass, FTO glass, sapphire and silicon are 0.5×10^{-6}/K, 4.5×10^{-6}/K, 6.7×10^{-6}/K and 2.6×10^{-6}/K, respectively. So the silicon substrate showed the lowest difference of thermal expansion coefficient with ZnO, only 13.3%, which meant less lattice imperfection and lattice mismatch would appear during the ZnO film deposition process. This might be partial reason why ZnO film on silicon substrate showed the best crystallinity.

The XRD patterns of obtained ZnO nanostructures on different substrates were shown in Fig. 3.6.

It could be found that (002) peaks were the main peak, which indicated that all of the ZnO nanostructures had highly (002) preferred orientations. Comparing to those obtained from as-deposited films, the intensity of the (002) peaks were significantly increased as well as the FWHM values were decreased. The improvement of crystallinity was attributed to the thermal annealing and nanostructures fabrication.

3.2.2.2 The influence of substrates on the fabrication of ZnO nanostructures

After thermal reducing annealing processes, vertical aligned ZnO nanostructures were obtained on all of the substrates, as shown in Fig. 3.7.

Table 3.1 The parameters of obtained ZnO nanostructures

Substrates / Parameters	Qz glass	FTO glass	Sapphire	Silicon
Head Diameter (nm)	140	250	140	120
Bottom Diameter (nm)	100	120	120	100
Height (nm)	950	900	1000	1250
Density $(10um)^{-2}$	30	70	110	200

The SEM figures indicated that ZnO nanostructures were significantly influenced by the as-deposited films. It was obviously observed that the uniformity of ZnO nanostructures was gradually improved in the same order of the crystallinity increase of as-deposited films. The parameters of obtained ZnO nanostructures were shown in Table 3.1. The results showed that the density of ZnO nanostructures increased in the

same order as the improvement of as-deposited film crystallinity. ZnO nanostructures deposited on the silicon substrate showed the highest density and uniformity.

The results indicated that vertical well- aligned ZnO films were easily formed on the ZnO film with high crystallinity and less lattice distortion, such as ZnO films on silicon substrate.

3.2.2.3 The growth mechanism of ZnO nanostructures

In this research, the as-deposited ZnO film was obtained by RF-sputtering method in pure Ar gas with a power 180W. During the sputtering process, Ar acts as a sputtering enhancing gas. The ZnO species would pile up on the surface of substrate to form ZnO films.

As shown in Fig. 3.8 [6], the intrinsic zinc oxide defect levels indicated that ZnO band gap is 3.2eV, which should be an insulator at room temperature. However, due to the existence of intrinsic defects, the periodic field of ZnO structure was destroyed, creating some additional levels. The existence of these additional levels was conducive to the formation of interstitial zinc atoms.

$$ZnO \rightarrow Zn_i^x + 1/2O_2 \qquad 3\text{-}1$$

From the energy level diagram of ZnO Eigen defect, it's obviously to notice that the activation energy of interstitial zinc atoms (Znix) was quite low (0.05ev). So they had substantially ionized at room temperature.

$$Znix \rightarrow Zni^* + e' \qquad 3\text{-}2$$

This is the reason why ZnO films were conductive (10^3~10^9 ohm/□) at room temperature. In the absence of foreign impurities, these conduction electrons mostly came from the ionization of interstitial zinc atoms, resulting in ZnO films exhibiting the n-type electronic conductivity characteristics.

After ZnO film deposition, the as-deposited films were annealed in the reducing ambient to obtain ZnO nanostructures. The formation of the fluted hexagonal cone nanostructures might be attributed to a two-step growing process determined by the melting point of Zn (419.58 ℃) during annealing in the reducing ambient.

Firstly, in the annealing furnace, ZnO film will react with H_2 to form metal Zn atoms and H_2O which was called reducing process, as shown in Equation 3-3,. When the period temperature increased from room temperature to 420 ℃, obtained Zn atoms would stay still.

$$H_2 + ZnO \rightarrow Zn + H_2O \qquad 3\text{-}3$$

The second step (>420 ℃) was driven by the so-call "self-catalyst effect". The metal Zn atoms from the first step together with the original Zn atoms from the as-deposited ZnO films were used as catalyst in the fabrication of ZnO nanorods. These Zn atoms can move freely on the surface of ZnO films. The bonding of H_2O was undermined and easy to be polarized with the temperature increase, as shown in Equation 3-4.

$$H_2O \rightarrow H^+ OH^- \qquad 3\text{-}4$$

When the temperature was above 420 ℃, the thermal motion of molecules increased, H_2O have more chance to meet the metal Zn atoms on the surface of ZnO films,

As shown in Equation 3-2, metal Zn atoms were easily substantially ionized due to the low activation energy (0.05ev). When these free state Zn* atoms meet the OH^-, they will react as shown in Equation 3-5 and 3-6, which was called growth process.

$$Zn^* + OH^- \rightarrow Zn(OH)_2 \qquad 3\text{-}5$$

$$Zn(OH)_2 \rightarrow ZnO + H_2O \qquad 3\text{-}6$$

As a result, mass ZnO nuclei appeared on the surface of ZnO films. ZnO nuclei would grow up along the (0001) direction (c-axis) because it was the fastest growth

direction of the wurtzite ZnO owing to the polarity of ZnO, as shown in Fig. 3.9.

For ZnO, (0001) has the lowest surface free energy, resulting in a smooth surface in the equilibrium state. This is why the ZnO nanorods showing a strong (0001) preferred orientation to form hexagonal structure. As we discussed in the chapter 1, the oppositely charged ions in ZnO±(0001) produce positively charged Zn^{-}(0001) and negatively charged O^{-}(000-1) surfaces, resulting in a normal dipole moment and spontaneous polarization along the (0001) direction (c-axis).

Therefore, ZnO nuclei in ZnO films were recystallized to form the vertical hexagonal ZnO nanorods due to hexagonal structured heads stretched out to maintain the minimum surface.

The microstructure of ZnO nanorod was confirmed by the TEM measurement in Fig. 3.10. It can be seen that the high-resolution image indicated the nanorod was highly c-axis orientation. The constant c was 0.52nm, (ZnO standard constant 0.52062nm). The selected area electron diffraction (SAED) pattern of this nanorod was shown in Fig. 3.10(c). The perfect regular spots revealed the high crystallinity of this ZnO nanorod.

The reason why different alignment of nanorods appeared even under the same annealing conditions could only be attributed to the effect of ZnO thin film. ZnO nanorods were grown up from as-deposited ZnO films along c-axis on (0001) plane, making the base plane (0001) quite important, which would make great influence on the alignment of ZnO nanorods, as shown in Fig. 8. If as-deposited ZnO film exhibited the similar surface morphology of Fig. 8-a, the roughness was low as well as the crystallinity was good, resulting in the good alignment of ZnO nanorods. Oppositely, if the roughness was quite high as well as the crystallinity was quite poor, the alignment of ZnO nanorods would be very bad. ZnO films on silicon substrates exhibited best

crystallinity, lowest lattice distortion and lowest roughness. Therefore, the vertical well-aligned ZnO nanorods were obtained on the silicon substrates.

3.2.3 Summary

The influence of different substrates on the as-deposited ZnO films and following formed ZnO nanostructures were investigated. The results showed that the substrates had significant influence of ZnO films, further influence on fabrication of well-aligned ZnO nanostructures. ZnO film deposited on the silicon had the best crystallinity and the formed ZnO nanostructures with the best alignment and the highest density.

For the mechanism, the lower mismatch of the lattice imperfections and matching thermal expansion coefficient between ZnO film and substrates contributed to fabricating ZnO film with good crystallinity and vertical well-aligned ZnO nanostructures. The information for ZnO nanostructures fabricating on different substrates will give helpful information for fabrication of vertical well-aligned ZnO nanostructures.

3.3 Annealing temperature dependence

3.3.1 Experiments

ZnO thin films (500nm) were deposited on silicon substrate by a conventional 13.56 MHz radio frequency (RF) magnetron sputtering system. The RF power is 180 W. The deposition processes were performed in an Ar ambient (30 sccm) controlled by a mass flow controller. The working pressure was maintained at 7 Pa. The substrate temperature on the anode was preheated to 150 °C for 20min prior to deposition and was fixed during the deposition procedure.

Following the deposition procedure, ZnO thin film was put into a conventional furnace at low temperature annealing in a reducing gas ambient. The furnace kept the

temperature at different temperatures (including 460 ℃, 450 ℃, 440 ℃, and 420 ℃) for 5h in reducing gas (1.9% H_2 in N_2). The influences of the annealing temperature on the fabrication of vertical well-aligned ZnO nanostructures were investigated.

3.3.2 Results and discussion

Figure 3.11 showed the XRD patterns of the ZnO nanostructures obtained from different annealing temperatures. The X-ray diffraction analysis revealed that the (002) peak was the dominate peak for all the samples, indicating that all of the obtained ZnO nanostructures showed highly c-axis (002) preferred orientation. However, the crystallinity of formed ZnO nanostructures was gradually improved with the increase of annealing temperature. ZnO film obtained in 460 ℃ showed the highest (002) peak intensity. The different peak intensities of the ZnO nanostructures indicated that the crystallinity of obtained ZnO nanostructures was significantly influenced by the annealing temperatures.

Figure 3.12 (1-a) to (4-a) showed the top view SEM images of vertical well-aligned ZnO nanostructures obtained from reducing annealing process in different temperatures. It was observed that the density of obtained ZnO nanostructures was decreased from $200/(10um)^2$ to $80/(10um)^2$, $50/(10um)^2$, and $30/(10um)^2$, when the annealing temperature decreased from 460 ℃ to 450 ℃, 440 ℃, and 420 ℃, respectively.

The cross section SEM images of obtained vertical well-aligned ZnO nanostructures obtained from reducing annealing process in different temperatures were shown in Fig. 3.9 (1-b) to (4-b). The results indicated that the height of obtained ZnO nanostructures was decreased from 1250nm to 600nm, 300nm, and 100nm, when the annealing temperature decreased from 460 ℃ to 450 ℃, 440 ℃, and 420 ℃, respectively.

However, the diameter of obtained ZnO nanostructures was firstly increased from

120nm to 150nm, 180nm, then decreased to 130nm, when the annealing temperature decreased from 460 ℃ to 450 ℃, 440 ℃, and 420 ℃, respectively. With the increase of annealing temperatures, the height of ZnO nanostructure increased due to the increase of the growth speed in the vertical direction. But the diameter of ZnO nanostructures was firstly increased from 130nm to 180nm, then decreased from 180nm to 150nm, 120nm when the annealing temperatures increased from 420 ℃ to 440 ℃, 450 ℃, and 460 ℃.

For the mechanism, the ZnO nanostructures were recrystallizing and reducing processes in the same time in our experiments. But the diameter and height of ZnO nanostructures was increase due to the speed of recrystallizing process was faster than reducing process in the temperature increased from 420 ℃ to 440 ℃, 450 ℃, 460 ℃. When the temperature was up to 460 ℃, The speed of reducing process was faster than recrystallizing process, resulting in the reducing of ZnO nanorods, leading to the size decrease of ZnO nanostructures.

Figure 3.13 showed the PL spectra of the ZnO nanostructures obtained from different annealing temperatures.

It was found that the blue-green emission centered on 491nm was obtained from the all of annealed samples with the suppressed UV emission around 378nm. The most intense green peak was obtained from the ZnO nanostructures grown in 460 ℃.

It is well-accepted that the green emission from ZnO nanostructures arises from oxygen vacancy related defect centers in the ZnO. It can assume that the much more oxygen vacancies might be produced and existed on the ZnO nanostructures which have much larger appearance area, result in the enhancement of PL peak in the visible range.

Comparing the ZnO nanostructures formed in the different annealing temperatures, it was obviously that there were much dense ZnO nanostructures grown in 460℃. Comparing to ZnO nanostructures in other temperatures including 420℃, 440℃, and 450 ℃, the ZnO nanostructures showed higher density (220/10μm^2) in 460 ℃ so that the PL emission in visible range from ZnO nanostructures in 460 ℃ was much stronger than ZnO nanostructures in other temperatures (420℃, 440℃, and 450 ℃).

3.3.3 Summary

The influence of different annealing temperatures on the formed ZnO nanostructures was investigated. The density and height of ZnO nanostructures were increased with the increase of the annealing temperature. The diameter of ZnO nanostructures were increased with the temperature increase from 420 ℃ to 440 ℃, 450 ℃, then slightly decreased when the temperature was up to 460 ℃. The blue-green emission centered at 491nm was obtained from all of annealed samples, with the suppressed UV emission around 378nm. The intensity of visible peak (around 491nm) was increased with the increase of temperature. The annealing temperatures can help controlling the size, density and PL properties of the ZnO nanostructures.

3.4 Conclusions

In this chapter, the influence of the substrates and annealing temperatures were investigated.

1) The results showed that the substrates had significant influence of ZnO films, further influence on fabrication of well-aligned ZnO nanostructures. ZnO film deposited on the silicon had the best crystallinity and the formed ZnO nanostructures with the best alignment and the highest density.

2) The lower mismatch of the lattice imperfections and matching thermal expansion coefficient between ZnO film and substrates contributed to fabricating ZnO film with good crystallinity and vertical well-aligned ZnO nanostructures.

3) The density and height of ZnO nanostructures were increased with the increase of the annealing temperature. The average diameter of ZnO nanostructures were increased with the temperature increase from 420 ℃ to 440 ℃, 450 ℃, then slightly decreased when the temperature was up to 460 ℃. The blue-green emission centered at 491nm was obtained from all of annealed samples with the suppressed UV emission center around 378nm. The intensity of visible peak (center around 491nm) was increased with the increase of temperature. The annealing temperatures can help controlling the size, density and PL properties of the ZnO nanostructures.

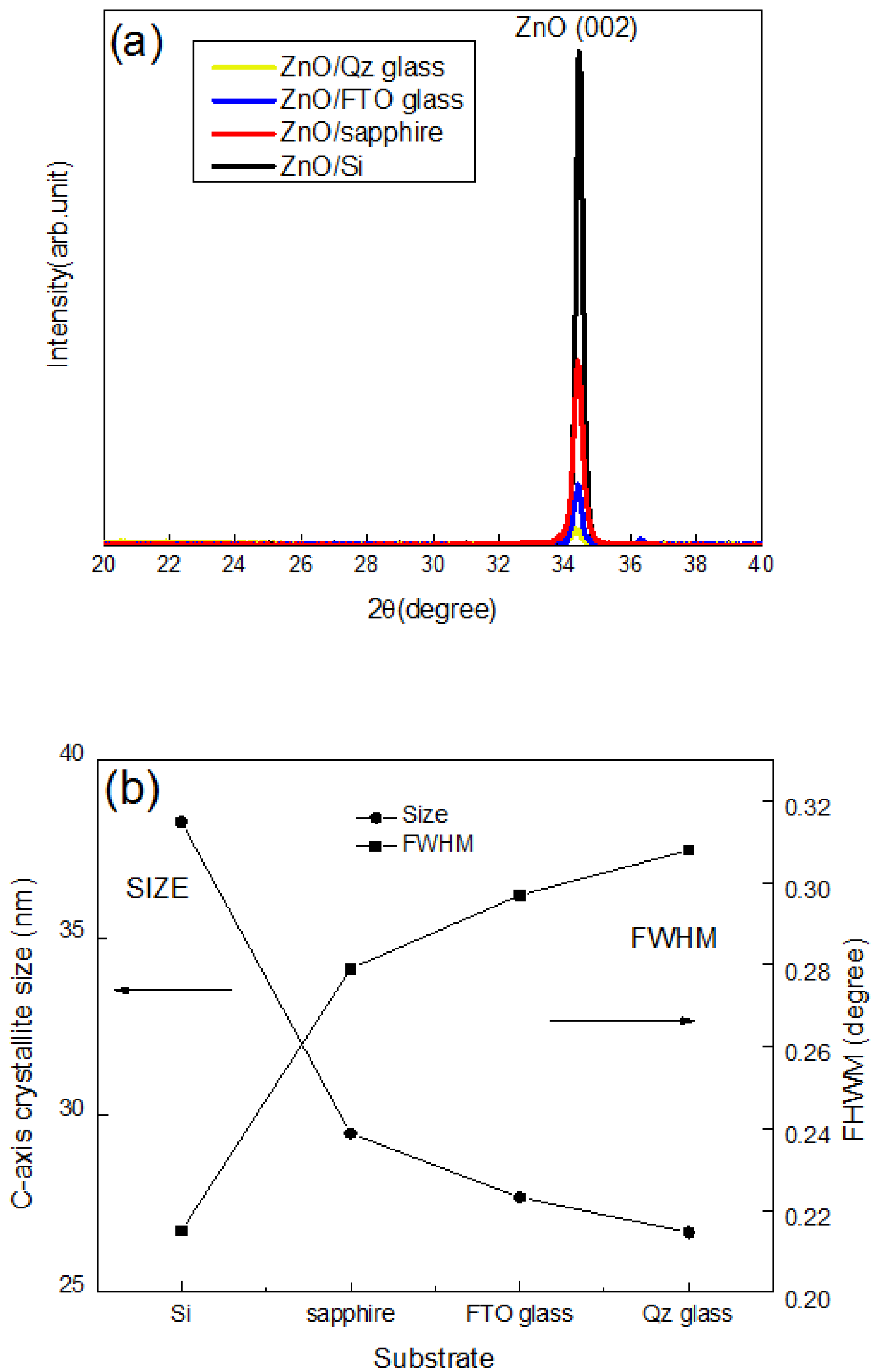

Fig. 3.1 (a) XRD patterns and (b) dependence of c-axis crystallite sizes and FWHM of as-deposited ZnO films on different substrates.

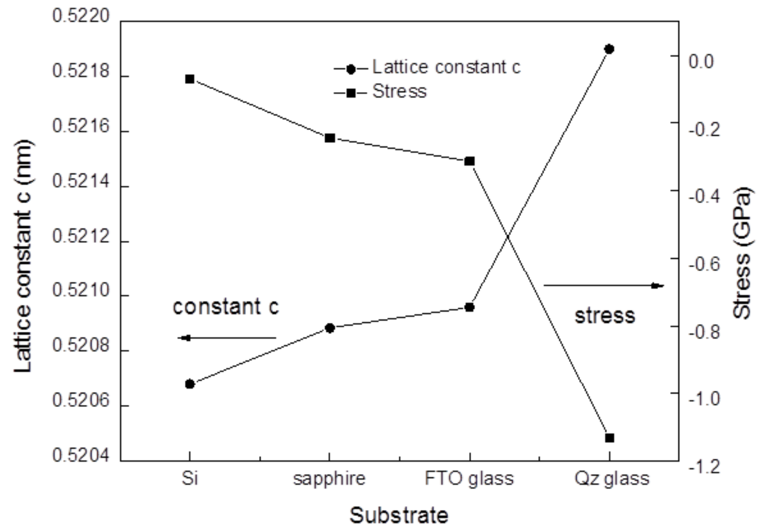

Fig. 3.2 Dependence of lattice constant c and stress of as-deposited ZnO films on different substrates.

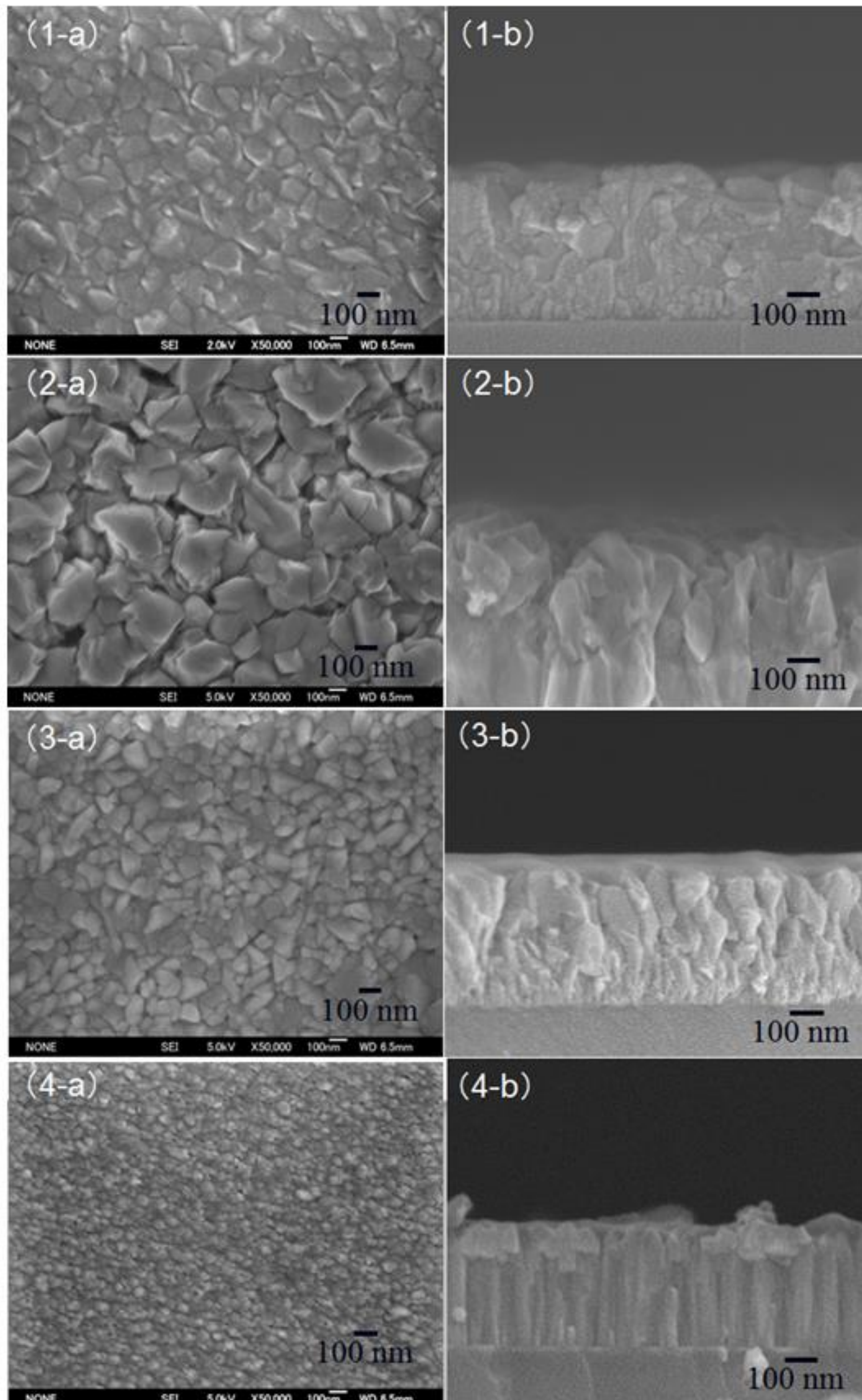

Fig. 3.3 SEM images of as-deposited ZnO film on (1) Qz glass, (2) FTO glass, (3) sapphire, and (4) silicon.

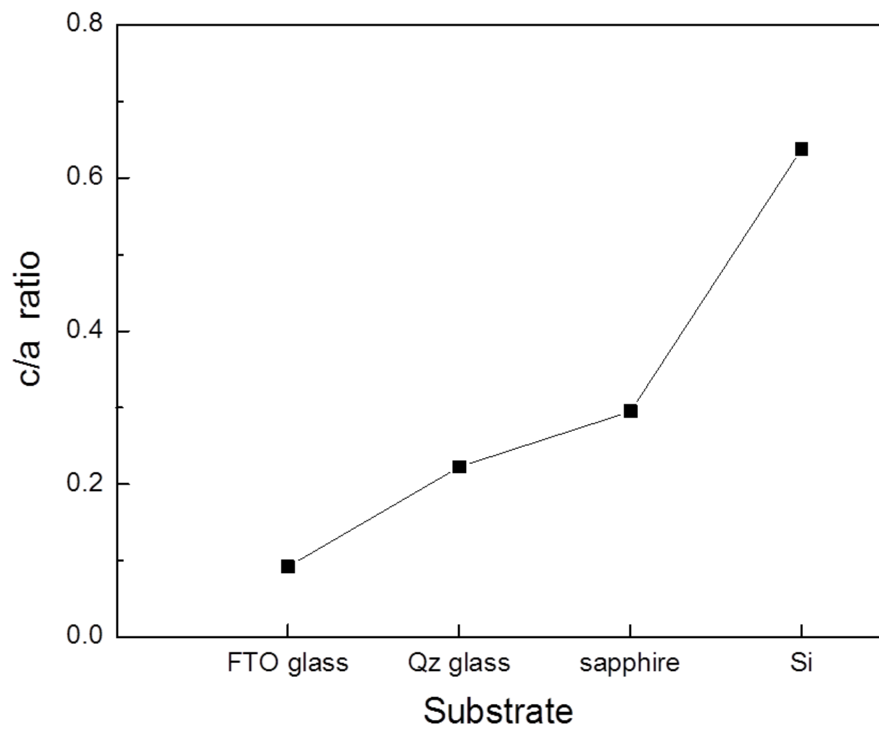

Fig. 3.4 Comparison of ca ratio of as-deposited ZnO films on different substrates.

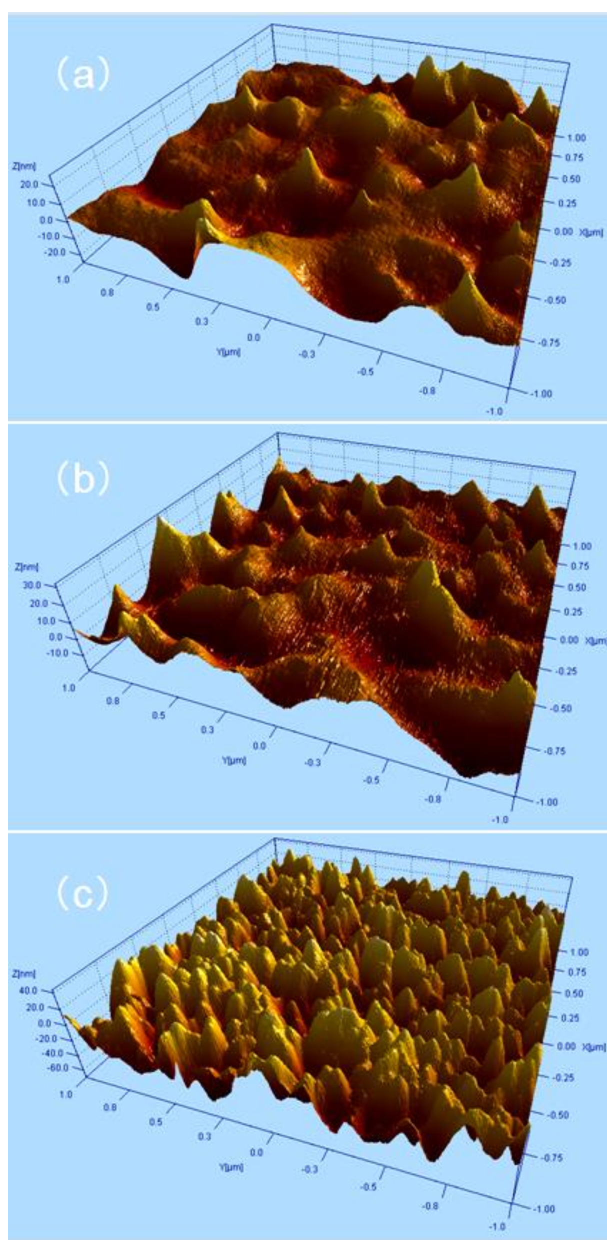

Fig. 3.5 AFM images of ZnO films (500 nm in thickness) deposited on (a) Qz glass, (b) FTO glass, and (c) silicon.

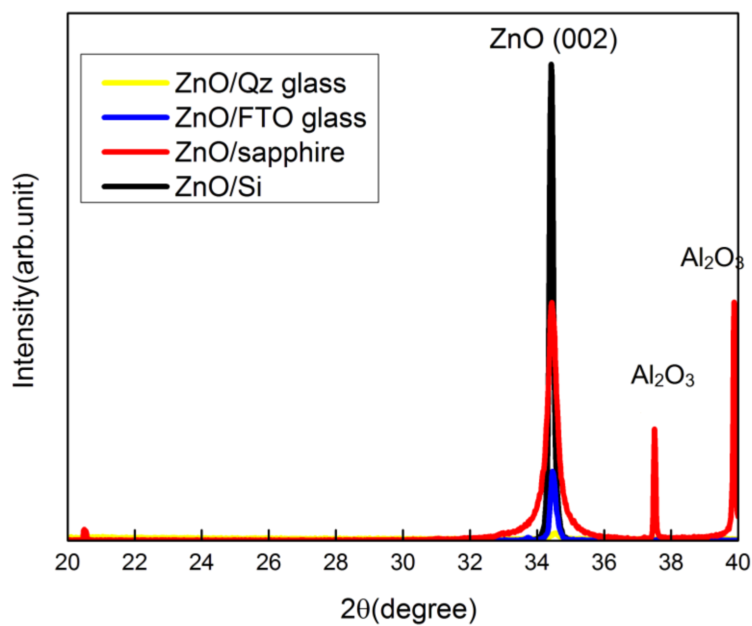

Fig. 3.6 XRD patterns of ZnO nanostructures on different substrates (after reducing annealing, two peaks of Al_2O_3 appeared in XRD pattern of ZnO sapphire).

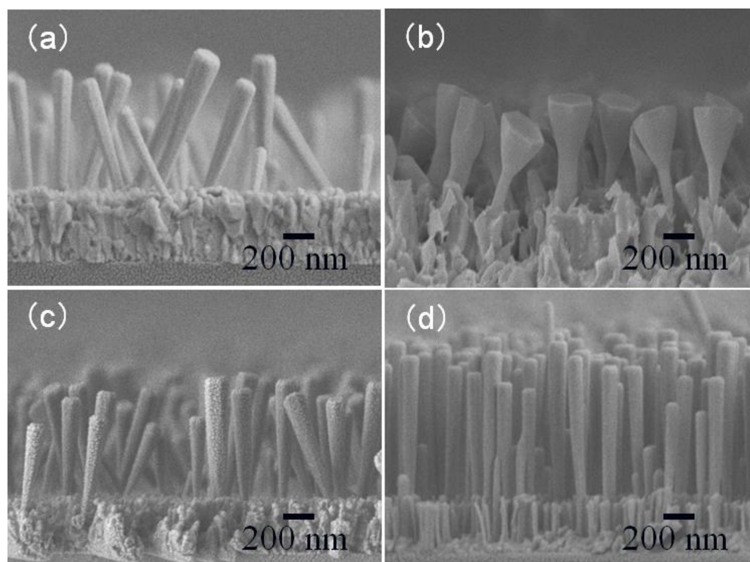

Fig. 3.7 SEM images of fabricated ZnO nanostructures on (a) Qz glass, (b) FTO glass, (c) sapphire, and (d) silicon.

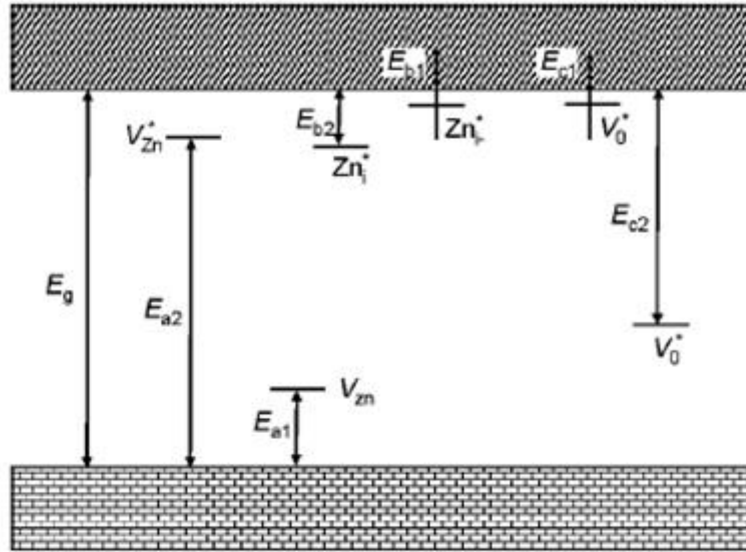

Fig. 3.8 The energy level diagram of ZnO Eigen defect. [6]

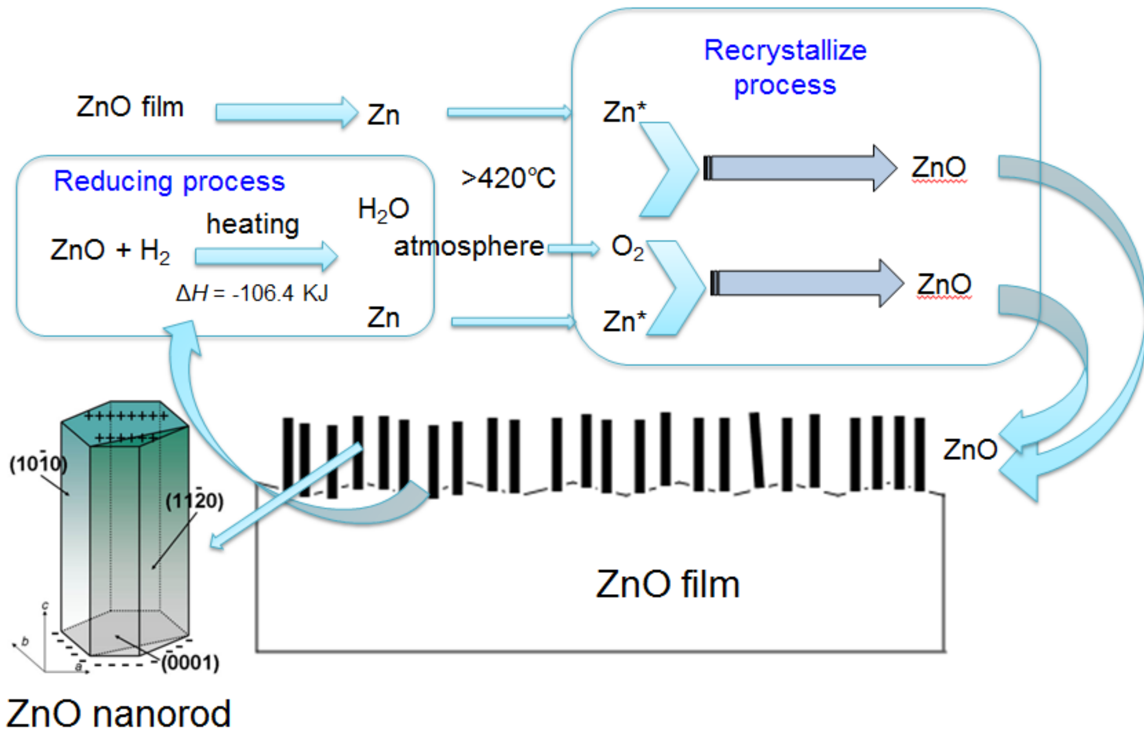

Fig. 3.9 The growth mechanism of ZnO nanostructures.

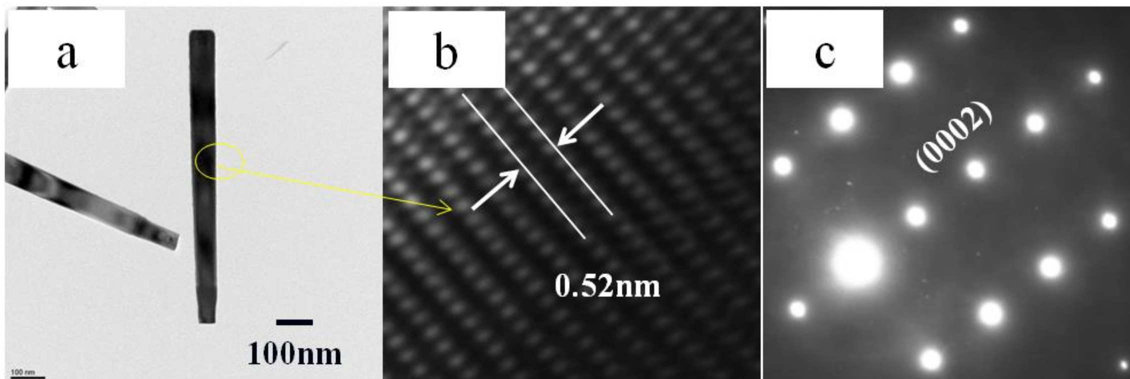

Fig. 3.10 The TEM images of a ZnO nanorod

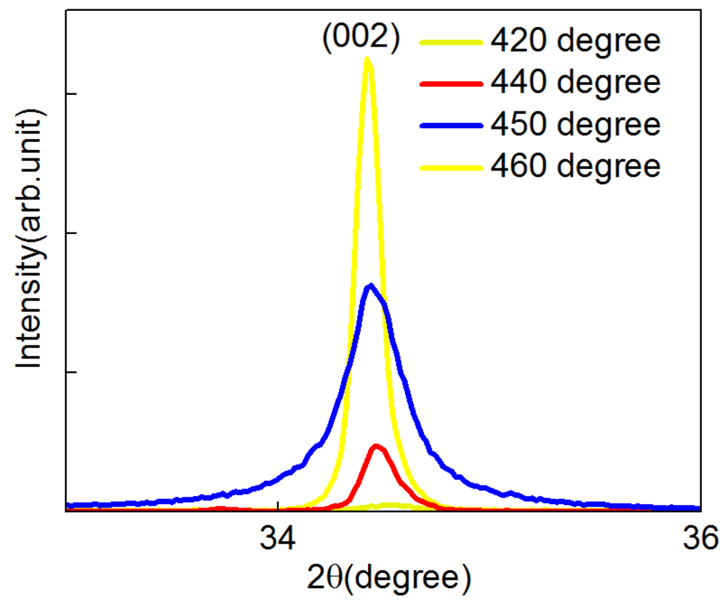

Fig. 3.11 XRD patterns of ZnO nanostructures obtained from different annealing temperatures.

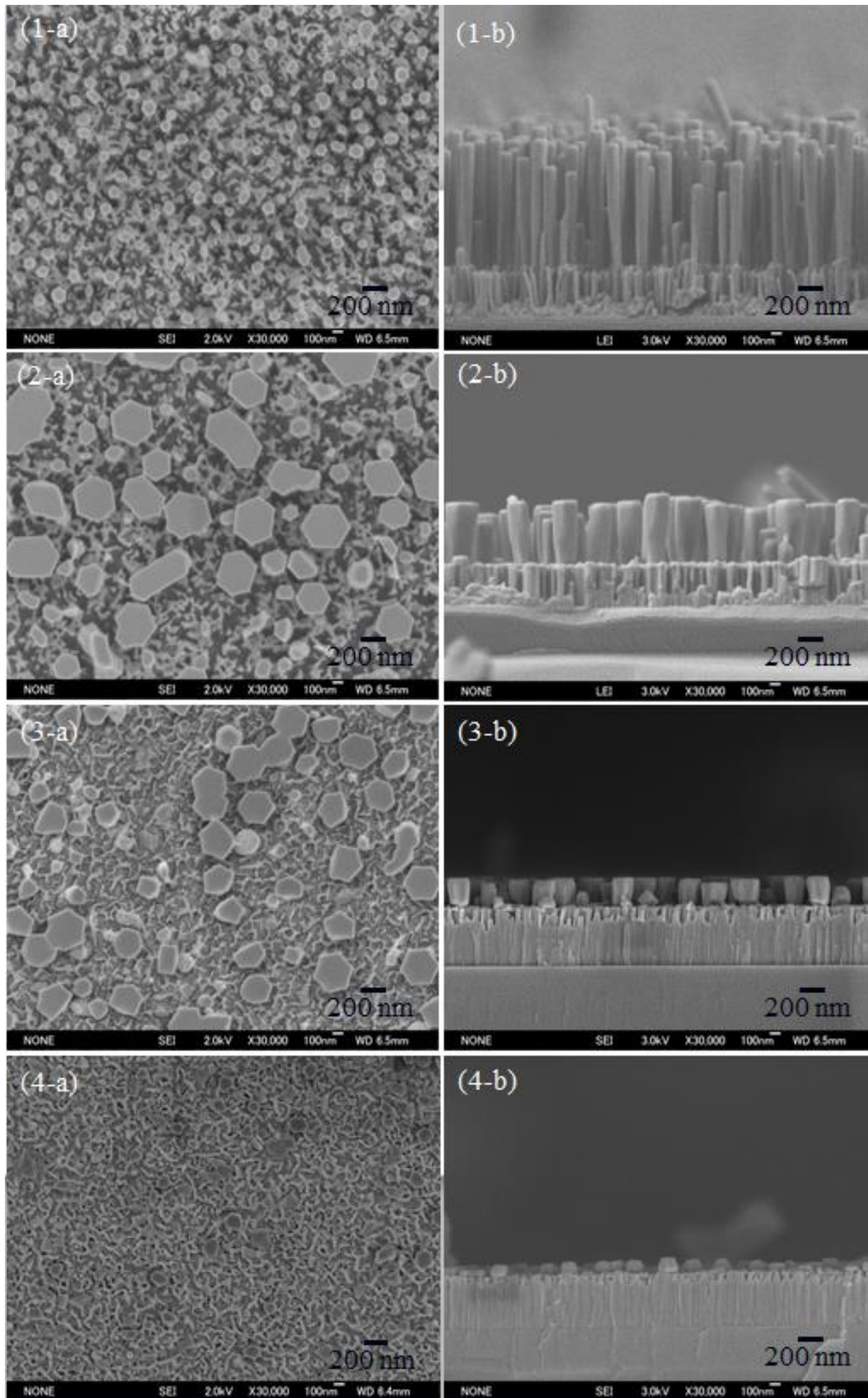

Fig. 3.12 SEM images of fabricated ZnO nanostructures with the annealing temperature

of (1) 460 ℃ (2) 450 ℃, (3) 440 ℃, and (4) 420 ℃.

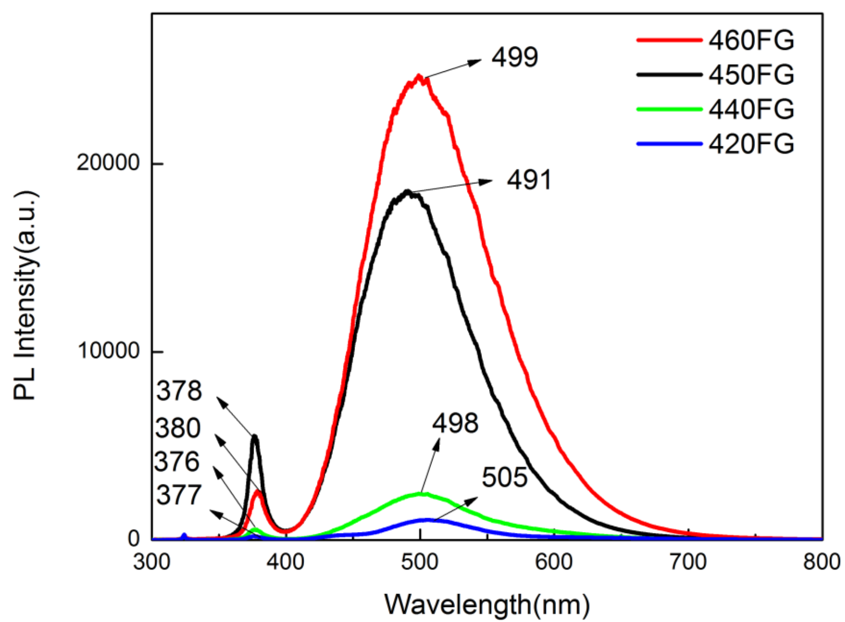

Fig. 3.13 PL spectra of ZnO nanostructures obtained from different annealing temperatures.

Reference

1 D. C. Look, Mater. Sci. Eng. B. Solid-State Mater. Adv. Technol. 80 (2001) 383.

2 Q. H. Li, Q. Wan, Y. X. Liang, and T. H. Wang, Appl. Phys. Lett. 84 (2004) 4556.

3. S. Choi, J. W. Kang, D. K. Hwang, and S. J. Park, IEEE Trans. on Electron Devices. 57 (2010) 26.

4. B. F. Martinson, J. W. Elam, J. T. Hupp, and M. J. Pellin, Nano Lett. 7 (2007) 1887.

5. L. Li, T. Y. Zhai, Y. Bando, and D. Golberg, Nano Ener. 1 (2012) 91.

6. T. Aoki, Y. Hatanaka, and D. C. Look, Appl. Phys. Lett. 76 (2000) 3257.

7 H. Chik, J. Liang, S. Cloutier, N. Kouklin, and J. Xu, Appl. Phys. Lett. 84 (2004) 376.

8 U. Ozgur, Y. I. Alivov, C. Liu, A. Teke, M. A. Reshchikov, S. Dogan, V. Avrutin, S. J. Cho, and H. Morkoc, J. Appl. Phys. 98 (2005) 041301.

9. T. Ma, M. Guo, M. Zhang, and X. D. Wang, Nanotechnol. 18 (2007) 035605.

10 S. Y. Li, P. Lin, C. Y. Lee, and T. Y. Tseng, J. Appl. Phys. 95 (2004) 3711.

11 H. Ohta, K. Kawamura, M. Orita, M. Hirano, N. Sarukura, and H. Hosono, Appl. Phys. Lett. 77 (2000) 475.

12 M. H. Huang, S. Mao, H. Feick, H. Yan, Y. Wu, H. Kind, E. Weber, R. Russo, and P. Yang, Science. 292 (2001) 1897.

13. C. Y. Li, M. Furuta, T. Matsuda, T. Hiramatsu, H. Furuta, and T. Hirao, Thin Solid Films. 517 (2009) 3265.

14. T. Hiramatsu, M. Furuta, H. Furuta, T. Matsuda, C. Y. Li, and T. Hirao, J. Cryst. Growth. 282 (2009).

15. T. Matsuda, M. Furuta, T. Hiramatsu, H. Furuta, C. Y. Li, and T. Hirao, Appl. Surf. Sci. 256 (2010) 6350

16. M. Furuta, T. Hiramatsu, T. Matsuda, C. Y. Li, H. Furuta, and T. Hirao, J. Non-cryst. Solids. 354 (2008) 1926
17. C. Y. Li, T. Kawaharamura, T. Matsuda, H. Furuta, T. Hiramatsu, M. Furuta, and T. Hirao, J. Appl. Phys. Express. 2 (2009) 091601
18. C. Y. Li, T. Matsuda, T. Kawaharamura, H. Furuta, M. Furuta, T. Hiramatsu, and T. Hirao, J. Vac. Sci. Technol. B. 28 (2010) C2B51
19. E. V. Monakhov, J. S. Christensen, K. Manknys, B. G. Svensson, and A. Y. Kuznetsov, Appl. Phys. Lett. 87 (2005) 191910
20. T. Minami, H. Nanto, and S. Takata, Appl. Phys. Lett. 41 (1982) 958
21. R. E. I. Schropp, and A. Madan, J. Appl. Phys. 66 (1989) 2027
22. J. Lee, W. Gao, Z. Li, M. Hodgson, J. Metson, H. Gong, and U. Pal, J. Appl. Phys. A80 (2005) 1641.
23. K. Ip, M. E. Overberg, Y. W. Heo, D. P. Norton, S. J. Peaton, C. E. Stutz, B. Luo, F. Ren, D. C. Look, and J. M. Zavada, Appl. Phys. Lett. 82 (2003) 385.
24. K. Shin, K. Prabakar, W. P. Tai, J. H. OH, and C. Lee, J. Korean Phys. Soc. 45 (2004) 1288.
25. N. H. Kim, and H. W. Kim, Mater. Lett. 58 (2003) 938.
26. S. K. Hong, T. Hanada, H. Ko, Y. Chen, T. Yao, D. Imai, K. Arak, M. Shinohara, K. Saitoh, and M. Terauchi, Phys. Rev. B. 65 (2002) 115331.
27. M. Y. Han, and J. H. Jou, Thin Solid Films. 260 (1995) 58.
28. C. Y. Li, M. Furuta, T. Matsuda, T. Hiramatsu, H. Furuta, and T. Hirao, Thin Solid Films, 517 (2009) 3265.

29. M. B. Lee, M. Kawasaki, M. Yoshimoto, B. K. Moon, H. Ishiwara, and H.Koinuma, Jpn. J. Appl. Phys. 34 (1995) 808.
30. F. Shinoki and A. Itoh, J. Appl. Phys. 46 (1975) 3381.
31. D. P. Wang, Z. M. Li, T. Kawaharamura, M. Furuta, T. Narusawa, and C. Y. Li, Phys. stat. Sol. (c). 9 (2012) 491.
32. M. Birkholz, Thin Film Analysis by X-Ray Scattering, Wiley-VCH Verlag GmbH&Co. KGaA, (2006).
33. X. Li, C. Y. Li, T. Kawaharamura, D. P. Wang, N. Nitta, M. Furuta, H. Furuta and A. Hatta, Trans. Mat. Res. Soc., 28, (2013).
34. L. Duan, B. X. Lin, R. Yao, and Z. X. Fu, Chinese J. Mater. Research, 20 (2006) 259.
35. M. Liu, Z. W. Liu, J. F. Gu, F. W. Qin, C. Y. Ma, and Q. Y. Zhang, Acta. Phys. Sin. 57 (2008) 1113.

Chapter 4

Fabrication of large size ZnO nanostructures by multiple annealing processes

4.1 Introduction

In the last chapter, vertical well-aligned ZnO nanostructures with good reproducibility were fabricated. But, the size of ZnO nanostructures was too small.

In order to further control and produce large surface area ZnO nanostructures, we developed a novel multiple annealing process, which combines the reducing annealing process and oxygen annealing process.

As we discussed in last chapter, both recrystallizing and reducing processes happened together in the annealing process. The reducing process can be continuously carried out due to the continuous supplement of the forming gas (1.9%H_2 in N_2). But the recrystallizing process would be decreased due to the limited oxygen in the furnace. If the oxygen was too few, the reducing process will suppress the recrystallizing process, leading to the etching of the ZnO nanostructures. If suitable oxygen was periodically supplied between the reducing annealing processes, the oxygen can be supplied to contribute ZnO nanostructures regrowth,. This mechanism we will discuss in details in this chapter.

With the periodic oxygen supplementation, the multiple annealing can supply suitable oxygen during the reducing annealing processes. The properties of obtained ZnO nanostructures were strongly dependent on the (1) oxygen treatment time, (2) low

temperature treatment, and (3) multiple annealing procedures.

In this chapter, the effects of multiple annealing processes on the properties of ZnO nanostructures were investigated.

Firstly, the periodic oxygen supplementation has great influence on the fabrication of large size ZnO nanostructures. Adjusting of oxygen treatment time was the easiest way to control the supply of oxygen during the multiple annealing processes. In this part, I discussed the influence of oxygen annealing time on the fabrication of ZnO nanostructures and try to optimize the periodic oxygen supplementation to supply suitable oxygen during the reducing annealing processes.

Then, the influence of low temperature treatment on the properties of ZnO nanostructures was discussed. In this thesis, the low temperature treatment was firstly developed to assistant obtaining high density vertical well-aligned ZnO nanostructures in our novel multiple annealing processes. A relatively low temperature (<419.6 ℃, the melting point of Zn) reducing annealing can reduce the ZnO film surface to fabricate more Zn on the surface. When the annealing temperature was over 419.6 ℃, the Zn atoms on the surface can move unrestrainedly on the ZnO film surface to reacting with oxygen, fabricating ZnO nuclei.

In this part, I discussed about the influence of low temperature on the fabrication of ZnO nanostructures and try to optimize the pre-annealing temperature to help fabricating much more ZnO nanostructures during the multiple annealing processes.

Finally, the influence of multiple annealing process design (the arrangement of reducing and oxygen treatment order and time) on the properties of obtained ZnO nanostructures was discussed. The multiple annealing process design has great influence on the fabrication of large size ZnO nanostructures. Multiple annealing processes also

can help controlling the supply of oxygen during the multiple annealing processes. Further, the proper annealing process design can adjust the size and morphology of the obtained ZnO nanostructures.

In this part, I discussed about the influence of multiple annealing processes on the fabrication of ZnO nanostructures and try to fabricate ZnO nanostructures with controllable size.

4.2 Influence of oxygen annealing time

4.2.1 Experiments

ZnO thin films (500nm) were deposited on FTO glass by a conventional 13.56 MHz radio frequency (RF) magnetron sputtering system [11-12]. A 4-inch ZnO ceramic target (99.999% ZnO) was located on the cathode 60mm away from the substrate stage. The RF power was 180 W. The deposition processes were performed in an Ar ambient (30 sccm) controlled by a mass flow controller. The working pressure was maintained at 7 Pa. The substrate temperature on the anode was preheated to 150 ℃ for 20min prior to deposition and was fixed during the deposition procedure.

Following the deposition procedure, ZnO thin film was put into a conventional furnace in a reducing gas ambient. Firstly a low temperature treatment was introduced to treat the ZnO film at 300 ℃ for 3h in reducing ambient. Then the ZnO films were treated by the multiple annealing processes at 450 ℃. Firstly the ZnO film was annealed in the reducing gas ambient for 2h, and then annealed in O_2 for different time, including 0min, 15min, 30min, 1h, followed by a reducing annealing in the same condition as the first step with extending the annealing time to 3h. For safety, N_2 was introduced shortly to the furnace between every two steps. The annealing parameters were shown in Fig. 4.1.

4.2.2 Results and discussion

Figure 4.2 showed the SEM images of as-deposited ZnO films and obtained ZnO nanostructures after multiple annealing processes with different oxygen treatment time.

Fig. 4.2(a) was the as-deposited ZnO film, with an average grain size 320nm. Fig. 4.2(b,c,d,e) was the SEM images of ZnO nanostructures obtained from the multiple annealing processes with different oxygen annealing treatment time (0, 15min, 30min, and 1h). The results in Fig. 4.2(b,c,d,e) indicated that the size of ZnO nanostructures increased with extending the oxygen annealing time from 0min to 1h.

When the oxygen annealing time was increased from 0min to 15min, 30min and 1h, the density and diameter of ZnO nanostructures were increased from $160/(10\mu m)^2$ to $240/(10\mu m)^2$, $270/(10\mu m)^2$, $450/(10\mu m)^2$ and 110nm to 130nm, 150nm, 220nm, respectively. These results showed that the high density large size ZnO nanostructures were fabricated after the optimized multiple annealing process. The highest density and diameter was obtained from ZnO nanostructures after multiple annealing processes with 1h oxygen treatment.

The XRD patterns of obtained ZnO nanostructures from multiple annealing processes with different oxygen annealing time were shown in Fig. 4.3. It's found that (002) peaks were the dominate peak, which indicated that all of the ZnO nanostructures had highly (002) preferred orientation.

The peak intensities of ZnO nanostructures were significantly increased with the oxygen annealing treatment extending from 0min to 15min, 30min, and 1h. The change of peak intensities of the ZnO nanostructures indicated that the crystallinity of ZnO nanostructures was significantly improved by the oxygen annealing processes.

Figure 4.4 showed the PL spectra of ZnO nanostructures with different oxygen

treatment time. The visible peak (center around 491nm) intensity increased when the oxygen annealing processes extended from 0min to 1h. Oppositely, the UV peak (center around 378nm) intensity decreased when the oxygen annealing processes extended to 1h. The visible emission was enhanced with the extending time of oxygen treatment time due to the enlarged surface area as we discussed in chapter 3. The intensity decrease of UV peak was due to the improvement of crystallinity to reduce the defects and dislocation.

4.2.3 Summary

The influence of oxygen treatment time on the formed ZnO nanostructures was investigated. The results indicated the oxygen treatment time can help adjusting the size and crystallinity of obtained ZnO nanostructures.

4.3 Influence of low temperature treatment

4.3.1 Experiments

ZnO thin films (500nm) were deposited on FTO glass by a conventional 13.56 MHz radio frequency (RF) magnetron sputtering system. The RF power was 180 W. The deposition processes were performed in an Ar ambient (30 sccm) controlled by a mass flow controller. The working pressure was maintained at 7 Pa. The substrate temperature on the anode was 150 ℃.

Following the deposition procedure, ZnO thin film was put into a conventional furnace at low temperature annealing in a reducing gas ambient. Firstly the low temperature treatment was introduced to treat the ZnO film at 100℃, 200℃, 300℃, 400℃ for 3h in reducing ambient, respectively. Then the ZnO films were treated by the multiple annealing processes at 450℃. In these multiple annealing processes, firstly the ZnO film was annealed in the reducing gas ambient for 3 h, and then annealed in O_2 for

1h followed by a reducing annealing in the same condition as the first step with extending the annealing time to 4h. For safety, N_2 was introduced shortly to the furnace between every two steps.

4.3.2 Results and discussion

Figure 4.5 showed the SEM images of ZnO nanostructures after multiple annealing processes with different low temperature treatment.

Fig. 4.5(a-e) was the SEM images of ZnO nanostructures obtained from the multiple annealing processes with different low temperature pre-annealing temperature 100 ℃, 200 ℃, 400 ℃, and 300 ℃, respectively. The SEM images indicated that the density of ZnO nanostructures was increased with extending the annealing temperature from 100 ℃ to 200 ℃, and 300 ℃. These results confirmed that more ZnO nanostructures could be formed on the surface of ZnO films with increasing the low temperature treatment temperature. However, the density of ZnO nanostructures was decreased when the temperature increased from 300 ℃ to 400 ℃, due to the reducing speed faster than recrystallizing speed, resulting in the reducing of fabricated ZnO nuclei, resulting in the density decrease of the ZnO nanostructures.

When the low temperature treatment in 300 ℃ for 3h was applied, the vertical well-aligned ZnO nanostructures with the highest density were fabricated on the surface of ZnO films. The top diameter of the obtained ZnO nanostructures was 270nm.

4.3.3 Summary

The influence of low temperature treatment on the formed ZnO nanostructures was investigated. The low temperature treatment can help controlling the density of the obtained ZnO nanostructures.

4.4 Fabrication of large size ZnO nanostructures

4.4.1. Experiments

ZnO film (thickness 500nm) was deposited on FTO glasses by RF (13.5MHz) magnetron sputtering method. Following the deposition process, the initial multiple annealing process was applied to fabricate ZnO nanorods on ZnO films at 450℃. Sequentially, several cycles (one reducing annealing process combined with one oxygen treatment called one cycle) were applied to help on ZnO nanorods regrowth to large surface area. Oxygen annealing was introduced to treat ZnO nanorods between two reducing annealing processes for supply oxygen helping on ZnO nanostructures further growth during the reducing annealing processes. The fabrication processes were was shown in Fig. 4.6.

4.4.2. Results and discussion

The XRD patterns of the ZnO nanostructures were shown in Fig. 4.7. The X-ray diffraction analysis revealed that the (002) reflection peak was the dominate peak for all the films, meaning (002) preferred orientation with a c-axis perpendicular to the substrates. However, the peak intensities of ZnO nanostructures were significantly increased with the process extending from 2 step to 3step, 4 step, and 5 step. The change of peak intensities of the ZnO nanostructures indicated that the crystallinity of ZnO nanostructures was significantly influenced by the annealing processes.

Figure 4.8 showed the relationship between the c-axis crystallite size, the FWHM and different annealing processes.

It was found that the FWHM value was decreased from 2 step to 3step, 4 step, and 5 step. The sharpest FWHM value 0.193 °was obtained from the ZnO nanostructures after 5 step. Therefore, the XRD result showed the crystallinity of ZnO nanostructures was

improved gradually when the process extending from 2 step to 3step, 4 step, and 5 step.

Figure 4.9 showed SEM images of ZnO nanostructures fabricated by different annealing processes. The results indicated that the ZnO nanostructures were grown to be big size with extending the annealing processes from 2 step to 3 step, 4 step, and 5 step. The size of the ZnO nanostructures can be adjusted by controlling the annealing processes.

When the annealing processes extended, ZnO nanostructures grew to be large size. When the annealing processes increased from 2 step to 3 step, 4 step, and 5 step, the heights of ZnO nanostructures increased from 1340nm to 1750m, 2130nm, and 2510nm as well as top diameters of ZnO nanostructures increased from 250nm to 270m, 275nm, 290nm, respectively.

When the multi-annealing steps increased from 2 step to 5 step, the thickness of ZnO films was decreased. After 4 step, there were no continuous films on the FTO surface.

In our technique, ZnO nanostructures could be fabricated by catalyst free effect during initial reducing annealing. If suitable oxygen was supplied to the ZnO film, the reduced zinc atoms from films would react with oxygen to contribute ZnO nanostructures regrowth. Therefore, optimized reducing annealing process recrystallized zinc atoms from ZnO film to ZnO nanostructures, resulting in the thin film reducing remarkably. Finally, the large ZnO rods with 2.5 μm in height and 0.3 μm in top-diameter were obtained.

The microstructure of ZnO nanostructures obtained from initial annealing process was reconfirmed by the TEM measurement in Fig. 4.10. It can be seen that the high-resolution image reconfirmed the nanorod was highly c-axis orientation. The

constant c was 0.52nm, (ZnO standard constant 0.52098nm). The selected area electron diffraction (SAED) pattern of this nanorod was shown in Fig. 4.10. The perfect regular spots revealed the high crystallinity of this ZnO nanorod.

Figure 4.11 showed optical transmittance of ZnO nanostructures formed by different processes. When the annealing processes increased from 2 step to 3 step, 4 step, and 5 step, the transmittance of ZnO nanostructures on FTO glass decreased due to the large size ZnO nanostructures helped increasing the scattering and loss of the light, resulting in the decrease of the transmittance.

The PL spectra of ZnO nanostructures formed by different processes were shown in Fig. 4.12. The PL measurement showed that the blue-green emission centered at 491nm was obtained from the all of annealed samples, with the UV emission centered around 378nm. The visible peak intensity increased when the multiple annealing processes extended, which was probably due to the surface area increase of ZnO nanostructures with extending multiple annealing procedures.

4.4.3. Summary

The influence of multiple annealing procedures on the formation of large size ZnO nanostructures was investigated. Large size ZnO nanostructures were obtained with the novel multi-annealing processes. The crystallinity of ZnO nanostructures was also improved. Oxygen annealing between the two reducing gas annealing processes contributed to efficiently introduce the oxygen into the ZnO thin films, leading to the growth of ZnO nanostructures. The large size ZnO nanostructures were fabricated after the multiple annealing procedures.

4.5 Conclusions

In this chapter, the effects of different post-treatment processes on the ZnO

nanostructures were investigated. The conclusions of each part in this chapter will be generally expressed one by one.

1) The oxygen treatment time can help adjusting the size of obtained ZnO nanostructures.

2) The low temperature treatment can help controlling the density of the obtained ZnO nanostructures.

3) Large size ZnO nanostructures were obtained with the novel multi-annealing processes. The crystallinity of ZnO nanostructures was also improved. Oxygen annealing between the two reducing gas annealing processes contributed to efficiently introduce the oxygen into the ZnO thin films, leading to the growth of ZnO nanostructures. The large size ZnO nanostructures were fabricated after the multiple annealing procedures.

Annealing Gas	Time (h)	Temperature (℃)
H_2 in N_2: 1.9%	3	300
H_2 in N_2: 1.9%	2	450
O_2	0~1	450
H_2 in N_2: 1.9%	3	450

Fig. 4.1 The multiple annealing processes with different oxygen treatment time

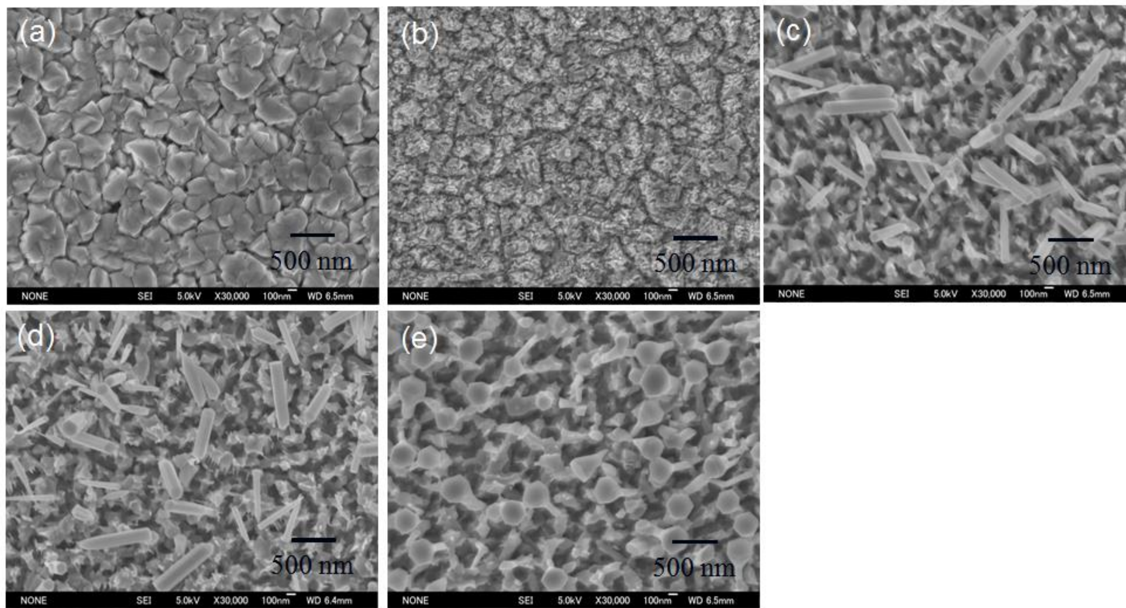

Fig. 4.2 SEM images of (a) as-deposited ZnO films and fabricated ZnO nanostructures with (b) 0min (c) 15min, (d) 30min, and (e) 60min.

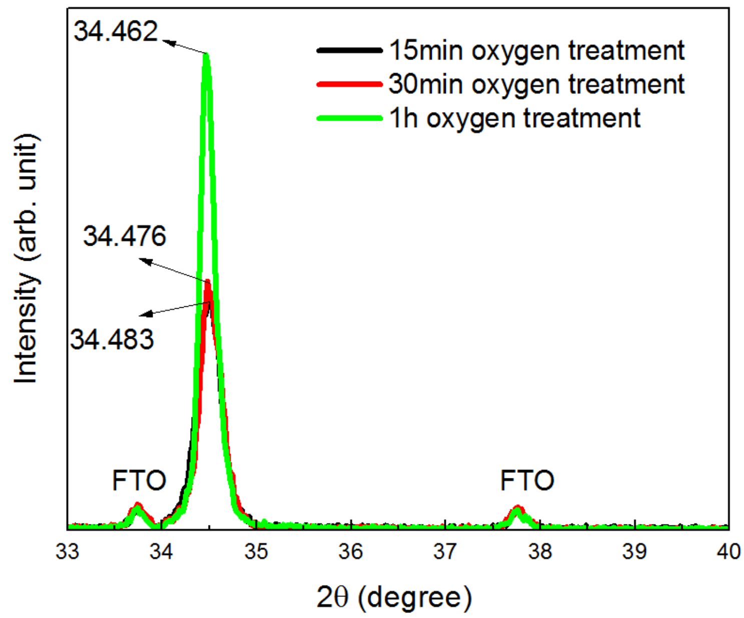

Fig. 4.3 The XRD spectras of ZnO nanostructures with different oxygen annealing treatment time.

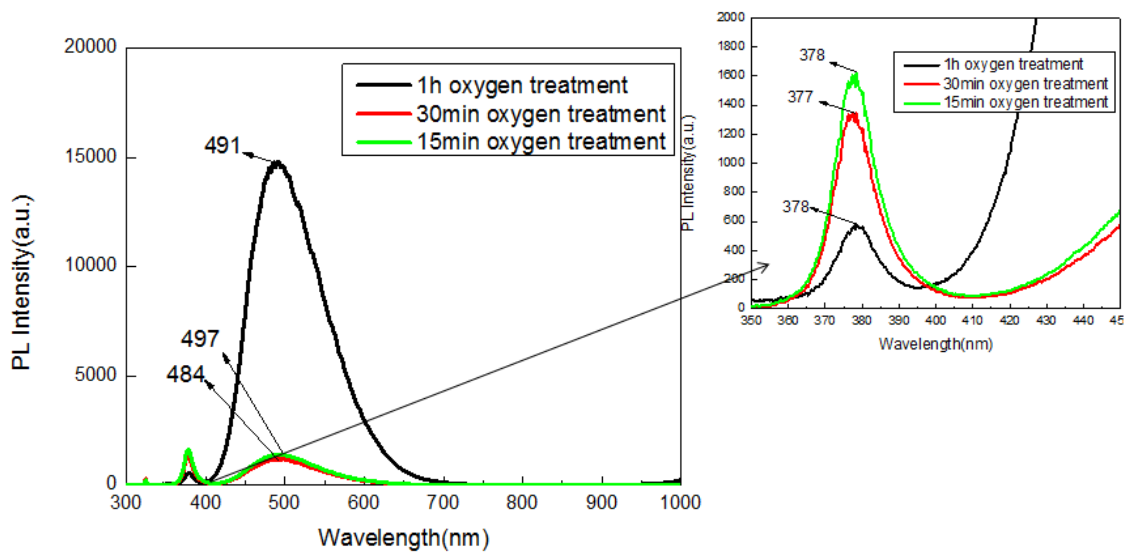

Fig. 4.4 The PL spectras of ZnO nanostructures with different oxygen treatment time.

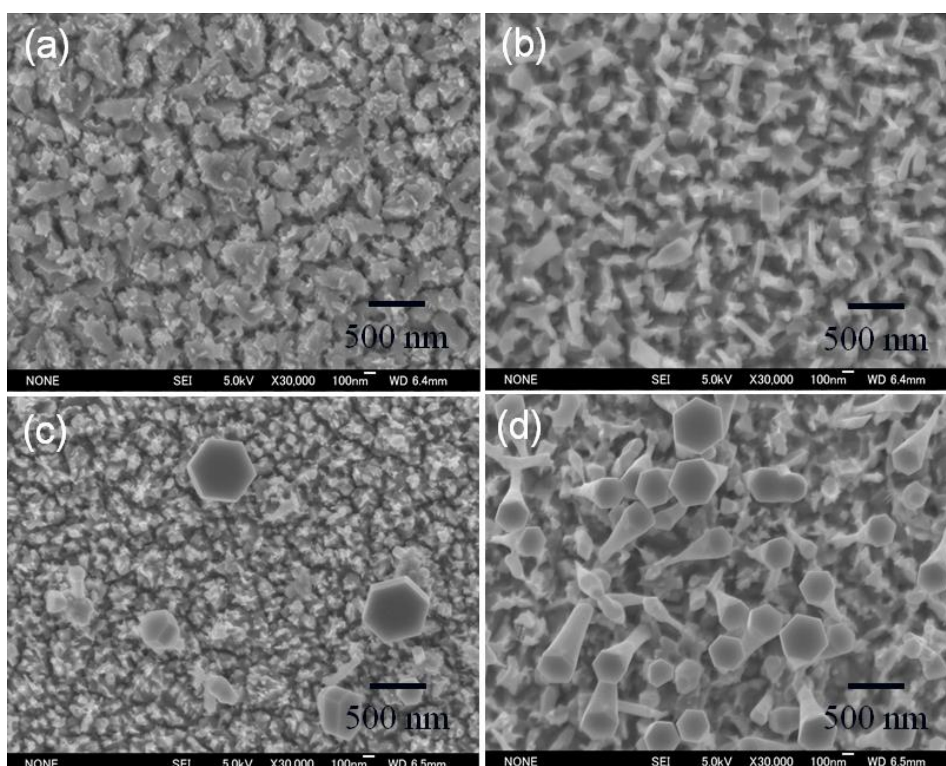

Fig. 4.5 The SEM images of obtained ZnO nanostructures with different oxygen treatment time.

(a:0min, b:15min, c:30min, d: 60min)

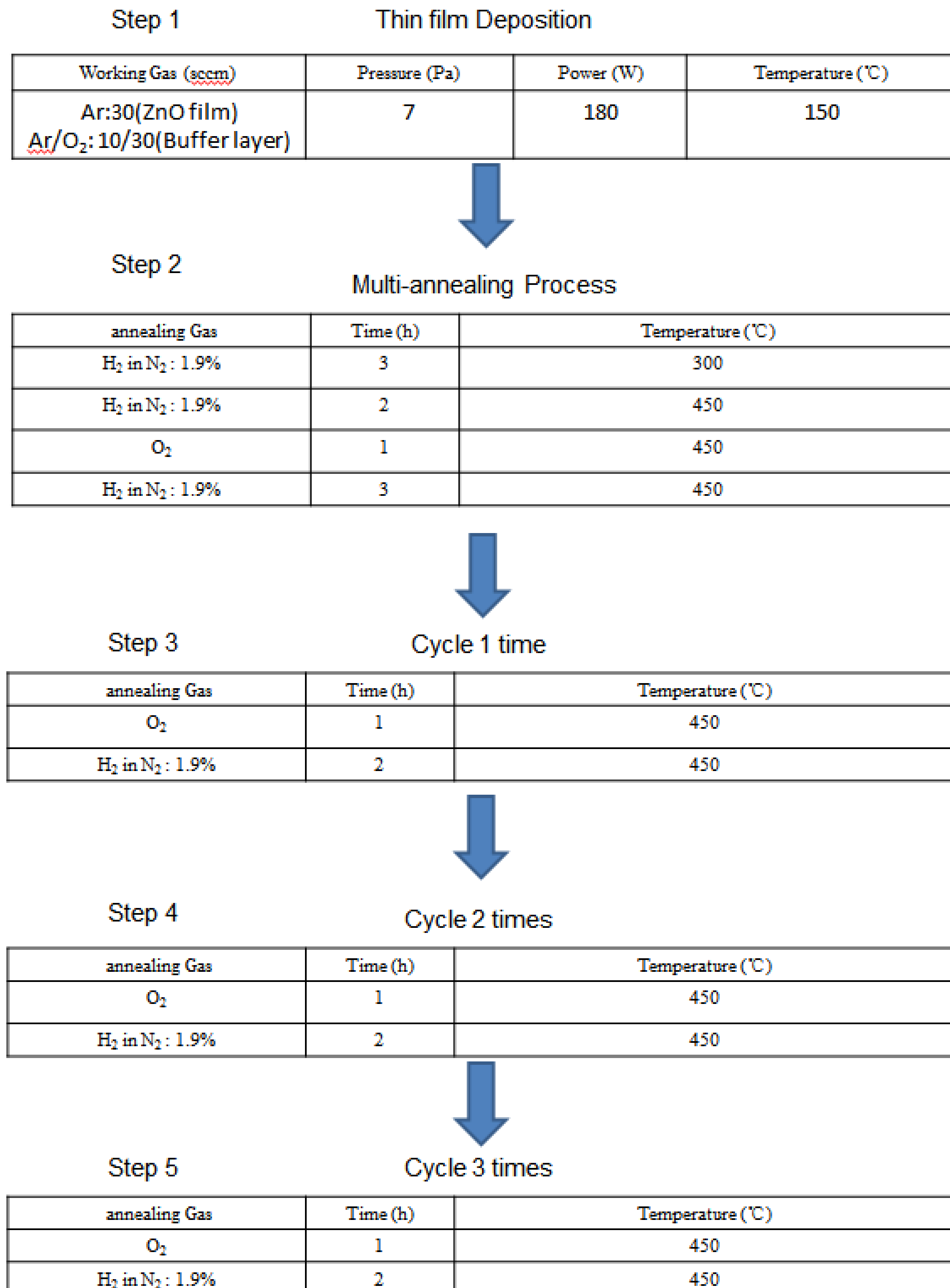

Step 1 Thin film Deposition

Working Gas (sccm)	Pressure (Pa)	Power (W)	Temperature (℃)
Ar:30(ZnO film) Ar/O_2: 10/30(Buffer layer)	7	180	150

Step 2 Multi-annealing Process

annealing Gas	Time (h)	Temperature (℃)
H_2 in N_2 : 1.9%	3	300
H_2 in N_2 : 1.9%	2	450
O_2	1	450
H_2 in N_2 : 1.9%	3	450

Step 3 Cycle 1 time

annealing Gas	Time (h)	Temperature (℃)
O_2	1	450
H_2 in N_2 : 1.9%	2	450

Step 4 Cycle 2 times

annealing Gas	Time (h)	Temperature (℃)
O_2	1	450
H_2 in N_2 : 1.9%	2	450

Step 5 Cycle 3 times

annealing Gas	Time (h)	Temperature (℃)
O_2	1	450
H_2 in N_2 : 1.9%	2	450

Fig. 4.6 The annealing processes of different steps.

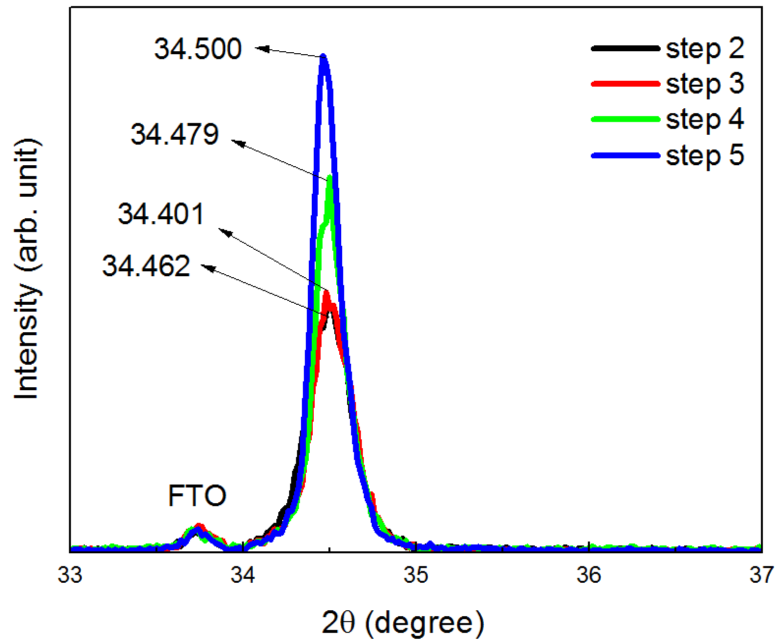

Fig. 4.7 The XRD patterns of ZnO nanostructures with different multiple annealing processes.

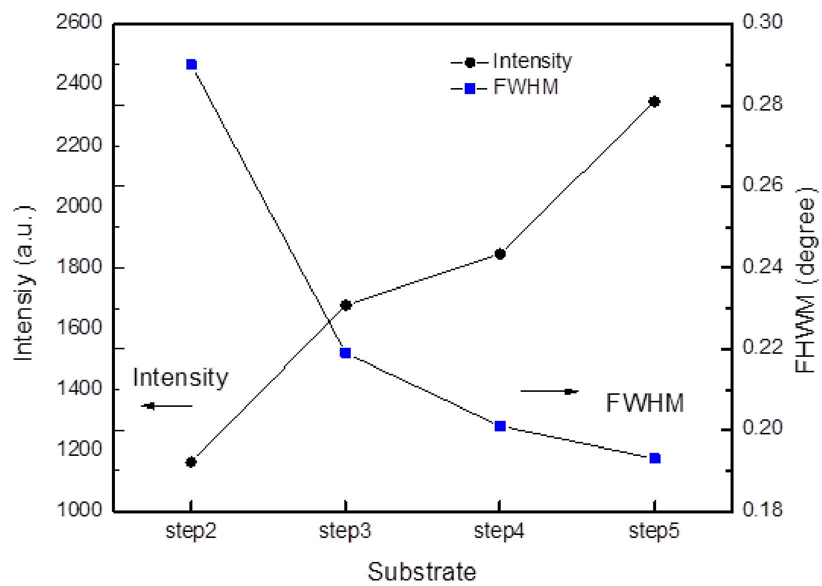

Fig. 4.8 Dependence of intensity and FWHM of obtained ZnO nanostructures on different annealing processes.

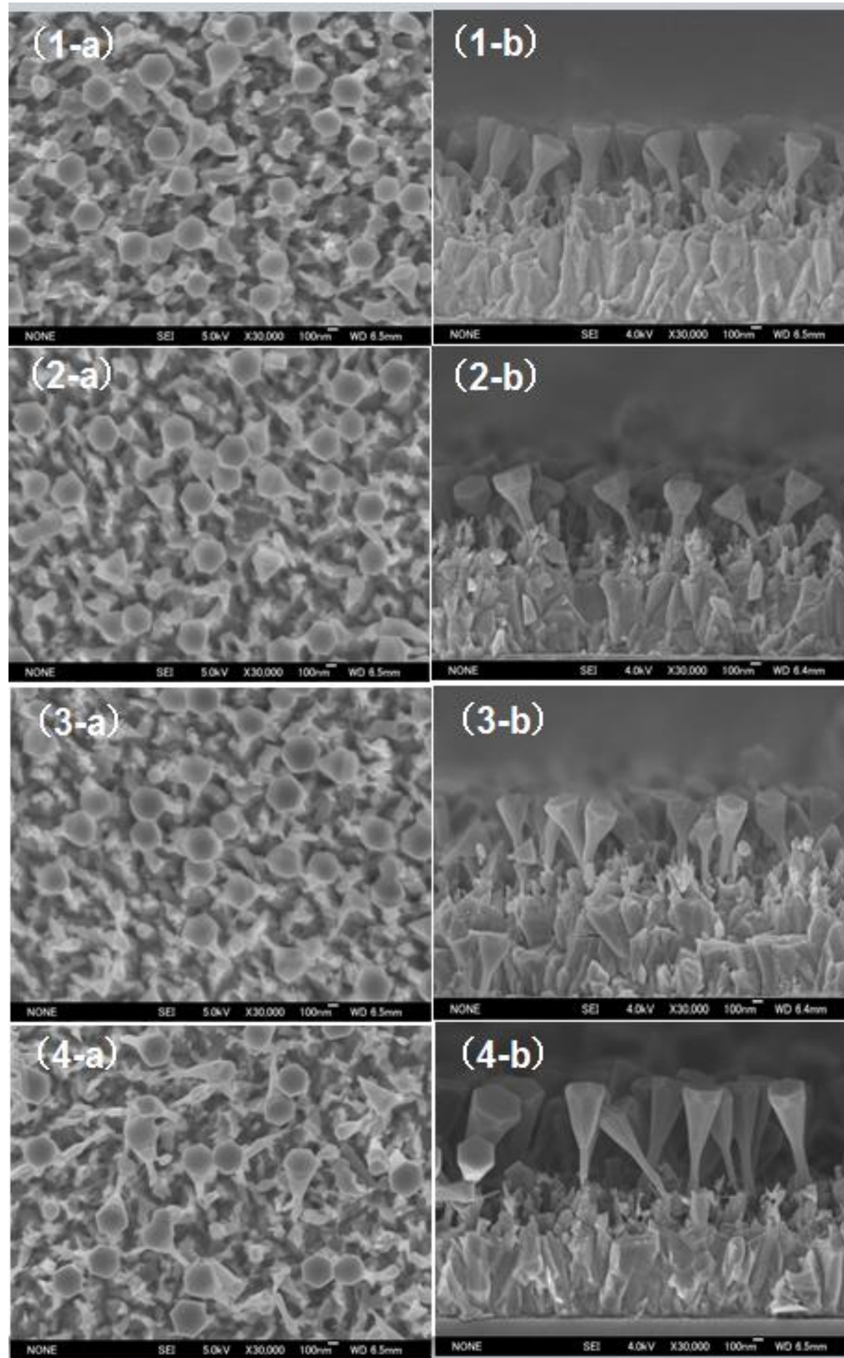

Fig. 4.9 The SEM images of ZnO nanostructures with different multiple annealing processes

(1: step 1, 2: step 2, 3: step 3, 4: step 4

a: top view, b: cross-section view)

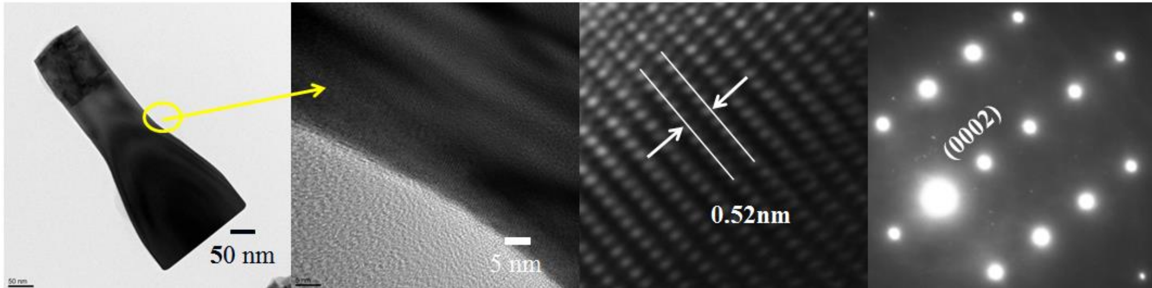

Fig. 4.10 The HRTEM images of a ZnO nanorod obtained from the multiple annealing processes

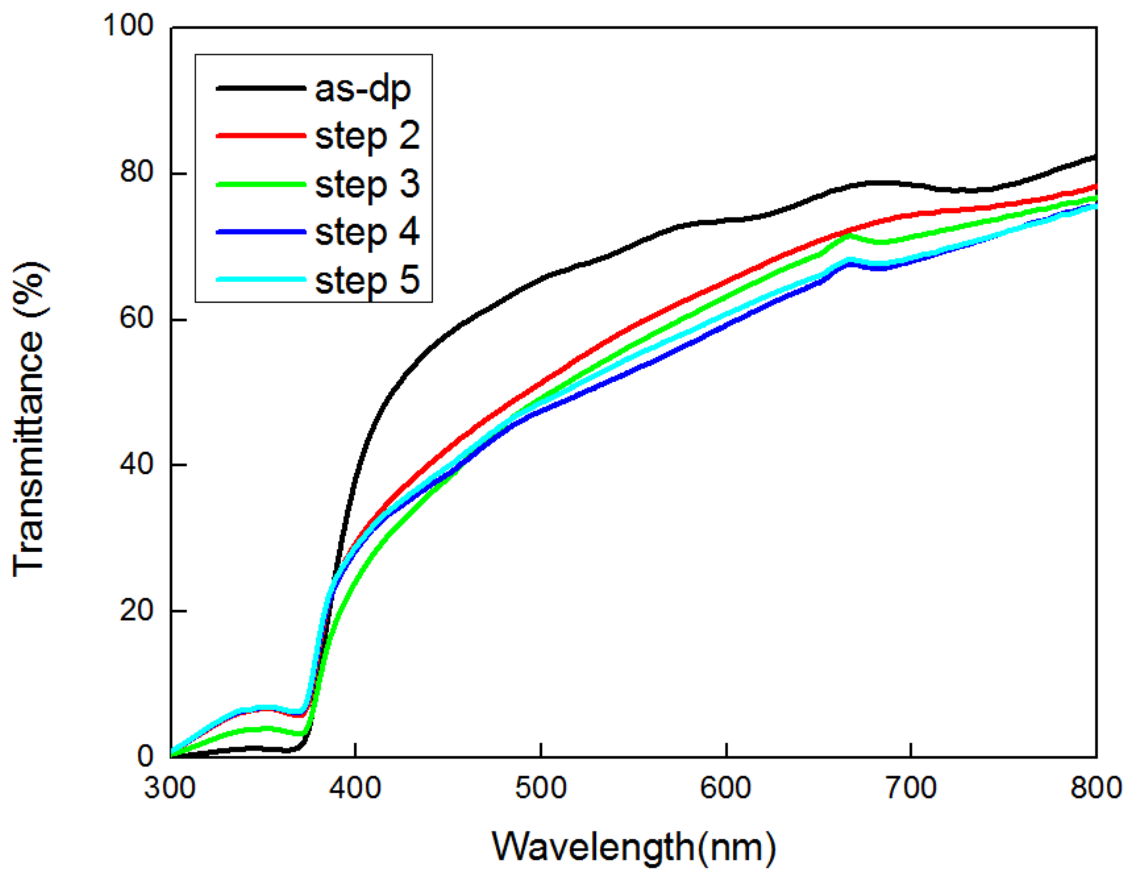

Fig. 4.11 The transmittance of ZnO nanostructures with different multiple annealing processes.

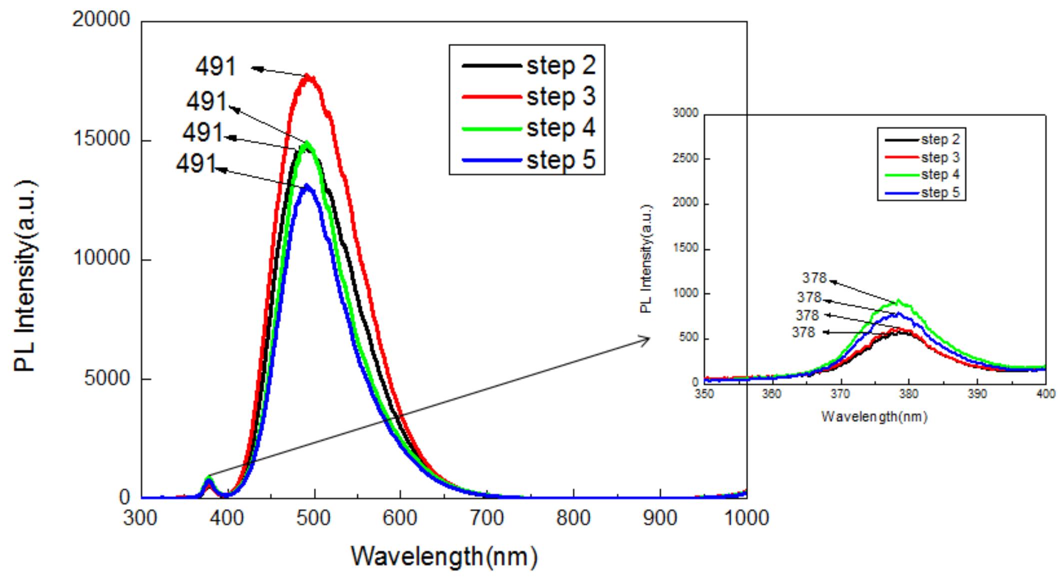

Fig. 4.12 The PL spectra of ZnO nanostructures with different multiple annealing processes.

Reference

1 J. Huang, Z.G. Yin and Q.D. Zheng, Energy Environ, Sci., 4 (2011) 3861.

2 Q.H. Li, Q. Wan, Y.X. Liang, T.H. Wang, Appl. Phys. Lett. 84 (2004) 4556.

3 S. Choi, J. W. Kang, D. K. Hwang and S. J. Park, IEEE Transactions on Electron Devices, 57 (2010) 26.

4 B.F. Martinson, J.W. Elam, J.T. Hupp, and M.J. Pellin, Nano Lett. 7 (2007) 254.

5 T. Aoki, Y. Hatanaka, D. C. Look, Appl. Phys. Lett. 76 (2000) 3257.

6 J. Wu, S. Liu, Adv. Mater. 14 (2002) 215.

7 Z. Li, X. Huang, J. Liu, Y. Li, G. Li, Materials Letters 62 (2008) 1503

8 J. Yang, M. Gao, L. Yang, Y. Zhang, J. Lang, D. Wang, Y. Wang, H. Liu, H. Fan, Applied Surface Science 255 (2008) 2646.

9 R.B. Peterson, C.L. Fields, B.A. Gregg, Langmuir 20b(2004) 5114.

10 L. Yang, Q. Zhao, M. Willander, J. Yang, J. Crystal Growth 311 (2009) 1046.

11 C. Y. Li, T. Kawaharamura, T. Matsuda, H. Furuta, T. Hiramatsu, M. Furuta, T. Hirao, J. Appl. Phys. Express., 2. (2009) 091601.

12 D.P. Wang, Z.M. Li, T. Kawaharamura, M. Furuta, T. Narusawa, and C.Y. Li, Phys. stat. Sol. (c), 9 (2012) 196.

Chapter 5

Morphology modification of ZnO nanostructures by Mist CVD treatment

5.1 Introduction

ZnO is an import wide bandgap semiconductor [1-3]. In last two chapters, we have succeeded in obtaining the well-aligned large size ZnO nanostructures on ZnO film using multiple annealing techniques [4-6]. However, the morphology of ZnO nanostructures still needed to be enlarged for the photovoltaic application. In this chapter, a novel mist chemical vapor deposition method (Mist CVD) was firstly introduced to treat obtained ZnO nanostructures from reducing annealing process.

The Mist CVD was a novel chemical vapor deposition method. The figure of Mist CVD was shown in Fig. 5.1. In this chapter, the effects of Mist CVD treatment conditions including (1) treatment time (0~75min) and (2) the carrier gases (air and argon) on the properties of obtained ZnO nanostructures were investigated.

Firstly, the influence of carrier gases in Mist CVD on the properties of ZnO nanostructures was discussed. The carrier gases in Mist CVD have great influence on the fabrication of the ZnO nanostructures in Mist CVD system. Adjusting of Mist CVD carrier gases would change the crystallinity and morphology of the obtained ZnO nanostructures.

Then, the influence of Mist CVD post-treatment time on the properties of ZnO nanostructures was discussed. Adjusting of Mist CVD treatment time was the direct way

to control the modification of ZnO nanostructures.

5.2 Carrier gas dependence

5.2.1 Experiments

ZnO film (thickness 1um) was firstly deposited on Si substrate by radio frequency (RF, 13.5 MHz) magnetron sputtering method. The ZnO nanostructures were formed by a following multiple annealing process in the reducing ambient at 450 ℃.

In this reducing annealing processes, firstly the ZnO film was annealed in a reducing gas ambient (H_2 in N_2: 1.9%) for 2 h, then annealed in O_2 for 1 h followed by a reducing annealing in the same condition as the first step with extending annealing time to 8h.The annealing temperature was kept at 450 ℃ for this processes. For safety, N_2 was introduced shortly to the furnace between every two steps. ZnO nanostructures were fabricated on the ZnO thin film, as shown in Fig. 5.1.

Figure 5.2 (a) showed the as-deposited ZnO thin film by RF magnetron sputtering. The average grain size was about 200nm. After reducing annealing process, it was found that there were ZnO nanostructures appearing on ZnO thin film. The top diameter and the height of ZnO nanostructures were 180nm and 1050nm, respectively, as shown in Fig. 5.2(b).

The prepared ZnO nanostructures on ZnO film were put into the quartz reaction channel in Mist CVD system. The solvents and solutes were respectively methanol/H_2O (9:1) and zinc acetylacetonate ($Zn(Acac)_2$) (0.02mol/L). The ultrasonic frequency applied through a transducer was 2.4 MHz, the carrier and dilution gas were both air at the flow rate of 2.5 L/min and 4.5 L/min respectively. The channel was heated at 430 ℃ during Mist CVD process. Two kinds of carrier gases were selected, air and argon. The treatment time was 5min and 30min for comparison.

The condition of Mist CVD post-treatment was summarized in the Table 5.1.

Table 5.1 Mist CVD conditions for ZnO nanostructures growth in air

Zinc Source	$Zn(Acac)_2$
Concentration	0.02mol/L
Solvent	Methanol/H_2O(9:1)
Temperature	430 ℃
Carrier gas flow rate	2.5L/min
Dilute gas flow rate	4.5L/min
Carrier gas	air/argon
Time	5min, 30min

5.2.2 Results and discussion

Figure 5.3 showed the SEM images of as-deposited ZnO nanostructures and the ZnO nanostructures obtained from different carrier gases. The results indicated that the morphology of ZnO nanostructures was significantly modified after Mist CVD treatmen. It was obviously that the appearance of the ZnO nanorods obtained from reducing annealing was nearly smooth. After 5min Mist CVD treatment, there was small nuclei growth on the total surface of ZnO nanorods from Fig. 5.3(2-3). When time extended to 30min. the nanosheets appeared on the surface of ZnO nanostructures, meaning the grownup of the nuclei on the surface of ZnO nanostructures with extending the treatment time.

However, the surface mopholgy of ZnO nanostructures obtained from different carrier gases was different. The nuclei obtained from carrier gas argon showed better

alignment compared with the nuclei obtained from carrier gas air. When time extended to 30min. the intertwined nanosheets appeared on the surface of ZnO nanostructures in the carrier gas air while the well-aligned nanosheets appeared on the surface of ZnO nanostructures in the carrier gas argon.

In the Mist CVD treatment process, the solute was $Zn(Acac)_2$ which was dissolved in methenol/H_2O (9:1) following by atomized to form mist droplets in the diameter scale of several micrometers with ultrasonic transducer. The mist droplets were transferred by the argon gas from the supply unit to the reaction unit in which the ZnO nanorods on ZnO film obtained from reducing process was set.

During this treatment process, there were two parts of zinc sources supplied. One was the zinc atoms remained on ZnO nanorods after reducing annealing process, which can serve as self-catalyst to contribute to ZnO nanostructures growth on the place zinc atoms located on the surface of ZnO nanorods. The second zinc source was from solution of Mist CVD method. The mist droplets derived from $Zn(Acac)_2$ solutions could decompose to release free zinc atoms if the temperature increased over 250 ℃. In this experiment, the temperature of reaction unit was 430 ℃, so there were many free zinc atoms to contribute to nanostructures growth.

If the carrier gas was air, mist droplets carried by air were imported to the reaction unit. Zinc atoms in the surface of nanostructures reacted with oxygen from the air immediately to form ZnO nuclei. $Zn(Acac)_2$ in the mist droplets started to decompose to release zinc atoms to react with oxygen to form ZnO on the place the ZnO nuclei existed.

If the carrier gas was argon gas, Zinc atoms in the surface of nanorods reacted with oxygen immediately to form ZnO nuclei. $Zn(Acac)_2$ in the mist droplets started to

decompose to release zinc atoms to react with oxygen to form ZnO on the place the ZnO nuclei existed, meaning that the growth of ZnO nanostructures was epitaxial growth in the carrier gas argon.

When Mist CVD treatment time was extended to 30min, ZnO nuclei continued to grow up. From previous reports [4-8], ZnO fabricated by chemical vapor deposition (CVD) method in aqueous solution showed the morphology of nanorods. But in our research, solvent was 90% methanol with only 10% H_2O, meaning less hydroxyl groups would appear on the surface of ZnO nuclei compared with in aqueous solution. The research of Pan et al. [9] indicated that less hydroxyl groups on the surface of ZnO nuclei would increase the packing probability of ZnO nuclei in the direction including c-axis, making only one direction with OH restricted during growth. Therefore, when carrier gas was air, ZnO nuclei on the ZnO nanostructures grew into intertwined nanosheets covered all over the surface while ZnO nuclei on the ZnO nanostructures grew into well-aligned nanosheets, when the carrier gas was argon gas, as shown in Fig. 5.3(4-5).

The HRTEM images of ZnO nanostructures and ZnO nanostructures after Mist CVD treatment for 30min were shown in Fig. 5.4.

Figure 5.4(1) showed the high-resolution image and selected area electron diffraction (SAED) of ZnO nanostructures obtained from reducing annealing process. The results indicated that the ZnO nanostructures were highly c-axis orientation with constant c was 0.52nm. The SAED patterns were shown in Fig. 5.4(1-c). The perfect regular spots revealed that ZnO nanostructures showed good single crystal.

Figure 5.4(2) showed the high-resolution image and SAED of ZnO nanostructures after Mist CVD treatment in argon gas for 30min. The results indicated that the ZnO

nanostructures were highly c-axis orientation with constant c was 0.52nm. The SAED patterns were shown in Fig. 5.4(2-c). The perfect regular spots revealed that ZnO nanostructures showed good single crystal. Also, the XRD patterns of ZnO nanostructures after Mist CVD treatment in argon gas indicated that the obtained ZnO nanostructure has only one crystal direction (002), meaning that ZnO nanostructures after Mist CVD treatment in argon gas showed good single crystal structure.

Figure 5.4(3) showed the high-resolution image and SAED of ZnO nanostructures after Mist CVD treatment in air for 30min. The results indicated that the ZnO nanostructures were highly c-axis orientation with constant a was 0.32nm. The SAED patterns were shown in Fig. 5.4 (3-c). The spots revealed that ZnO nanostructures were polycrystalline.

5.2.3 Summary

The influence of carrier gases on the modification of well-aligned ZnO nanostructures was investigated. The results indicated the crystallinity and surface morphology of ZnO nanostructure were quite different. Choosing the suitable carrier gases in Mist CVD treatment can help us obtaining the ZnO nanostructures with the designed crystallinity and surface morphology.

5.3 Mist CVD treatment time dependence

5.3.1 Experiments

The ZnO nanostructures were fabricated by the same process with chapter 5.2.

The prepared ZnO nanostructures on ZnO film were put into the quartz reaction channel in Mist CVD system. In this section , we modulated the Mist CVD treatment time of 5min, 30min, 45min, 60min, and 75nm to investigate the influences of Mist CVD treatment time on the properties of ZnO nanostructures. Other conditions of Mist

CVD post-treatment were the same as in Chapter 5.2.

5.3.2 Results and discussion

5.3.2.1 Carrier gas: air

Fig. 5.5 (1-a) to (6-a) showed the top view SEM images of ZnO nanostructures obtained from Mist CVD post-treatment processes in air. It was observed that top diameter of ZnO nanostructures had little change after 5min, compared with the ZnO nanostructures without Mist CVD treatment. When Mist CVD treatment time increased up to 75min, top diameter increased significantly until reach to 1600nm at 75min, then unified finally, as shown in Fig. 5.5.

Fig. 5.5 (1-b to 6-b) showed the cross section view SEM images of ZnO nanostructures. Combined with Fig. 5.6, it was clearly found that the height of nanostructures increased from 1050nm to 1520nm until treated after 75min with the growth rate 6nm/min in vertical direction.

Comparing with the top diameter increase, the bottom diameter almost as same as linearly increased from 100nm to 1250nm with the growth rate 20nm/min. The above results showed the ZnO nanostructures regrowth much faster in the horizontal direction than that in the vertical direction in the Mist CVD processes.

The XRD patterns of ZnO nanostructures obtained after Mist CVD post- treatment for different time were shown in Fig. 5.7(a).

It was observed there were two peaks (002) and (101) in the XRD patterns, Compared with (101) peak, (002) peak obviously was dominated with much higher intensity for all the samples, which revealed that all of the ZnO nanostructures had highly (002) preferred orientations with a c-axis perpendicular to the substrates.

Fig. 5.7(b) showed the dependence of intensity and FWHM of ZnO nanostructures on

different Mist CVD treatment time.

Fig. 5.7(b) indicated that intensity of (002) peaks decreased as well as FWHM increased from 0.224 to 0.279 with the Mist CVD time increase until 45min. Combined with the SEM images shown in Fig. 5.3, we could find that the ZnO nanostructures regrew both in vertical and horizontal directions, getting to approach each other until 45min. However, the intensity of (002) peaks was increased and FWHM decreased from 0.279 to 0.177 after the nanostructures reached each other and formed the film again when the time was over 45min.

Fig. 5.8 showed the PL spectra of ZnO nanostructures obtained after Mist CVD post-treatment for different time. It was found that the blue-green emission centered at 491nm was obtained from the all of samples with the suppressed UV emission about 378nm. The green emission was related to the oxygen vacancy in the ZnO nanostructures [4]. When the ZnO nanostructures treated with the carrier gas air, the oxygen vacancy would be filled by oxidation effect in the air, resulting in the less oxygen vacancy. Therefore, the visible peak decreased with increasing the annealing time. The UV peak density also decreased with extending the treatment time due to the gradual decrease of the optical crystallinity.

5.3.2.2 Carrier gas: argon

Fig. 5.9 (1-a) to (6-a) showed the top view SEM images of ZnO nanostructures obtained from Mist CVD post-treatment processes. It was observed that the ZnO nanostructures had slight modified after 5min. When Mist CVD treatment time increased up to 75min, top diameter increased significantly until reaching to 1620nm at 75min, then unified finally.

Fig. 5.9 (1-b to 6-b) showed the cross section view SEM images of ZnO

nanostructures. Combined with Fig. 5.10, it was clearly found that the height of nanostructures increased from 1050nm to 1620nm until treated after 75min with the growth rate 7.6nm/min in vertical direction. The bottom diameter almost as same as linearly increased from 100nm to 1440nm with the growth rate 20nm/min.

The results showed the ZnO nanostructures regrowth much faster in the horizontal direction than that in the vertical direction in the Mist CVD processes.

The XRD patterns of ZnO nanostructures obtained after Mist CVD post-treatment for different time were shown in Fig. 5.11.

It was obvious that the (002) diffraction peak was dominated peak which was oriented highly perpendicular to the plane of the substrate for these samples. (101) diffraction peak also appeared in the XRD patterns, indicating the crystal growth in (101) direction also happened during Mist CVD treatment.

Fig. 5.12 showed the PL spectra of ZnO nanostructures obtained after Mist CVD post- treatment for different time. It was found that the blue-green emission centered at 491nm was obtained from the all of annealed samples, with the UV emission about 378nm. The PL results showed that the visible peak was suppressed with extending the treatment time in argon gas as while as the UV peak was enhanced.

5.3.3 Summary

The influence of Mist CVD treatment time on the modification of well-aligned ZnO nanostructures was investigated. If the Mist CVD treatment time was increased, the surface morphology of ZnO nanostructures were modified with covering nanosheets and the size of ZnO nanostructures was enlarged. The size and morphology of ZnO nanostructure can be well controlled by modulating the Mist CVD treatment time.

5.4 Conclusions

In this chapter, ZnO nanostructures with well-controlled growth on silicon substrate were fabricated in a reducing gas ambient following by a novel mist chemical vapor deposition (Mist CVD) treatment in air and argon gas. The effects of Mist CVD carrier gases and treatment time on the crystal growth, structural properties were investigated.

1) The obtained ZnO nanostructures exhibited different morphology and crystallinity with different carrier gases: the growth of ZnO nanostructures was epitaxial growth in the carrier gas Argon, indicating the obtained ZnO nanostructures were good single crystal with well-aligned ZnO nanosheet on the surface; the growth of ZnO nanostructures were random in the carrier gas Air, resulting in the obtained ZnO nanostructures were polycrystalline with intertwined nanosheets on the surface. Choosing the suitable carrier gases can help us obtaining the ZnO nanostructures with the designed crystallinity and surface morphology.

2) With the increase of Mist CVD treatment time, the surface morphology of ZnO nanostructures were modified with intertwined (carrier gas: air) and aligned (carrier gas: argon) nanosheets and the size of ZnO nanostructures was enlarged. The size and morphology of ZnO nanostructure can be well controlled by modulating the Mist CVD treatment time.

Fig. 5.1 The figure of Mist CVD system

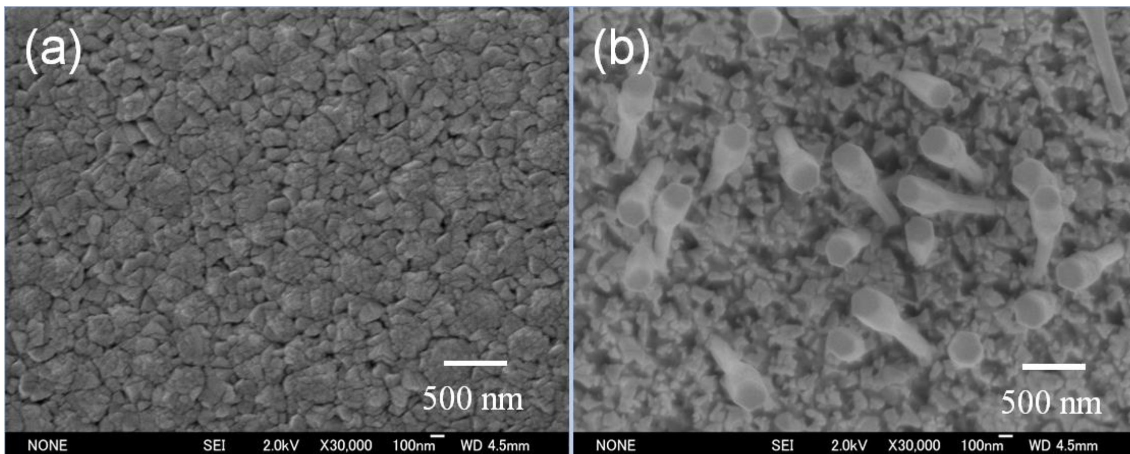

Fig. 5.2 The SEM images of (a) as-deposited ZnO film and (b) ZnO nanostructures obtained from reducing annealing process

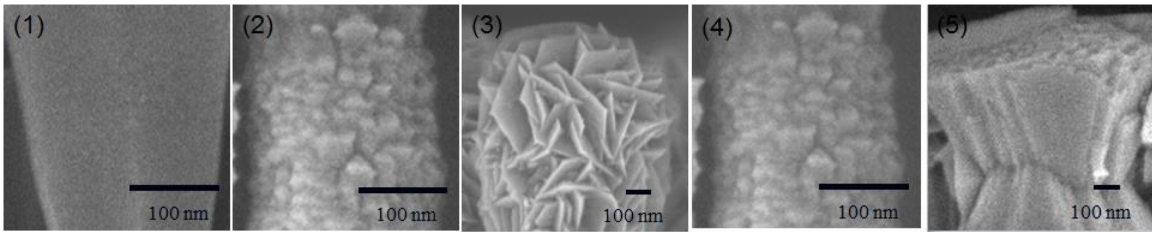

Fig. 5.3 Influence of Mist CVD treatment time (1) after reducing annealing; (2) 5min in air (3)30min in air (4) 5min in argon (5)30min in argon.

Fig. 5.4 The HRTEM images of ZnO nanorods obtained from different processes. (1: after reducing annealing, 2: after Mist CVD treatment in argon for 30min, 3: after Mist CVD treatment in air for 30min)

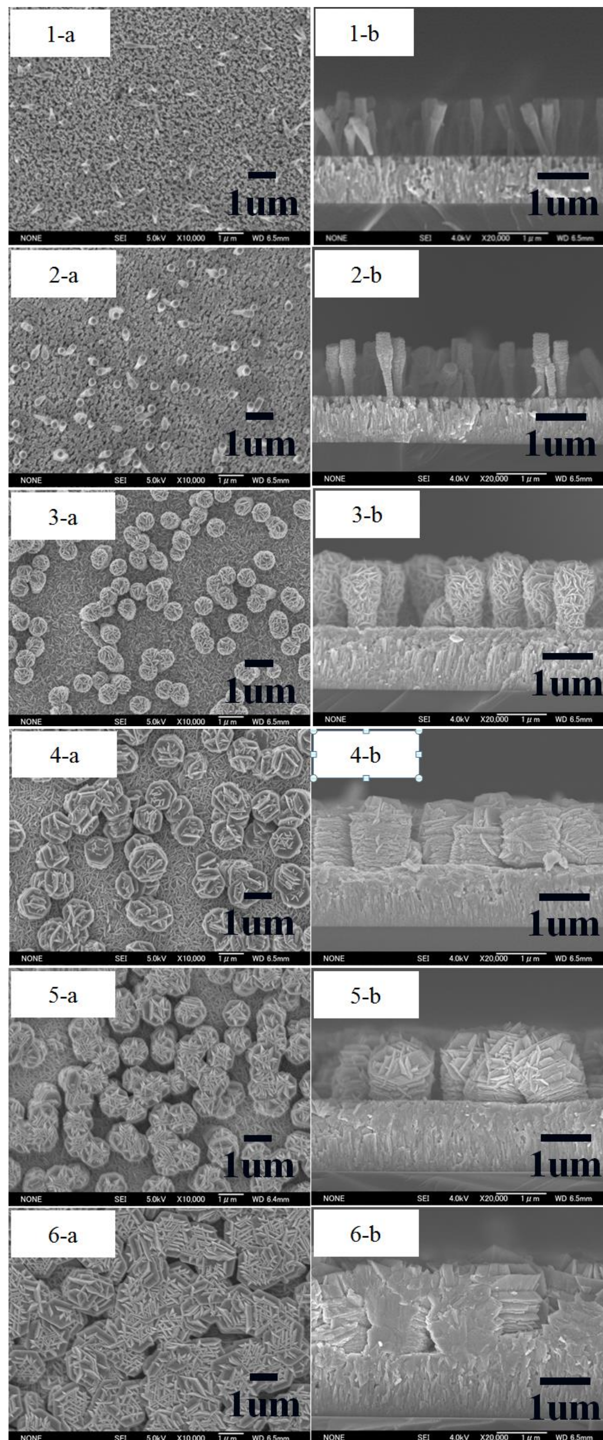

Fig. 5.5 SEM images of ZnO nanostructures regrowth after treated in Mist CVD in air for (1) 0 min (2)5min, (3)30min, (4)45min, (5)60min, (6)75min.

(a: top view and b: cross section view)

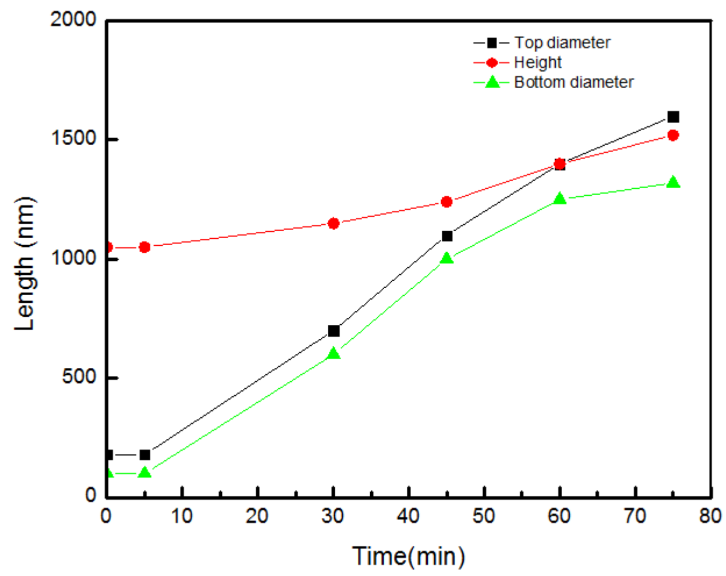

Fig. 5.6 Relationship between regrowth of ZnO nanostructures and Mist CVD post-treatment time in air

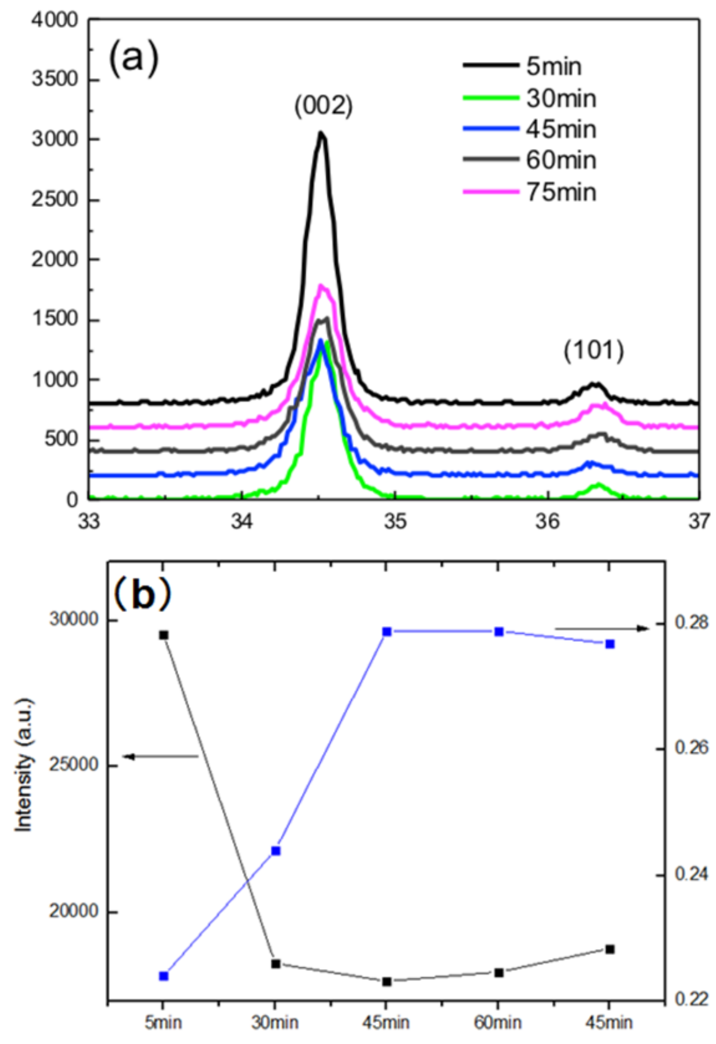

Fig. 5.7 (a) XRD patterns and (b) intensity and FWHM of ZnO nanostructures with different Mist CVD treatment time in air

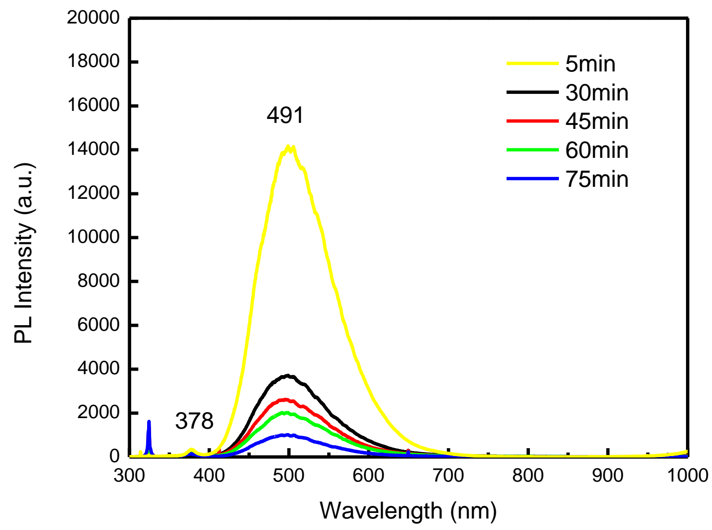

Fig. 5.8 PL spectras of ZnO nanostructures with different Mist CVD treatment time in air.

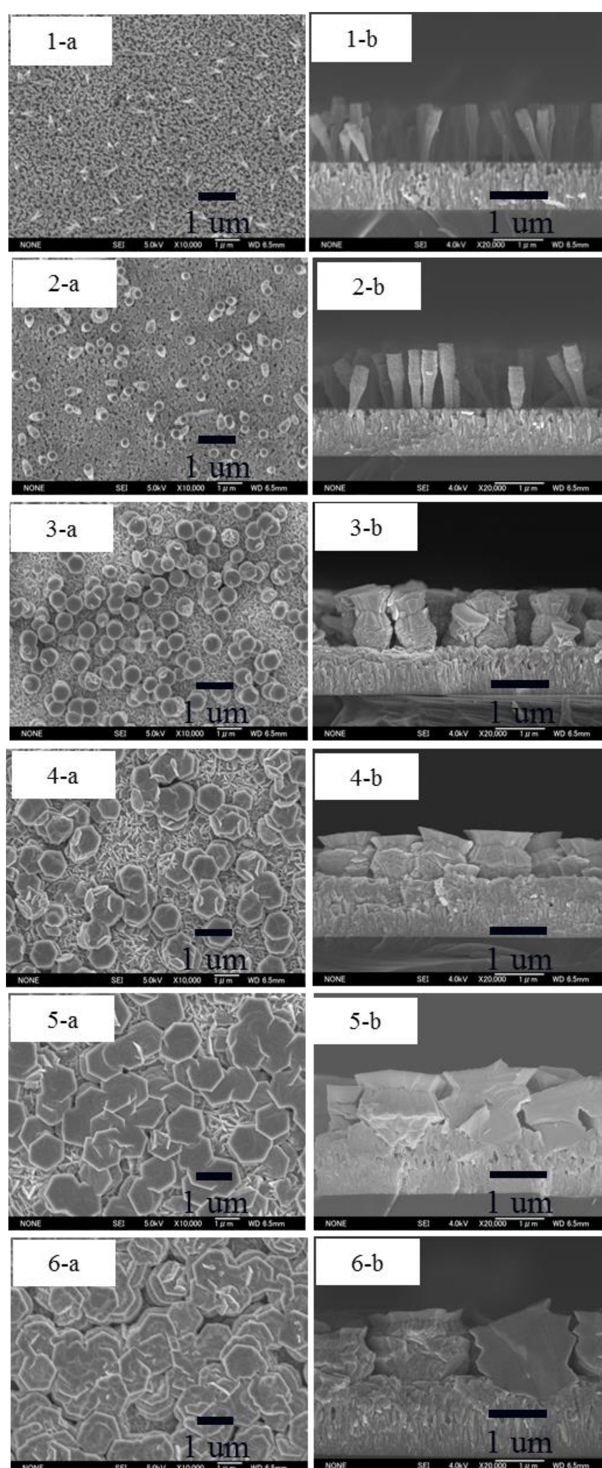

Fig. 5.9 SEM images of ZnO nanostructures regrowth after treated in Mist CVD in argon for (1) 0 min (2)5min, (3)30min, (4)45min, (5)60min, (6)75min.

(a: top view and b: cross section view)

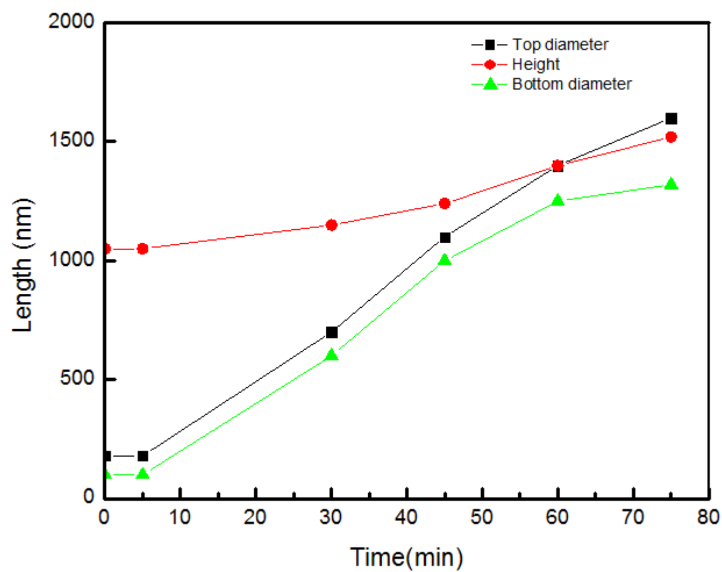

Fig. 5.10 Relationship between regrowth of ZnO nanostructures and Mist CVD post-treatment time in argon

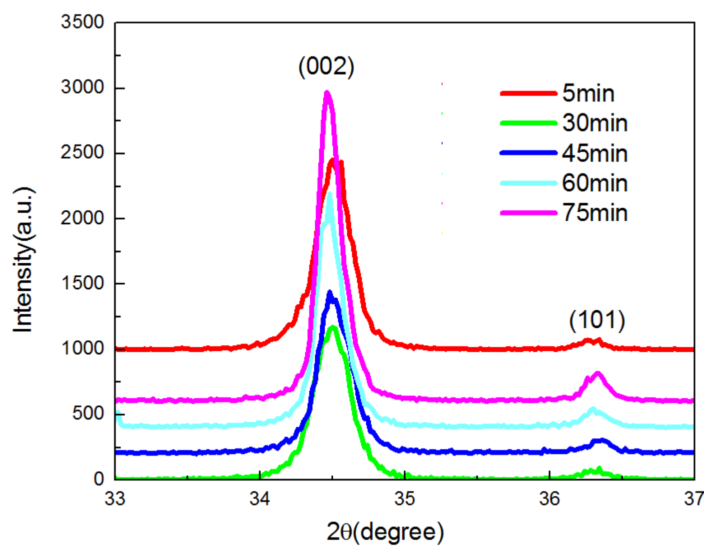

Fig. 5.11 XRD patterns of ZnO nanostructures on Mist CVD treatment time in argon

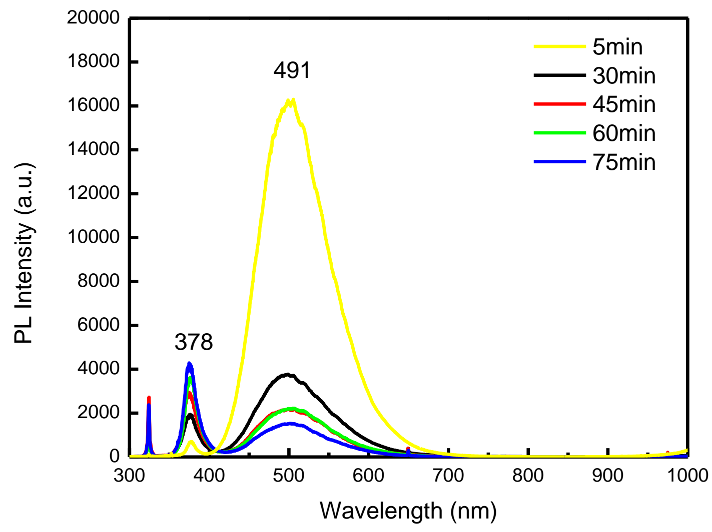

Fig. 5.12 PL spectra of ZnO nanostructures on Mist CVD treatment time in argon

Reference

1 J. Yang, M. Gao, L. Yang, Y. Zhang, J. Lang, D. Wang, Y. Wang, H. Liu, H. Fan, Appli. Surf. Sci. 255 (2008) 2646.

2 R.B. Peterson, C.L. Fields, B.A. Gregg, Langmuir. 20b (2004) 5114.

3 L. Yang, Q. Zhao, M. Willander, J. Yang, J. Crystal Growth. 311 (2009) 1046.

4 C. Y. Li, T. Kawaharamura, T. Matsuda, H. Furuta, T. Hiramatsu, M. Furuta, T. Hirao, J. Appl. Phys. Express. 2 (2009) 091601.

5 C. Y. Li, T. Matsuda, T. Kawaharamura, H. Furuta, M. Furuta, T. Hiramatsu, T. Hirao, T. J.Vac. Sci. Technol. B. 28 (2010) C2B51.

6 T. Kawaharamura, H. Orita, T. Shirahata, A. Yoshida, S. Fujita, T. and Hirao, Phisica Status Solidi(C). 9 (2012) 190.

7 D.P. Wang, Z.M. Li, T. Kawaharamura, M. Furuta, T. Narusawa, and C.Y. Li, Phys. stat. Sol. (c), 9 (2012) 2.

8 W.Q. Peng, S.C. Qu, G.W. Cong, Z.G. Wang, Cryst. Growth Des. 6 (2006) 1518.

9 A.L. Pan, R.H. Yu, S.S. Xie, Z.B. Zhang, C.Q. Jin, B.S. Zou, J. Cryst. Growth 3 (2005) 282.

Chapter 6

ZnO-based DSSC fabrication and applications

6.1 Introduction

Recent years, the dye-sensitized solar cell (DSSC) attracted more and more attention due to its low cost and easy to scale up [1-3]. However, the development of DSSC has reached bottleneck in the improvement of efficiency. A variety of problems prevented the DSSC to obtain higher efficiency.

Firstly, TiO_2 was used as photoanode in the traditional DSSC. The common TiO_2 was nanocrystalline porous films [2-5]. But the results exhibited that porous TiO_2 film was not so high efficiency in the absorption of dye molecules. Most of the film surface was ineffective due to the huge number of defects and dislocations in the boundary of different nanoparticles [6-7]. So to increase the effective surface area is the key to increase the absorption of dye molecules resulting in the efficiency increase. In order to increase the effective surface area, researchers tried to fabricate the textured TiO_2 nanostructures which could significantly increase the effective surface area. However, due to the difficulty to achieve textured TiO_2 nanostructures, another idea was proposed that find other material to replace TiO_2 [8-10].

Secondly, as shown in Fig. 6.1, the semiconductor electron transport was often simulated as the trapping and thermal release of electrons from a distribution of sub-bandedge states, which was relied on the Fermi level of the semiconductor. One major limitation for the traditional photoanode is the low electron diffusion coefficient

(Dn) in nanoparticle film, which is in the order of 10^{-4} cm^2/s[40]. However, this value was increased in the order of 10^{-2} cm^2/s in the single crystal TiO_2, almost thousand times larger than that in the monocrystalline TiO_2 film. The slow electron transport significantly limited the choice of redox couple in the electrolyte which in turn limited the photo voltage and constrained the choice of dye sensitizer.

In this regard, photoelectrode with new architectures especially one-dimensional (1-D) nanostructures drew widely interest and have been intensively studied, due to the effectively facilitating electron collection and enlarging the effective surface area. Therefore, ZnO nanostructures were paid more interest to be used as photoelectrode in DSSC application. Comparing to traditional DSSC photoelectrode material TiO_2, ZnO has not only similar wide bandgap energy of 3.2~3.3eV, but also much higher electron mobility (up to 1000 cm^2 V/s), as shown in Table 6.1. The most interesting point was that ZnO was quite easy to fabricate various nanostructures to obtain large surface area.

Table 6.1 The comparison of ZnO and TiO_2

Parameters	**ZnO**	**TiO_2**
Crystal structure	rocksalt, zinc blende, wurtzite	rutile, anatase, brookite
Fabrication of nanostructures	**easy**	**hard**
Energy band gap [eV]	**3.2~3.3**	**3.0~3.2**
Electron mobility [cm^2 V s^{-1}]	205~300(bulk), 1000(single nanowire)	0.1~4
Refractive index	2.0	2.5
Electron effective mass [m_e]	0.26	9
Relative dielectric constant	8. 5	170

If we wanted to apply the ZnO as the photoanode material in the DSSC, the first thing we need to do was to investigate the feasibility of ZnO using as photoanode in DSSC. Fig. 6.2 was the comparison of TiO_2 and ZnO based photoanode. The results

indicated that ZnO had the suitable conduction band and valence band, making ZnO possible to get the electrons from the dye molecules and transport the electrons to the TCO substrates (external circuit). This result indicated that ZnO can be used as the photoanode material in the DSSC.

Our previous work has succeeded in obtaining the hexagonal-cone ZnO nanorods on ZnO film using low-temperature treatment in a reducing gas ambient [16-17]. Compared with solution method, this technique is stable, simple, low cost, and easy to scale up.

In order to increase the efficiency of DSSC, we designed a novel DSSC structure using vertical well-aligned ZnO nanorods to replace TiO_2. A novel multiple reducing annealing method was developed to fabricate vertical well-aligned ZnO nanorods on ITO glass. The feasibility of ZnO nanorods as photoanode in DSSC was investigated.

6.2 ZnO-based DSSC fabrication

6.2.1 Experiments

6.2.1.1 ITO film fabrication

ITO thin films were deposited on alkali-free OA-10 glass (Nippon Electric Glass Co., Ltd.) by DC sputtering system. A 4-inch ITO ceramic target (99.99%) was located on the cathode 80mm away from the substrate. The sputtering chamber was evacuated until 5×10−4 Pa by using an oil diffusion pump. The output power of DC power source was 150 W. The deposition processes were performed in an Ar/O_2 ambient (20/0.2 sccm) controlled by mass flow controllers, which had proven to yield a good compromise between high conductivity and high transparency in this deposition system. The working pressure was maintained at 0.4 Pa. The substrate temperature on the anode was preheated to 250 ℃ for 20min prior to deposition and constantly maintained during

the deposition. In order to compare the effect of ITO film thickness, ITO films with different thicknesses were deposited: 200nm, 300nm, 400nm, and 500nm. The deposition rate of ITO films was 0.5nm/s. After the DC sputtering process, the samples were taken out from the sputtering chamber, and allowed to stand in the ambient air whilst cooling down to the room temperature.

6.2.1.2 ZnO film fabrication

ZnO thin films (500nm) were deposited by a conventional 13.56 MHz radio frequency (RF) magnetron sputtering system. A 4-inch ZnO ceramic target (99.999% ZnO) was located on the cathode 60mm away from the substrate stage. The background pressure in the sputtering chamber was evacuated to about 6×10^{-5} Pa with a turbo molecular pump. The RF power is 180 W. The deposition processes were performed in an Ar ambient (30 sccm) controlled by a mass flow controller. The working pressure was maintained at 7 Pa. The substrate temperature on the anode was preheated to 150 °C for 20min prior to deposition and was fixed during the deposition procedure.

6.2.1.3 ZnO nanostructure fabrication

Following the deposition procedure, ZnO thin film was put into a conventional furnace at low temperature annealing in a reducing gas ambient. Firstly a pre-annealing was introduced to treat the ZnO film at 300 ℃ for 2h in reducing ambient (1.9% H_2 in N_2). Then the ZnO film was treated at 450 ℃ for 5h in reducing ambient.

6.2.1.4 Dye-sensitized solar cell fabrication

A dye-sensitized solar cell device was successfully fabricated and demonstrated with the ZnO nanorods based photoanode. The structure of the dye-sensitized solar cell was ITO//ZnO Nanorods//N719//I^-/I_3^-//Pt//ITO.

The J-V characteristic of demonstrated DSSC were obtained by using a Keithley 2400 high voltage source interfaced to a computer, under simulated sunlight AM 1.5 with the radiant power of $100 mW/cm^2$. The photovoltaic parameters such as short circuit current density (Jsc), open circuit voltage (Voc), fill factor (FF) and efficiency (η) were analyzed from the J-V curve under illumination.

6.2.2 Characterization of ZnO based DSSC

6.2.2.1 Fabrication of high conductive and transparent ITO substrates

In order to reduce the cost and optimize the substrates for the fabrication of well-aligned ZnO nanostructures, we fabricated ITO films as electrodes in our lab. In order to choose the suitable ITO film for the fabrication of ZnO nanostructures on it, we modulated the ITO film with different thickness.

Figure 6.3 showed the AFM images of as-deposited ITO films with different thickness obtained from DC sputtering. The average rms roughness of the ITO film surface was calculated in a 2×2 μm^2 scan area. The results showed that the rms roughness of ITO films increased significantly from 0.501nm, to 1.94nm, 4.15nm, and 6.32nm in the order of thickness increased from 200nm to 500nm, respectively.

As reported [13], ITO films deposited by the DC sputtering showed a characteristic surface morphology, which was called domain-grain structures. The grains in the same domain had similar orientation. The large angle grain boundaries were called as domain boundaries. Shegesato et al. indicated that this type of morphology was caused by the ion bombardment effect during the DC sputtering process. Therefore, the domains grew to be bigger leading to a larger roughness if the sputtering time extended (indicating the film thickness increased). The AFM measurement results confirmed that the roughness of ITO films increased with the increase of film thickness.

The resistivity and mobility properties of as-deposited ITO films were also investigated by the Hall Effect measurement. The Van der Pauw method was used to determine the concentration and the type of the carriers. The dependences of resistivity and Hall mobility on the thickness of ITO films were shown in Fig. 6.4. Obviously, both resistivity and Hall mobility of the ITO films were significantly influenced by the film thickness. It was found that the resistivity of ITO films decreased when the thickness of ITO film increased from 200nm to 500nm, as well as the Hall mobility oppositely increased.

As well-known, ITO is oxygen defects heavily doped n-type semiconductor material. The two main factors of ITO affecting the resistivity are the electron mobility and the carrier concentration, as shown in Equation 1.

$$\rho = 1/(nq\mu) \qquad \textit{6-1}$$

n is the carrier concentration; q is the charge of electron; μ is the electron mobility.

Therefore, when the ITO film thickness increased, the increase of Hall mobility leaded to the decrease of resistivity, as shown in Fig. 6.4.

According the supplied data of commercial ITO glass (Sigma-Aldrich Co., Ltd.), the resistivity and Hall mobility are $2\times10^{-4}\Omega$cm and ~30cm^2/Vs respectively. Comparing to the commercial ITO glass, the resistivity and mobility from ITO thin films with 300~500nm-thick obtained in this experiment were comparable and even better. The lowest resistivity of $1.303\times10^{-4}\Omega$ cm and the highest Hall mobility of 29.2cm^2/Vs were respectively obtained from the 500nm-thick ITO film deposited on the glass.

The optical transmittance curves obtained from the ITO films with different thickness were shown in Fig. 6.5. The average transmittance of the all of ITO films in the visible light range was around 87%, which was higher than that from the commercial ITO glass (Sigma-Aldrich Co., Ltd.), about 85%.

6.2.2.2 Fabrication of ZnO films on ITO substrates

The XRD patterns of the ZnO films deposited on four different substrates were shown in Fig. 6.6. The X-ray diffraction analysis revealed that the (002) reflection peak was the dominate peak for all the films, meaning (002) preferred orientation with a c-axis perpendicular to the substrates. However, the peak intensities of ZnO films were significantly decrease with the thickness increase. The crystallinity of ZnO film was deteriorated gradually when the ITO film thickness increased from 200nm to 500nm.

The SEM images of as-deposited ZnO films were shown in Fig. 6.7. The thicknesses of all the deposited ZnO films were about 500nm. It was obviously that the clear column-like structure of as-deposited ZnO films gradually became vaguely with the ITO film thickness increased from 200nm to 500nm, indicating the crystallinity might gradually become worse with the ITO film thickness increased.

According to the above SEM image, it was clearly that the properties of ZnO films were significantly influenced by the properties of ITO substrates. Firstly, the ITO substrate surface roughness contributed to the grain growth during the ZnO thin film deposition. As reported, the good crystallinity attributed to a much flat substrate due to the lower lattice mismatch as well as less defects and variant. Therefore, the thinner ITO films exhibited the lower roughness, resulting in contributing to the better crystallinity of ZnO films.

For the thin film deposition on conductive substrates, the resistivity and Hall

mobility of the substrates could not be ignored because these two parameters of ITO substrates would significantly influence the initial film formation process. During the ZnO film sputtering process, the ZnO clusters were cracked from target to pile up to form ZnO films on the ITO substrate due to the bombardment effect. The ITO substrate was conductive and polycrystalline substrate, so that the sputtered ZnO species could move a relatively further distance on the surface of ITO substrates and the adhesion between the ZnO species and the ZnO films were weaker, resulting in worse crystallinity[15]. This might be the reason why the crystallinities of ZnO film were gradually improved with the ITO thickness decreasing.

6.2.2.3 Fabrication of ZnO nanostructures on ITO substrates

After reducing annealing processes, vertical aligned ZnO nanostructures were obtained on all of the substrates, as shown in Fig. 6.7(b). The SEM images indicated that ZnO nanostructures were significantly influenced by the thickness of ITO films. It was observed that the vertical alignment of ZnO nanostructures was gradually improved when the ITO film became thinner. The much higher density and height of ZnO nanostructures were obtained from much thinner ITO films. It was observed that the densities of ZnO nanostructures were gradually decreased from 115/ $(10\mu m)^2$ to 110/ $(10\mu m)^2$, 65/ $(10\mu m)^2$, and 20/ $(10\mu m)^2$ with the increase of ITO thin film thickness from 200nm to 300nm, 400nm, 500nm, respectively. The heights of ZnO nanostructures were correspondingly decreased from 1280nm to 1250nm, 950nm, and 840nm as well. ZnO nanostructures deposited on the thinner ITO films (200~300nm-thick) showed much higher density and average height.

As discussed in the ZnO film part, the better crystallinity of ZnO films was owing to thinner ITO films which have the low roughness, resistivity and mobility.

Sequentially, the good crystallinities of as-deposited ZnO films would contribute to the growth of well-aligned ZnO nanostructures during the growth of ZnO nanostructures, which was reported in my previous work [17].

According to our previously research [14-17], the growth of the ZnO nanostructures might be attributed to a two-stage growing processes including both vapor-solid (VS) process and vapor-liquid-solid (VLS) process. In this experiment, the catalysts were zinc atoms which were considered as self-catalysts, which were reduced by the reaction;

$$H_2 + ZnO \rightarrow Zn + H_2O \quad \textit{6-2}$$

Before the temperature approaching the melting point of zinc (419.6 ℃), the growth of the ZnO nanostructures was attributed to the VS mechanism, followed by "self-catalyzed" VLS growth process when the annealing temperature over 420 ℃. ZnO (0001) has the lowest surface free energy, resulting in a smooth surface in the equilibrium state. Therefore, ZnO nanostructures have a strong c axis (0001) preferred orientation, resulting in the fabrication of vertical ZnO nanostructures. The low roughness and high crystallinity of as-deposited films would contribute to the good vertical alignment of obtained ZnO nanostructures.

Therefore, ITO films with less thickness would help on fabricating vertical well-aligned ZnO nanostructures.

The optical transmittance curves of ZnO nanostructures on different ITO substrates were shown in Fig. 6.8. ZnO nanostructures on 200nm-thick and 300nm-thick ITO substrate showed the relatively higher transmittance, more than 75%, due to the good vertical alignment and crystallinity of the obtained ZnO nanostructures.

6.2.2.4 J-V measurement of ZnO-DSSC

The photoanode of dye-sensitized solar cell was applied to helping absorbing dye molecules to convert the photons to electrons as well as transporting the electrons to the power circuits, which required large effective surface area, high transmittance and high conductivity. In this experiment, we selected ZnO nanostructures deposited on the 300nm-thick ITO film as the photoanode in the demonstrated dye-sensitized solar cell, because these ZnO nanostructures had high density and average height as well as high transmittance. Moreover, the 300nm-thick ITO substrate exhibited much better conductive and mobility. Therefore, ZnO nanostructures on 300nm-thick ITO substrate were selected to be the photoanode in the demonstrated dye-sensitized solar cell.

As we discussed in the introduction section before, the surface area of ZnO nanostructures has significantly influence on the efficiency of DSSC. Therefore, two kinds of ZnO nanostructures on 300nm-thick ITO glass were applied in the demonstration of the ZnO-based DSSC. The SEM images of the two kinds of ZnO nanostructures were shown in Fig. 6.9. The height of two kinds of ZnO nanostructures was 1.2 μm and 2.8 μm, respectively. The structure of dye-sensitized solar cell was *ITO//ZnO nanostructures//N719//*I^-/I_3^-*//Pt//ITO.*

The J-V measurement was tested under simulated sunlight AM 1.5 with the radiant power of $100mW/cm^2$. The results were shown in Fig. 6.10.

The overall conversion efficiency of demonstrated ZnO-based solar cell with ZnO nanostructures (1.2 μm in height) as photoanode was 2.11% with a fill factor 0.549. The Jsc and Voc were $7.91mA/cm^2$ and 0.526V, respectively.

The overall conversion efficiency of demonstrated ZnO-based solar cell with ZnO nanostructures (2.8 μm in height) as photoanode was 3.65% with a fill factor 0.528. The Jsc and Voc were $12.67mA/cm^2$ and 0.551V, respectively.

The results indicated that the overall conversion efficiency increased with the increase of the size of ZnO nanostructures. The large size ZnO nanostructures had large surface area. And then the large surface area can help absorbing more dye molecules, leading to the more electrons will be injected to the ZnO nanostructures to transport to the circuit, which meant increase of the overall conversion efficiency.

6.2.3 Summary

In this section, the influences of the ITO substrate thickness on the as-deposited ZnO films as well as sequentially fabricated ZnO nanostructures were discussed. If the ITO film thickness increased, the roughness and Hall mobility of ITO films was increased while the resistivity of ITO films was decreased. When the ITO film thickness decreased, the as-deposited ZnO films exhibited better crystallinity and the following formed ZnO nanostructures showed the higher density, transmittance as well as better vertical alignment. The highest overall conversion efficiency of demonstrated dye-sensitized solar cell was 3.65% with a fill factor 0.528. The Jsc and Voc were 12.67mA/cm^2 and 0.551V, respectively.

6.3 Conclusions

In this chapter, the novel reducing annealing method was applied to fabricate vertical well-aligned ZnO nanostructures on ITO glass. The feasibility of ZnO nanostructures used as photoanode in DSSC was investigated.

If the ITO film thickness increased, the roughness and Hall mobility of ITO films was increased while the resistivity of ITO films was decreased. The as-deposited ZnO films deposited exhibited better crystallinity, and the following formed ZnO nanostructures showed the higher density, transmittance as well as better vertical

alignment when the ITO film thickness decreased. The highest overall conversion efficiency of demonstrated dye-sensitized solar cell was 3.65% with a fill factor 0.528. The Jsc and Voc were 12.67mA/cm^2 and 0.551V, respectively.

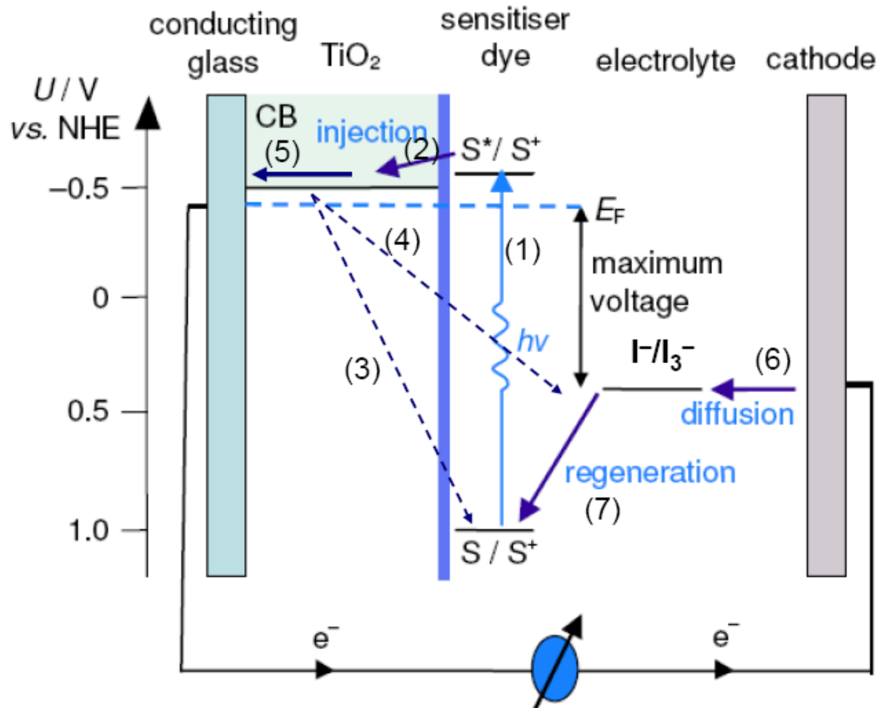

Fig. 6.1 The schematic diagram of dye-sensitized solar cell. [2]

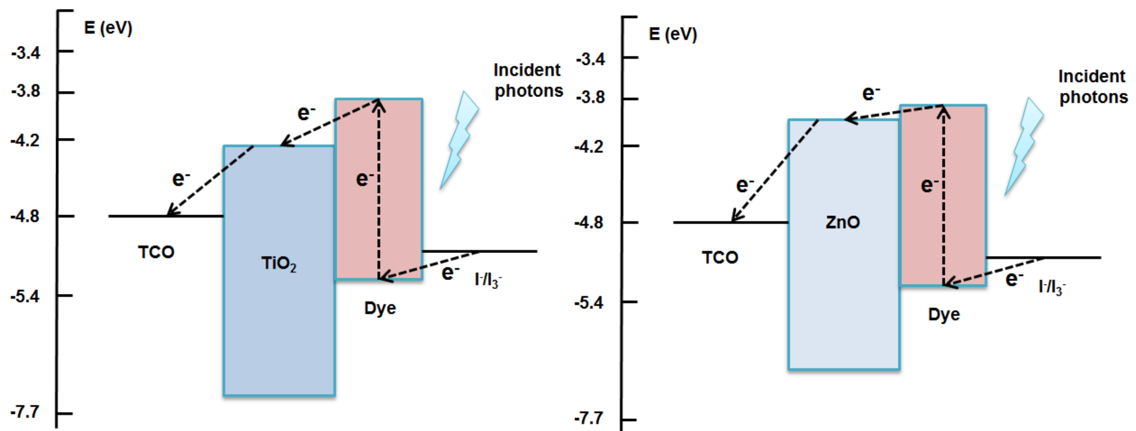

Fig. 6.2 The comparison of TiO_2 and ZnO based photoanode

(with the N719 dye, I^-/I_3^- electrolyte, TCO substrate)

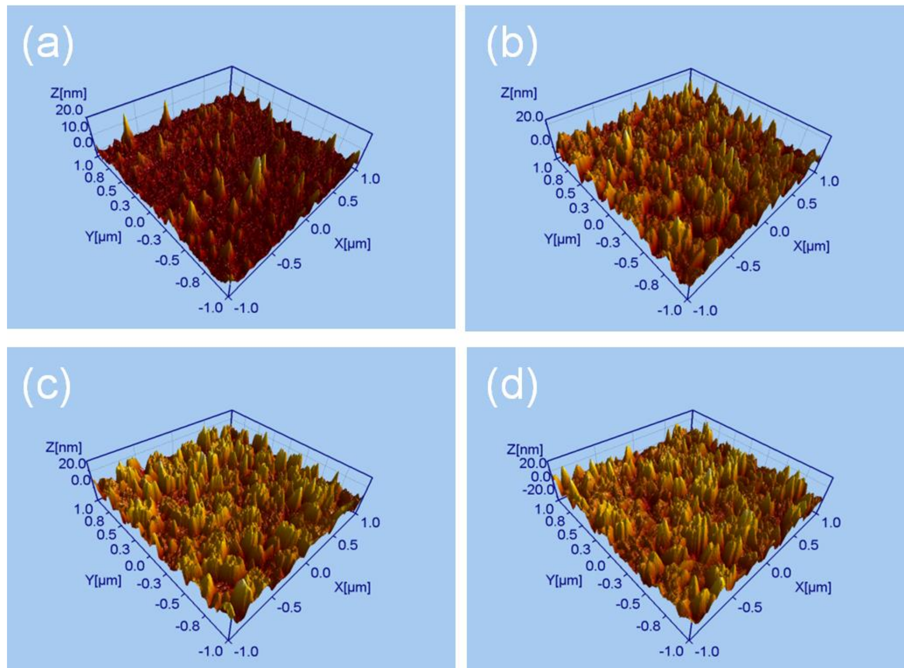

Fig. 6.3 AFM images of ITO thin films with thickness of (a) 200nm, (b) 300nm, (c) 400nm, and (d) 500nm.

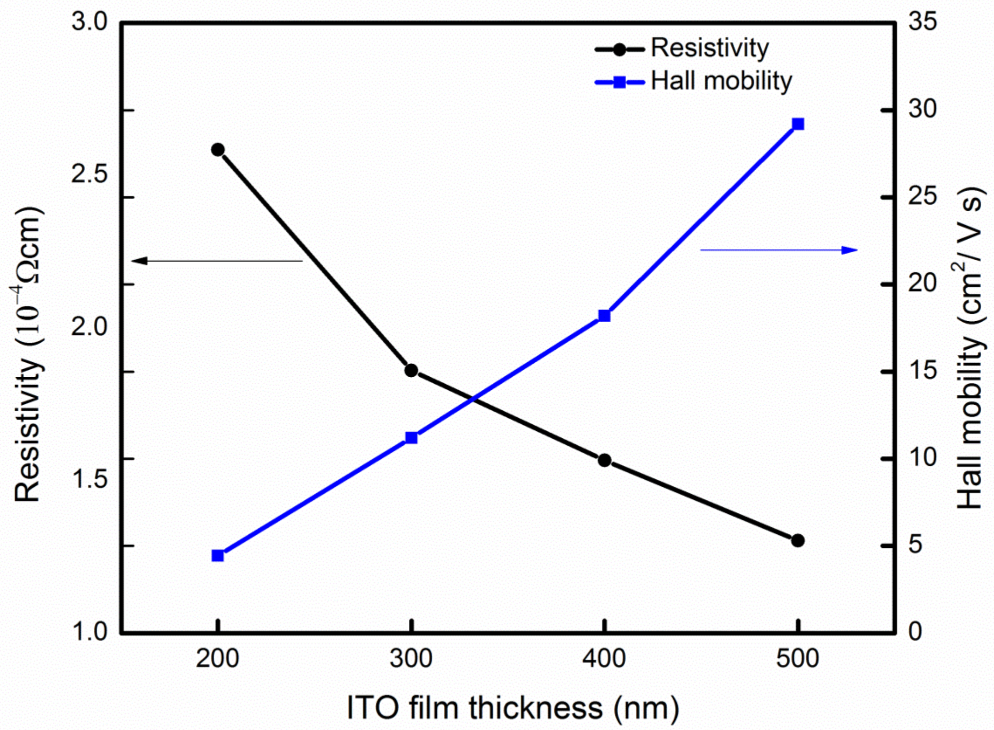

Fig. 6.4 The dependence of resistivity and Hall mobility on the thickness of ITO films.

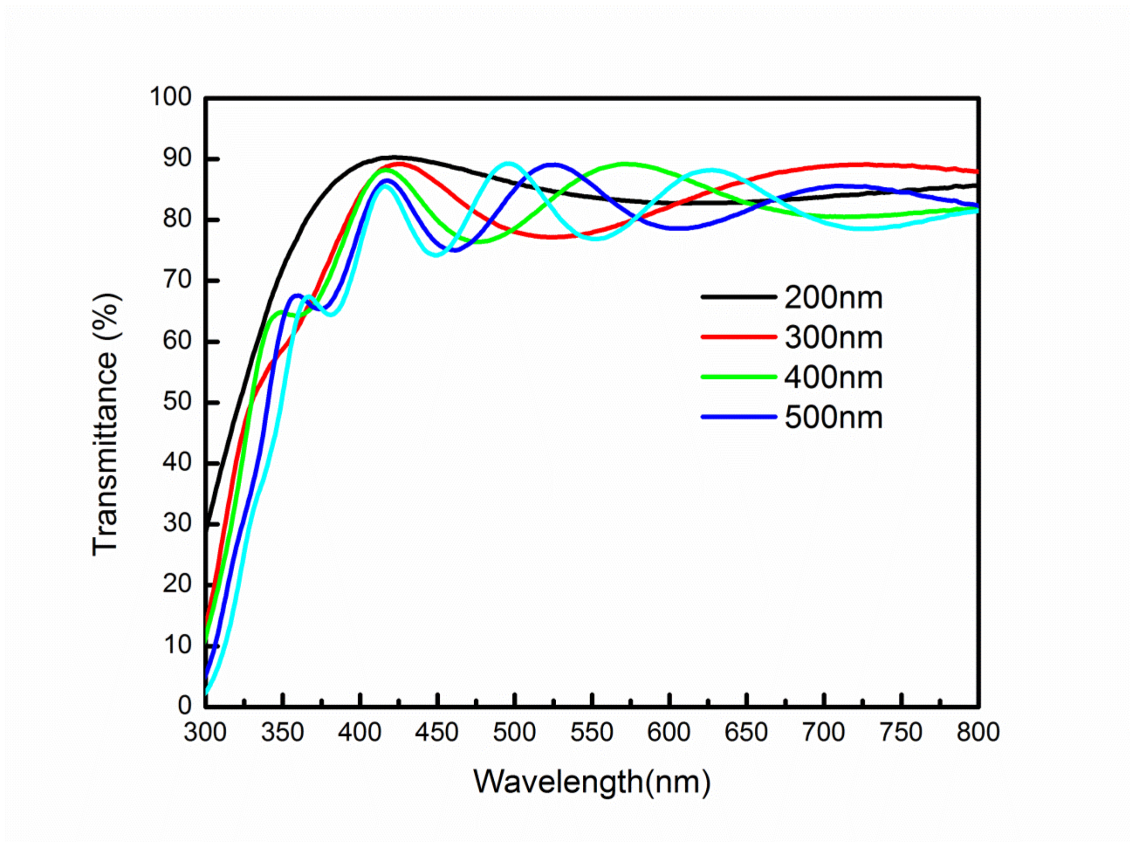

Fig. 6.5 The dependence of optical transmittance on the ITO film thickness.

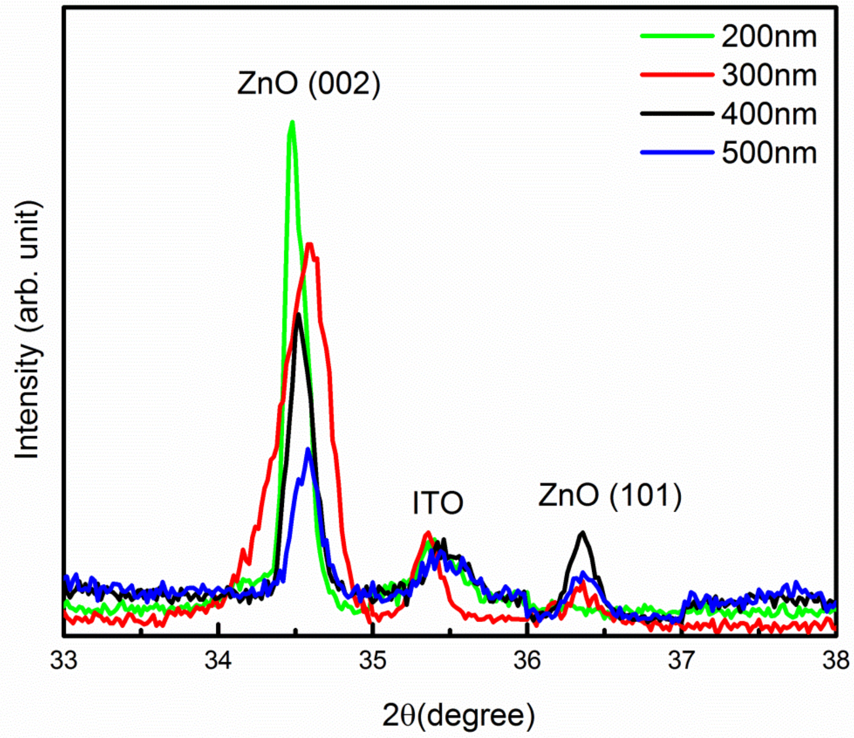

Fig. 6.6 The XRD patterns of as-deposited ZnO films on ITO film with different thickness.

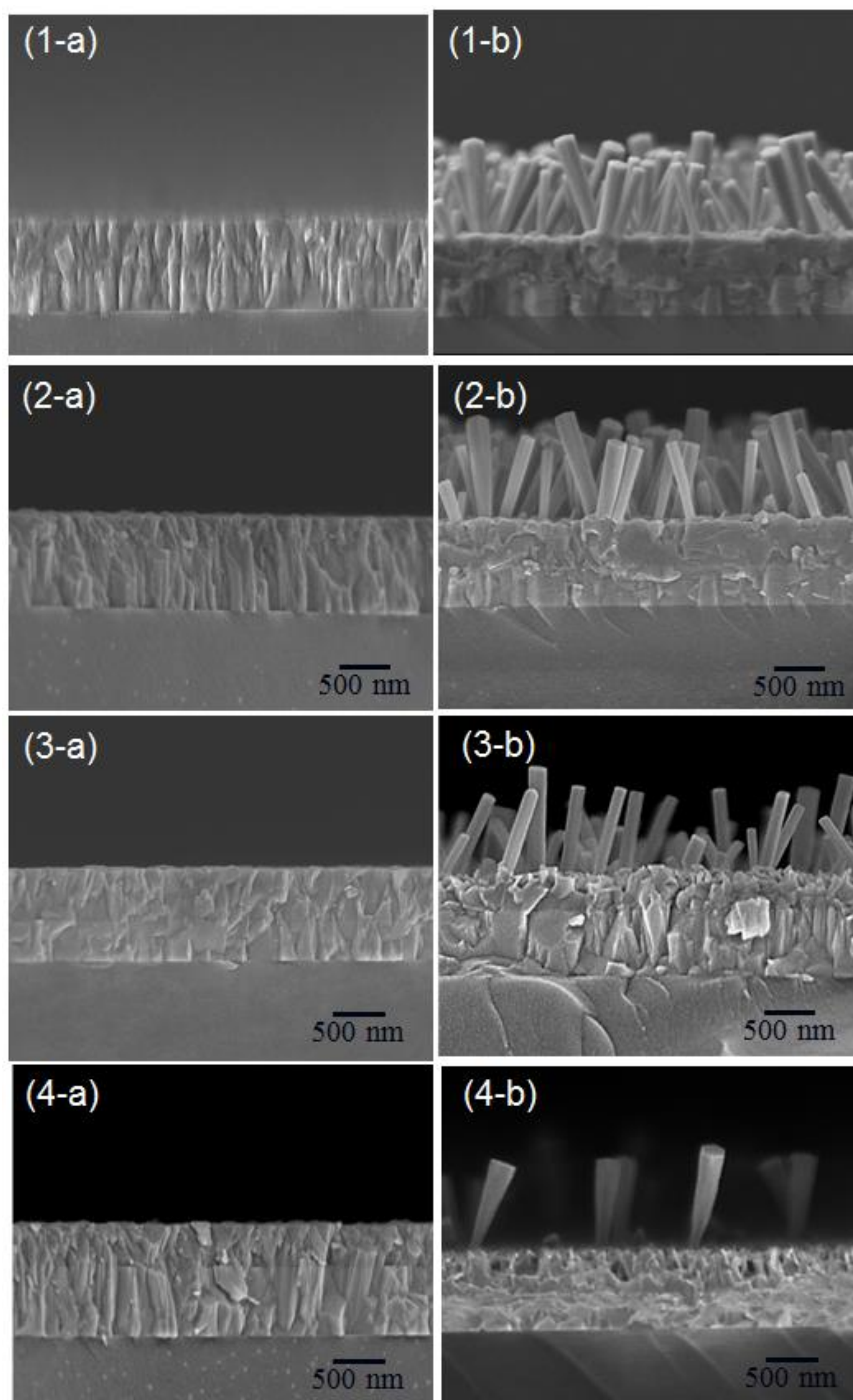

Fig. 6.7 SEM images of as-deposited ZnO film and nanostructures on ITO films with different thickness (1) 200nm (2) 300nm (3) 400nm and (4) 500nm.

(a: as-deposited ZnO films; b: obtained ZnO nanostructures)

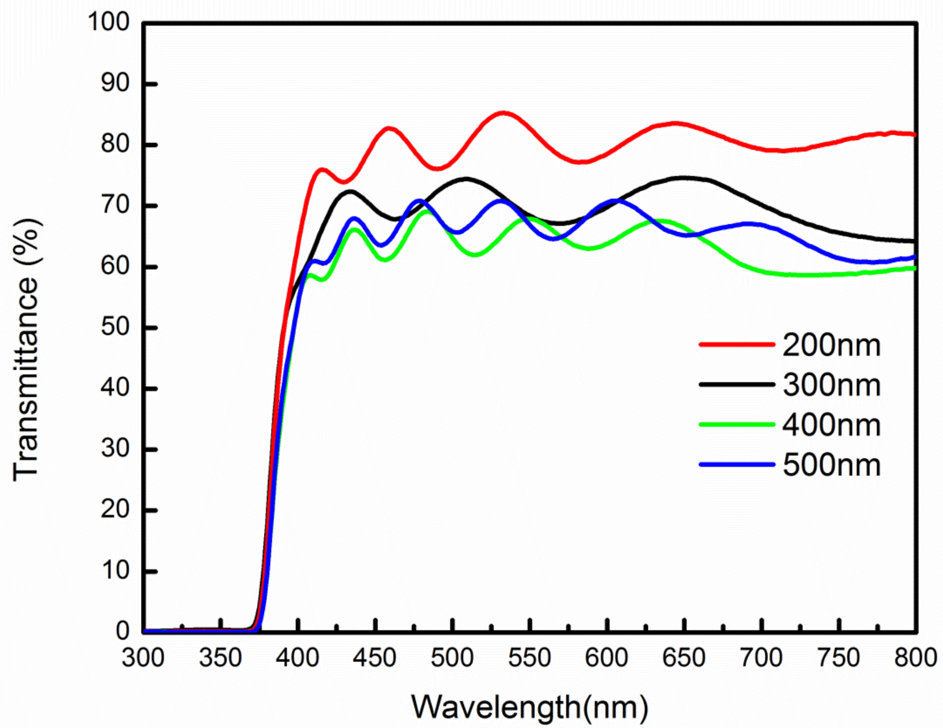

Fig. 6.8 The optical transmittance of ZnO nanostructures on ITO films with different thickness.

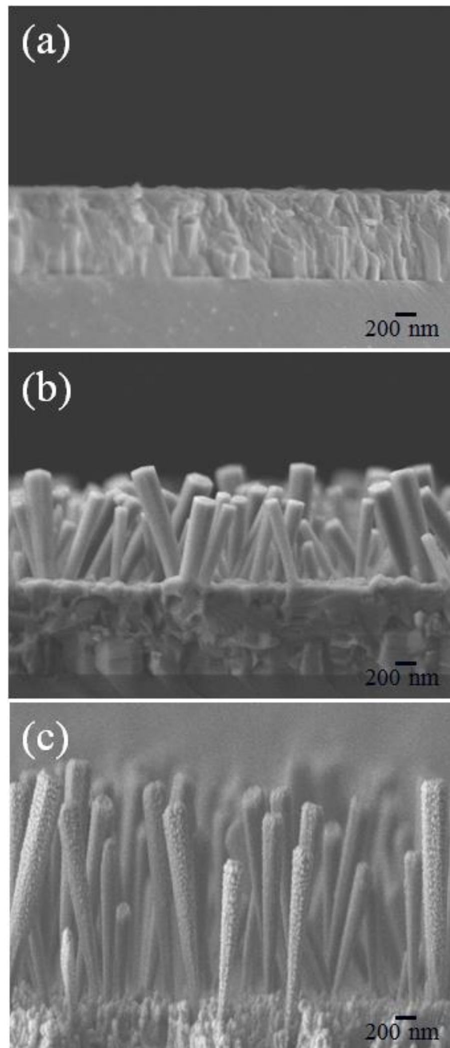

Fig. 6.9 SEM images of ZnO nanorods (a) As-deposited ZnO film, (b) after reducing annealing, and (c) after long time reducing annealing.

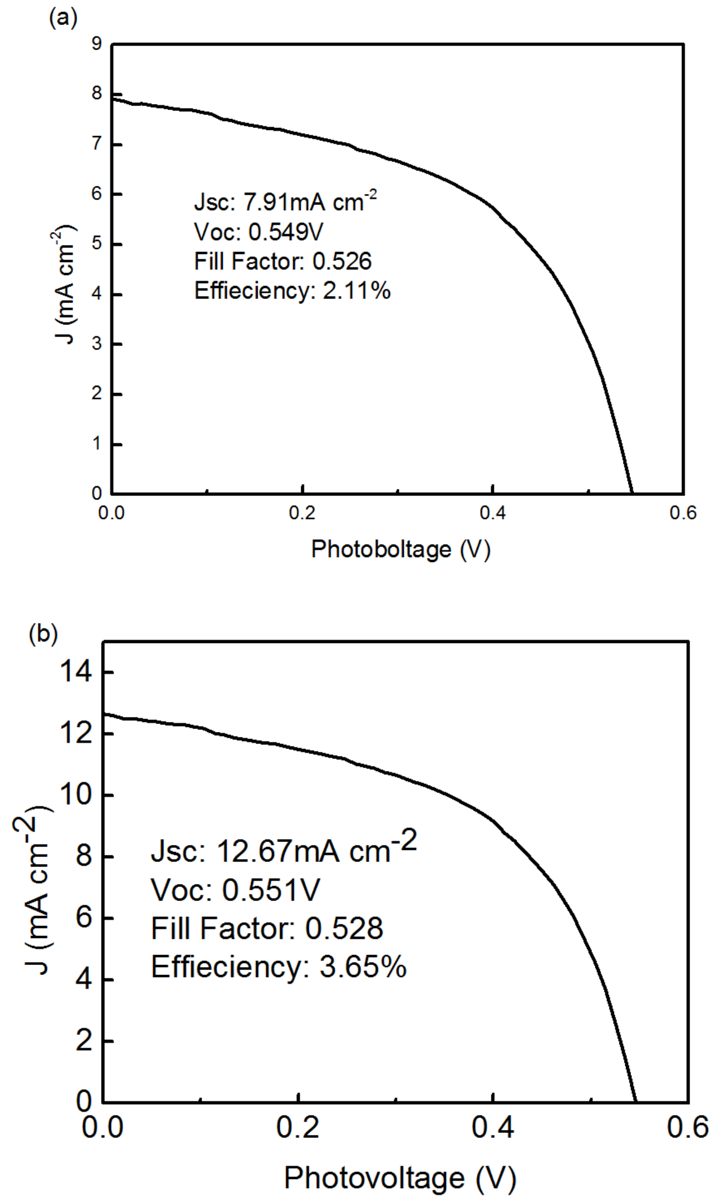

Fig. 6.10 J-V curve of the demonstrated dye-sensitized solar cell

(a: short ZnO nanostructures; b: long ZnO nanostructures.

Tested under simulated sunlight AM 1.5 with the radiant power of $100mW/cm^2$)

Reference

1 J. Huang, Z.G. Yin and Q.D. Zheng, Energy Environ, Sci., 4 (2011) 3861.

2 Q.H. Li, Q. Wan, Y.X. Liang, T.H. Wang, Appl. Phys. Lett. 84 (2004) 4556.

3 S. Choi, J. W. Kang, D. K. Hwang and S. J. Park, IEEE Transactions on Electron Devices, 57 (2010) 26.

4 B.F. Martinson, J.W. Elam, J.T. Hupp, and M.J. Pellin, Nano Lett. 7 (2007) 254.

5 T. Aoki, Y. Hatanaka, D. C. Look, Appl. Phys. Lett. 76 (2000) 3257.

6 J. Wu, S. Liu, Adv. Mater. 14 (2002) 215.

7 A. J. Petrella, H. Deng, N.K. Roberts, R.N. Lamb, Chem. Mater. 14 (2002) 4339.

8 X. Meng, D. Shen, J. Zhang, D. Zhao, Y. Lu, L. Dong, Z. Zhang, Y. Liu, X. Fan, Solid State Communications 135 (2005) 179.

9 H. Chik, J. Liang, S. Cloutier, N. Kouklin, J. Xu, Appl. Phys. Lett. 84 (2004) 3376.

10 S. Yamabi, H.J. Imai, Mater. Chem. 12 (2002) 3773.

11 L. Vayssieres, Adv. Mater. 15 (2003) 464.

12 Z. Li, X. Huang, J. Liu, Y. Li, G. Li, Materials Letters 62 (2008) 1503

13 J. Yang, M. Gao, L. Yang, Y. Zhang, J. Lang, D. Wang, Y. Wang, H. Liu, H. Fan, Applied Surface Science 255 (2008) 2646.

14 R.B. Peterson, C.L. Fields, B.A. Gregg, Langmuir 20b (2004) 5114.

15 L. Yang, Q. Zhao, M. Willander, J. Yang, J. Crystal Growth 311 (2009) 1046.

16 C. Y. Li, T. Kawaharamura, T. Matsuda, H. Furuta, T. Hiramatsu, M. Furuta, T. Hirao, J. Appl. Phys. Express., 2. (2009) 091601.

17 D.P. Wang, Z.M. Li, T. Kawaharamura, M. Furuta, T. Narusawa, and C.Y. Li, Phys. stat. Sol. (c), 9 (2012) 196.

Chapter 7

Conclusions

In this dissertation, my main work focused on the fabrication of vertical well-aligned large surface ZnO nanostructures for dye-sensitized solar cell applications.

In this thesis, I developed vertical well-aligned ZnO nanostructures on different substrates by novel reducing annealing technique. The surface morphology of the obtained ZnO nanostructures can be well controlled by the post-treatment of mist chemical vapor deposition technique. A highly conductive and transparent ITO substrate was fabricated by us by DC magnetron sputtering method, which was used as the substrates for the electrodes. With the large surface vertical well-aligned ZnO nanostructures on ITO substrates used as the photoanodes, I can get the ZnO-based DSSC with the high conversion efficiency of 3.75%.

The main conclusions of this thesis are summarized as follows:

I. Effects of substrate on the properties of vertical well-aligned ZnO nanostructures by single reducing annealing

The lower mismatch of the lattice imperfections and matching thermal expansion coefficient between ZnO film and substrates contributed to fabricating ZnO film with good crystallinity and vertical well-aligned ZnO nanostructures. ZnO film deposited on the silicon had the best crystallinity and the formed ZnO nanostructures with the best alignment and the highest density.

II. Effects of temperature on the properties of vertical well-aligned ZnO nanostructures by single reducing annealing

The density and height of ZnO nanostructures were increased with the increase of the annealing temperature. The diameter of ZnO nanostructures were increased when the temperature increased in the suitable range. The blue-green emission centered at 491nm was obtained from all of annealed samples, with the suppressed UV emission about 378nm. The intensity of visible peak (around 491nm) was increased with the increase of temperature.

III. Fabrication of controllable ZnO nanostructures by multiple annealing processes

In this part, the effects of different post-treatment processes on the ZnO nanostructures were investigated. The conclusions of each part in this chapter will be generally expressed one by one.

1) The oxygen treatment contributed to efficiently introduce the oxygen into the ZnO thin films between the two reducing annealing processes, leading to ZnO nanostructures regrown quickly. Adjusting the oxygen treatment time can help controlling the size and crystallinity of obtained ZnO nanostructures.

2) The low temperature treatment in the forming gas (1.9% H_2 in N_2) was introduced to help controlling the density of Zn atoms in the surface of the as-deposited ZnO films to control the density of obtained ZnO nanostructures.

3) ZnO nanostructures with controllable size and morphology were obtained by the novel multi-annealing processes.

IV. Influence of time and carrier gas on the properties of ZnO nanostructures treated by the Mist CVD technique

In this part, the effects of Mist CVD carrier gases and post annealing time on the crystal growth, structural properties of ZnO nanostructures were investigated.

1) The crystallinity and surface morphology of ZnO nanostructure were quite different with different carrier gases. The growth of ZnO nanostructures was epitaxial growth in the carrier gas Argon, indicating the obtained ZnO nanostructures were good single crystal with well-aligned ZnO nanosheet on the surface; the growth of ZnO nanostructures were random in the carrier gas Air, resulting in the obtained ZnO nanostructures were polycrystalline with intertwined nanosheets on the surface. Choosing the suitable carrier gases can help us obtaining the ZnO nanostructures with the designed crystallinity and surface morphology. Choosing the suitable carrier gases in the Mist CVD process can help us obtaining the ZnO nanostructures with controllable surface morphology.

2) With the increase of Mist CVD treatment time, the surface morphology of ZnO nanostructures were modified with intertwined (carrier gas: air) and aligned (carrier gas: argon) nanosheets and the size of ZnO nanostructures was enlarged. The size and morphology of ZnO nanostructure can be well controlled by modulating the Mist CVD treatment time.

V. Influence of ITO film thickness on the fabrication of ZnO nanostructures

In this part, the Influence of ITO film thickness on the fabrication of ZnO nanostructures was investigated.

If the ITO film thickness increased, the roughness and Hall mobility of ITO films was increased while the resistivity of ITO films was decreased. When the ITO film thickness decreased, the ZnO films deposited on ITO films exhibited better crystallinity, and the following formed ZnO nanostructures showed the higher density, transmittance

as well as better vertical alignment.

VI. Device demonstration of obtained vertical well-aligned ZnO nanostructures

In this part, the feasibility of ZnO nanostructures used as photoanode in DSSC was investigated.

The highest overall conversion efficiency of demonstrated dye-sensitized solar cell was 3.65% with a fill factor 0.528. The Jsc and Voc were 12.67mA/cm^2 and 0.551V, respectively.

Achievements in three years (2011-2014)

1) Credit (10)
2) Publication (8)

Publications (8)

First author (7):

Review Journal Papers

1. **Influence of substrate on zinc oxide nanostructures grown by thermal annealing**, Nanoscience and Nanotechnology Letters, 6, 174-180(2014).

   Xin Li, Chaoyang Li, Toshiyuki Kawaharamura, Dapeng Wang, Noriko Nitta, Mamoru Furuta, Hiroshi Furuta, and Akimitsu Hatta.

2. **Fabrication of zinc oxide nanostructures by mist chemical vapor deposition**, Transactions of the Materials Research Society of Japan, 39(2), 161-14(2014).

   Xin Li, Chaoyang Li, Toshiyuki Kawaharamura, Dapeng Wang, Noriko Nitta, Mamoru Furuta, and Akimitsu Hatta.

3. **Thickness of ITO thin film influences on fabricating ZnO nanorods applying for dye-sensitized solar cell**, Composite Part B: engineering, under review.

Xin Li, Chaoyang Li, Shengwen Hou, Akimitsu Hatta, Jinhong Yu, and Nan Jiang

4. **Fabrication of single crystal ZnO nanorods by novel hybrid method**, Applied Physics Letters, under review.

   Xin Li, Chaoyang Li, Shengwen Hou, Toshiyuki Kawaharamura, Dapeng Wang, and Akimitsu Hatta.

Proceeding

5. **Arrayed ZnO nanorods fabrication on ZnO film by self-catalyst growth method in aqueous solution**, Materials Research Society, 1584, 2013.

   Xin Li, Toshiyuki Kawaharamura, Dapeng Wang, Akimitsu Hatta, and Chaoyang Li.

6. **Fabrication of high conductive ITO thin film for photovoltaic applications**, AM-FPD20, 177-180 (2013).

   Xin Li, Chaoyang Li, Dapeng Wang, E.K.C Pradeep, Mamoru Furuta, and Akimitsu Hatta.

7. **Development of large surface ZnO nanorods as photoelectrode for dye sensitized solar cell application**, EU-PVSEC27, 434-436 (2013).

   Xin Li, Chaoyang Li, Toshiyuki Kawaharamura, Dapeng Wang, Noriko Nitta, Mamoru Furuta, and Akimitsu Hatta.

Co-author (1):

8. **Morphology controlled single-crystal ZnO nanostructures fabricated by a novel mist chemical vapor deposition**, SID Symposium Digest of Technical Papers, 44(1), 214-216 (2013).

   Chaoyang Li, **Xin Li,** Dapeng Wang, Toshiyuki Kawaharamura, Noriko Nitta, Mamoru Furuta, and Akimitsu Hatta.

(B) International conferences (13)

First author (7):

1. **Fabrication of high conductive ITO thin film for photovoltaic applications,** Active-Matrix Flatpanel Displays and Devices (AM-FPD) 2013, 2013, Jul. 2nd~5th, Kyoto, Japan, poster presentation

   Xin Li, Chaoyang Li, Dapeng Wang, Chandima Pradeep, Mamoru Furuta, and Akimitsu Hatta.

2. **Catalyst fabrication of well-aligned zinc oxide nanorods by a novel hybrid method,** 12th International Conference on Advanced Materials (IUMRS-ICAM 12), 2013, Sep. 22th ~ Sep. 28th, Qingdao, China, poster presentation

   Xin Li, Chaoyang Li, Toshiyuki Kawaharamura, Dapeng Wang, Noriko Nitta, Mamoru Furuta, and Akimitsu Hatta.

3. **Development of large surface ZnO nanorods as photoelectrode for dye-sensitized solar cell application ,** 28th European Photovoltaic Energy Conference and Exhibition (EU-PVSEC 28), 2013, Sep. 30th ~Oct. 4th, Paris, France, poster presentation

   Xin Li, Chaoyang Li, Toshiyuki Kawaharamura, Dapeng Wang, Noriko Nitta, Mamoru Furuta, and Akimitsu Hatta.

4. **Catalyst free growth of well-aligned zinc oxide nanorods,** 12th Asia Pacific Physics Conference of AAPPS (APPC 12),2013, Jul. 13th ~19th, Chiba, Japan, poster presentation

   Xin Li, Chaoyang Li, Toshiyuki Kawaharamura, Dapeng Wang, Noriko Nitta, Mamoru Furuta, and Akimitsu Hatta.

5. **A novel fabrication technique of zinc oxide nanorods for photoelectric applications,** 4th International Symposium of Frontier Technology, 2013, Jul. 25th ~30th , Shenyang, China, oral presentation

   Xin Li, Chaoyang Li, Toshiyuki Kawaharamura, Dapeng Wang, Noriko Nitta, Mamoru Furuta, and Akimitsu Hatta.

6. **Influence of substrate on zinc oxide nanostructures grown by thermal annealing** , 20th Annual International Conference on Composites or Nano Engineering (ICCE-20), 2012, Jul. 13th~19th, Beijing, China, oral presentation

   Xin Li, Chaoyang Li, Toshiyuki Kawaharamura, Dapeng Wang, Noriko Nitta, Mamoru Furuta, and Akimitsu Hatta.

7. **Fabrication of zinc oxide nanostructures by mist chemical vapor deposition** , International Union of Materials Research Societies - International Conference on Electronic Materials 2012 (IUMRS-ICEM 2012), 2012, Sep. 23rd~29th,Yokohama, Japan, oral presentation

   Xin Li, Chaoyang Li, Toshiyuki Kawaharamura, Dapeng Wang, Noriko Nitta, Mamoru Furuta, and Akimitsu Hatta.

Co-author (6):

8. **A novel method for fabrication well-aligned ZnO nanostructures,** 2013 IEEE International Nanoelectronics Conference (INEC 2013), 2013, Jan. 2nd~4th , Singapore, invited talk

   Chaoyang Li, **Xin Li,** Dapeng Wang, Toshiyuki Kawaharamura, Noriko Nitta, Mamoru Furuta, and Akimitsu Hatta.

9. **Morphology controlled single-crystal ZnO nanostructures fabricated by a novel mist chemical vapor deposition**, Society for Information Display (SID 2013), 2013, May. 19th~24th, Vancouver, Canada, oral presentation

   Chaoyang Li, **Xin Li,** Chandima Pradeep, Dapeng Wang, Toshiyuki Kawaharamura, Noriko Nitta, Mamoru Furuta, and Akimitsu Hatta.

10. **High luminance nano-structured zinc oxide thin film fabrication,**

6th International Conference on Advanced Infocomm Technology (ICAIT), 2013, Jul. 6th~9th, Hshichu, Taiwan, invited talk

Chaoyang Li, **Xin Li,** Dapeng Wang, Toshiyuki Kawaharamura, Noriko Nitta, Mamoru Furuta, and Akimitsu Hatta.

11. **Influence self-organized growth ZnO based nanorods for photonic device application,** 12th International Meeting on Information Display (IMID 12), 2012, Aug. 29th~31st, Daegu, Korea, invited talk.

    Chaoyang Li, Dapeng Wang, **Xin Li,** Toshiyuki Kawaharamura, Noriko Nitta, Mamoru Furuta, and Akimitsu Hatta.

12. **Effects of thickness on the optical properties of ZnO films prepared by radio frequency magnetron sputtering,** 20th Annual International Conference on Composites or Nano Engineering (ICCE-20), 2012, Jul. 22nd~27th, Beijing, China, invited talk

    Chaoyang Li, Zeming Li, Dapeng Wang, **Xin Li,** Toshiyuki Kawaharamura, Noriko Nitta, Mamoru Furuta, and Akimitsu Hatta.

13. **A novel dye-sensitized solar cell using well-aligned ZnO nanorods,** 27th European Photovoltaic Energy Conference and Exhibition (EU-PVSEC 27), 2012, Sep.23rd~28th, Frankfort, Germany, poster presentation

    Chaoyang Li, **Xin Li,** Dapeng Wang, Toshiyuki Kawaharamura, Noriko Nitta, Mamoru Furuta, and Akimitsu Hatta.

(C) Best paper award (1)

1. **Catalyst fabrication of well-aligned zinc oxide nanorods by a novel hybrid method,** 12th International Conference on Advanced Materials (IUMRS-ICAM 12), 2014, Sep. 22th ~ Sep. 28th, Qingdao, China, poster presentation

   Xin Li, Chaoyang Li, Toshiyuki Kawaharamura, Dapeng Wang, Noriko Nitta, Mamoru Furuta, and Akimitsu Hatta.

   Excellent Poster Award